Thermal and Chemical Freeze-out in Heavy Ion Collisions

Masashi Kaneta

Department of Physics, Faculty of Science,
Hiroshima University,
Kagamiyama 1-3-1, Higashi-Hiroshima,
Hiroshima 739-8526, Japan

29 January, 1999

To my parents and my friends,
especially
late Hisashi Kaneta
and
late Kazuhiro Kaimi

Abstract

I have studied single particle spectra of hadrons produced in the high energy heavy ion collisions. Experimental data of the present interest have been obtained by the NA44 momentum focussing spectrometer at the CERN-SPS. The particle source produced in these collisions has a very high energy density and therefore high temperature and immediately begins to expand and cool. When the expansion reaches to a certain extent, eventually the temperature decreases at a point where hadrons stop interacting with each other. The particle ratios are fixed at this point and we refer to this state of particle source as a chemical freeze-out. There is another type of freeze-out, that is, after further expansion and cooling, the temperature goes down to a point where the final state interactions between hadrons are no longer effective. This is referred to as a thermal freeze-out.

In this thesis, absolute values of single particle spectra are determined for pions, kaons, protons and antiprotons as functions of transverse mass (m_T) near mid-rapidity in 158 A GeV/c Pb+Pb collisions. From the particle mass dependence for the observed m_T distributions, we are able to deduce a value of about 130 MeV for the temperature at the thermal freeze-out. On the other hand, from the observed ratio of the rapidity densities, we are able to determine values of the chemical potential for light and strange quarks to be approximately 65 and 15 MeV, respectively, as well as a value of about 140 MeV for the temperature of the chemical freeze-out.

These values seem to justify our scenario, that is, in heavy ion collisions at CERN-SPS energies, the particle source of very high energy density, a kind of fire ball of high energy density, is produced. It then cools due to fast expansion. During the expansion, the fire ball reaches the chemical freeze-out at first and finally goes to the thermal freeze-out. It is also noted that if we believe in a usual model of quark-gluon plasma, the values of chemical potentials and chemical freeze-out temperature determined above suggest that the state of the fire ball immediately after the collision is rather close to the state of the quark gluon plasma.

Contents

Chapter 1

INTRODUCTION

1.1 Quark gluon plasma

Quantum ChromoDynamics (QCD) predicts the new state of the matter, Quark Gluon Plasma (QGP) at extreme temperature and/or density. QCD indicates that QGP is expected in the early universe, neutron stars and high energy heavy ion collisions. The latter is the only way to confirm the existence of QGP in a laboratory.

In the 1970's, deep inelastic electron-proton experiments indicated that nucleons have sub-structure. Now, it is known that they are consisting of quarks and gluons. QCD describes the interactions between these quanta. Particles consisting of quarks and gluons are called as 'hadrons' and in two main types, mesons and baryons. A meson is built of a quark and an anti-quark and a baryon is built of three quarks. The gluon corresponds to the photon in QED and its mediates the strong force by exchanging 'colour' between particles. Unlike the photon the gluon is itself charged. The strong force confines quarks and gluons in the hadrons. The hadrons have no colour charge and free quark or gluon is not observed in our physical world.

At extremely high density ($\rho > 10^{15}$ g/cm^3) and the high temperature ($T > 10^{12}$ K), the strong tie among quarks and gluons weaken and coloured objects can propagate for long distances. A QGP of free quarks and free gluons is expected in such an environment. It is thought that such situation is realized in the neutron star, the early state of the universe and the high energy heavy ion collisions.

The search for the QGP in high energy heavy ion collisions connects nuclear physics, elementary particle physics and astrophysics.

Nuclear physics studies the structure of nuclei and the nuclear force at beam momenta up to 1 GeV/c per nucleon. The nucleus is a state of hadronic matter at approximately zero temperature and at low density. In relativistic high energy heavy ion collisions, high temperatures and densities have been studied in terms of thermal and chemical equilibrium. Its view point has success to understand the state of hadron sources. This has proved useful for the analysis of hadron production in the GSI-SIS energy region [1].

Elementary particle physics studies the fundamental constituent of matter. QCD is the theory of quarks and gluons. At high energy and momentum transfer, experiments confirm validity of perturbative calculations with QCD. On the other hand, the non-perturbative region, which includes the QGP, is not well studied. Relativistic high energy heavy ion collisions test the non-perturbative QCD.

According to the Big-Bang theory of cosmology, our universe was born about twenty billion years ago as hot and dense fire ball. The universe has been expanding and cooling since then and it is thought to have experienced a phase transition from the QGP phase to the hadron phase at a temperature ($T \approx 200$MeV) and 10^{-5} seconds from the Big-Bang. The centre of the neutron stars have the high baryon density (~ 10 times of the nucleon) and a cold QGP may exist there. Since both phenomena are difficult to observe directly, the search for QGP contributes to astrophysics and cosmology.

1.2   High energy heavy ion collisions

In the 1950's Fermi predicted that the high temperature and/or density matter would be created in high energy heavy ion collisions or very high energy proton-proton collisions [2]. In the same era, multi-particle cosmic ray events were measured. The 'fire ball' model was introduced to explain the phenomena and it was believed that the production of particles was controlled by thermodynamic quantities such as temperature and density.

Experiments have been done to find the QGP at CERN^{I,II} (European Laboratory for Particle Physics) and BNL^{III} (Brookhaven National Laboratory) since the end of the 1970's.

The first round of experiments with relatively light ions showed that nuclei were not

---

^{I}The acronym CERN comes from the earlier French title: "Conseil Européen pour la Recherche Nucléaire"

^{II}http://www.cern.ch/

^{III}http://www.bnl.gov/bnl.html

transparent at high energy and that a large amount of transverse energy was produced. This was a necessary pre-condition for QGP.

In the second generation of high energy heavy ion experiments, from the end of the 1980's dedicated experiments were built to measure the four-momenta of each particle in the acceptance. Collaborations focused on one or two topics such as charged hadrons, multi-strange baryons, di-leptons, photons, or two particle interferometry. Many phenomena consistent with QGP have been observed. A sample of this work can be found in the following references; strangeness and antibaryon enhancement [3]-[6], 'exotic' signatures of the QGP [7], photons and lepton pairs [8, 9], J/ψ suppression [10, 11], space time expansion measured by two particles interferometry [12], and single particle momentum spectra and yield [13]. The physics of each topic is explained in the following subsections.

1.2.1 Strangeness and antibaryon enhancement

The nucleus has no strange quantum number and no antiquark except sea quarks. At high density, the Pauli exclusion principle favours the creation of strange quarks compared to the more numerous up and down quarks. Therefore, the enhancement of strangeness might be one of signals of QGP. Antibaryon enhancement may arise the creation of u$\bar{\text{u}}$ pair and d$\bar{\text{d}}$ pairs in the QGP. On the other hand, the strangeness and antiquark enhancement occur in a high temperature hadron gas by $\pi + \text{p}$ to $\text{K} + \Lambda$, for example.

1.2.2 'Exotic' signatures of the QGP

When the density of quarks is very high, the Fermi energy of up and down quarks may exceed the mass of the strange quark. It is then easier to produce s$\bar{\text{s}}$ pairs of quarks than u$\bar{\text{u}}$ or d$\bar{\text{d}}$ pairs. (This may happen in neutron stars.) However, hadronization tends to extract $\bar{\text{s}}$ quarks before s quarks. This is called strangeness distillation and may result in the creation of a quark nugget containing many strange quarks. This is called a strangelet.

A strangelet candidate named 'Centauro' was observed in cosmic ray interactions by the Brazil-Japan emulsion chamber collaboration [14]. Many experiments tried to observe Centauro-like events accelerators, in Fermi Lab., BNL, CERN and so on. Unfortunately, none has been observed since then.

1.2.3   Photons and di-leptons pairs

The electromagnetic probes, photons and di-leptons may be better signals of QGP than the hadronic probes since they are free from strong final state interactions in the fire ball.

The energy spectrum of photons may reflect thermal radiation from a hot gas of quarks and gluons. However, the low energy region is heavily contaminated by a background from decays of hadrons, mainly π^0 and η. In the high momentum region, the At high energy, there is a background from "direct" processes such as g+q to γ+q reaction and Compton scattering. Current experimental sensitivities are not sufficient to observe a clear signal.

Lepton pairs are created in the hot gas by the $q\bar{q}$ annihilation and the Drell-Yan process, i.e. quark-antiquark annihilation. The CERES (NA45) collaboration[IV] has measured di-electrons and reported a very interesting invariant mass distribution. In the p+A collisions, the invariant mass distribution can be explained by an extrapolation from p+p collisions [15, 16]. On the other hand, the distribution from S+Au [15, 17] and Pb+Pb [18] collisions can not be reproduced by the extrapolation. The phenomenological candidates to explain the discrepancy are a mass shift [8, 9] and/or a changing width of the light vector mesons, ρ and ω in the high dense matter.

1.2.4   J/ψ suppression

The J/ψ is a bound state of c$\bar{c}$ pair (charmonium). Since the charm quark has large mass (1.1∼1.4 GeV [19]), the thermal creation of c$\bar{c}$ is suppressed by Boltzmann factor. The Drell-Yan process of nucleon-nucleon collisions in the heavy ions makes c$\bar{c}$. If the QGP is made in the heavy ion collisions, the c and $\bar{c}$ are liberated in the QGP gas and possibility of the bound state is small [10]. In the plasma's temperature is greater than about 1.2 times critical temperature, the bound state is forbidden by Debye screening between colour charges [11]. The c and the $\bar{c}$ quark hadronize with the other quark in the gas and form the charmed meson D and $\bar{D}$. Thus, J/ψ suppression is one of the signals of QGP.

The CERN experiment NA38[V]/NA50[VI] and the NA51[VII] have measured J/ψ, ψ' and Drell-Yan production in p+A, O+A, S+A and Pb+Pb collisions. The NA50 collaboration

---

[IV]http://ceres6.physics.uni-heidelberg.de/
[V]http://www.cern.ch/NA38/
[VI]http://www.cern.ch/NA50/
[VII]http://lyoinfo.in2p3.fr/eiexp/na51.html

recently reported that the ratio J/ψ to Drell-Yan yield as a function of L, the mean path length of the produced c$\bar{c}$ state through a nuclear matter [20, 22]. They claim that 'the anomalous suppression appears as a sharp discontinuity from the nuclear absorption mechanism in Pb+Pb collisions' in Ref. [20].

1.2.5 Space time expansion measured by two particles interferometry (HBT)

The Hanbury-Brown Twiss (HBT) effect, or Bose Einstein correlation, is a technique to measure the size of a source of bosons. Originally, this was used to determine a size of a fixed star by measuring the interference of photons [23, 24]. However, a hadron source generated in ultra-relativistic high energy heavy ion collisions is not static like a star and this complicates the interpretations [12, 21].

If a QGP is realized in the heavy ion collisions, anomalous size or time duration might be observed [25, 26]. The hadronic source size has been studied by the pion, kaon and proton interferometry at AGS and SPS. These measurements have been done by E802/E859/E866, E814/E877[VIII] and E917[IX] collaborations at BNL and NA35[X]/NA49[XI] NA44[XII] collaborations and WA80/WA93/WA98[XIII] collaborations at CERN.

For Pb+Pb collisions, the recent result of pion interferometry from experiments show that the pion HBT radius in the transverse direction is of the same order of the nucleus radius at the freeze-out. The longitudinal HBT radius is close to or larger than transverse radius.

1.2.6 Single particle momentum spectra and yield

Hadron momentum spectra and the rapidity densities (dN/dy) contain many informations on the state of hadron gas at the freeze-out. Those may be affected by the thermal and chemical freeze-out, the transverse flow, the collective flow and the stopping power.

It is well known that the transverse momentum spectra of the hadrons seem to be

---

[VIII]http://skipper.physics.sunysb.edu/~e877/Home.html

[IX]http://rudipc.phy.uic.edu/e917_at_ags/

[X]http://na35info.cern.ch/

[XI]http://na49info.cern.ch/na49/

[XII]http://www.nbi.dk/na44/

[XIII]http://www.cern.ch/WA98/

Boltzmann distributions in heavy ion collisions. This is also seen in p-p collisions and its might be from the Fermi motion of parton in nucleons. In ultra relativistic high energy heavy ion collisions, the multiplicity of hadrons generated ranges from several hundred to several thousand. The dN/dy distributions of the hadrons in the high energy heavy ion collisions can not be explained by simple extrapolations from p-p collisions and indicate that the hadrons have inelastic and/or elastic scattering with each other. Therefore, a thermo-dynamical description is suitable to explain the momentum distributions.

If the hadron gas was in equilibrium before the freeze-out, the temperature, and chemical potentials should describe the momentum distributions and the particle ratios. The temperature is derived from transverse momentum spectra since the longitudinal distribution (parallel with beam direction) is effected of the beam energy. The dN/dy distribution gives information on longitudinal flow.

The other freeze-out is 'Chemical freeze-out' and is related to particle creations. If the hadron gas reaches chemical equilibrium, the abundances of different particle species are controlled by chemical potential. Since the two freeze-out's occur at different time, the analyses for both freeze-out are done separately.

For central collision, (where axial symmetry holds well), transverse flow has been found by several experimental groups at BNL-AGS and CERN-SPS including NA44 [27]. In peripheral collisions, the more general collective flow analysis is done. The spectators may affect the momentum distribution by a fluid-like effect. It has been found that the effect of collective motion for the pion spectra is different from the effect on the protons [28]-[31].

The stopping power of nuclear medium for hadrons is a key quantity for formation of energetic and baryon rich collision complex. It is discussed from the rapidity distribution of protons. The distribution has not only protons generated in the collisions but original protons in the ions. The experimental results show that the stopping power at AGS energy ($E_{lab} \approx 10$ GeV / nucleon) is greater than at SPS energy ($E_{lab} \approx 10^2$ GeV / nucleon).

1.3   Subject studied in this thesis

As reviewed above, chemical and thermal freeze-out are crucial stages of development of the hot and dense system formed by high energy heavy ion collisions.

The invariant cross sections of single charged particles, $\pi^\pm$, $K^\pm$, p and $\bar{p}$ are measured

as a function of transverse mass (m_T) near mid-rapidity in central 158 A GeV Pb+Pb collisions. The temperature for thermal freeze-out is obtained from the particle mass dependence for the observed m_T distributions and a values of about 130 MeV is deduced for T_{th}. From the particle ratios, I deduced the values; the temperature of about 140 MeV for chemical freeze-out, the chemical potential for light and strange quarks of approximately 65 and 15 MeV, respectively.

These values seem to justify our hypothesis, that is, in heavy ion collisions at CERN-SPS energies, a particle source of very high energy density, a kind of fire ball, is produced and then subjected to rapid cooling due to fast expansion. During the expansion, the fire ball reaches chemical freeze-out first and later thermal freeze-out. The systematical study of chemical freeze-out for various collision systems indicates that the T_{ch} is increasing with the beam energy, while the baryon densities at mid-rapidity is decreasing.

It is remarkable that if we believe in a usual model of quark-gluon plasma, the values of chemical potentials and freeze-out temperatures determined above suggest that the state of the fire ball immediately after the collision is rather close to the region where we expect the QGP phase transition.

In the next chapter, set-up and detectors of the NA44 experiment are described. Following that, the analysis method will be shown and then the transverse mass distributions and the rapidity densities at mid-rapidity. Finally, thermal and chemical freeze-out will be discussed in the light of the transverse momentum spectra and dN/dy values from NA44.

Chapter 2

NA44 EXPERIMENT AT CERN SPS

NA44 is one of experiments at the CERN Super Proton Synchrotron (SPS) and the name 'NA44' means the 44th experiment in North Area.

The SPS is a part of the CERN accelerator complex (see Fig. 2.1). The accelerator has a collider mode for proton and antiproton collisions. The collider called $S\bar{p}pS$ and the Novel prize in 1984 was awarded to the discovery for W and Z bosons using the accelerator complex. It accelerates protons up to 450 GeV/c, sulphur nuclei up to 200 A GeV/c and lead nuclei up to 158 A GeV/c. The SPS accelerator provides heavy ion beams at the highest energies in the world.

The NA44 collaboration consists of about 50 members and 12 institutes from the world. The present collaboration institutes are shown in the following list.

- Brookhaven National Laboratory, Upton, New York 11973, USA

- CERN, CH-1211 Geneva 23, Switzerland

- Department of Physics, Columbia University, New York, New York 10027, USA

- Department of Physics, Hiroshima University, Kagamiyama 1-3-1, Higashi-Hiroshima 739-8526, Japan

- Department of Physics, Ohio State University, Columbus, Ohio 43210, USA

- Department of Physics, University of Lund, S-22362 Lund, Sweden

- Los Alamos National Laboratory, Los Alamos, New Mexico 87545, USA

- Niels Bohr Institute, DK-2100 Copenhagen, Denmark

- Nuclear Physics Laboratory of Nantes, 44072 Nantes, France

- Rudjer Boskovic Institute, Zagreb, Croatia

- State University of New York, Stony Brook, New York 11794, USA

- Technical University, A-1040, Vienna, Austria

- Texas A&M University, College Station, Texas 77843, USA
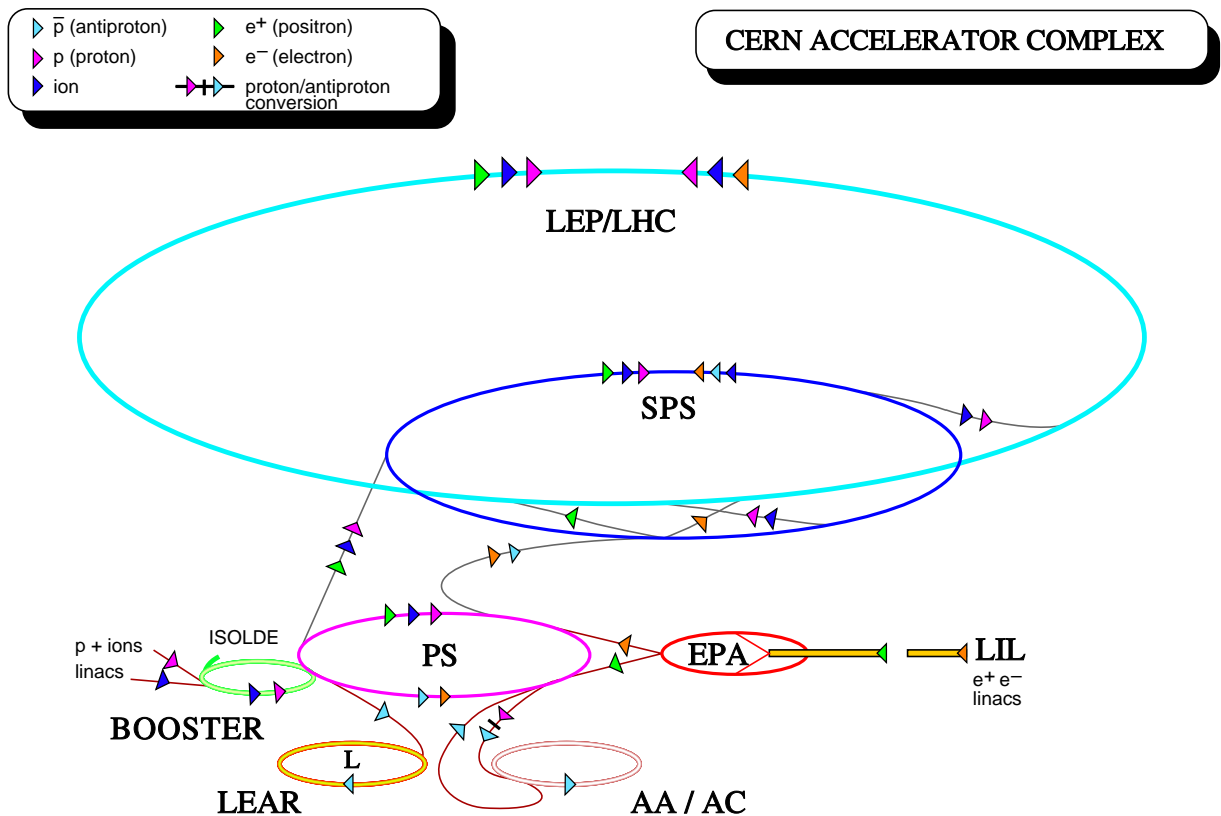
Figure 2.1: Accelerator complex system in CERN

2.1 NA44 experiment

The aim of our experiment is to study the space-time evolution and the temperature of hadronic matter created with the ultra relativistic heavy ion collisions in terms of one- and two-particle spectra measurements.

History: Before the NA44 experiment starts, the NA35 group have reported an observation possible large long-lived pion sources in the central rapidities in 200 A GeV/c O+Au collisions [32]. The existence of a large long-lived particle source is thought to be a signal of QGP. Since the NA35 had not the particle identification (PID) at that time, they assumed negative hadron as negative pion. To confirm the NA35 result, the NA44 experiment was proposed with capabilities of the high speed data acquisition and the high momentum resolution with excellent PID by using a momentum focussing spectrometer. The NA44 collaboration was organized in 1989 and the experiment started with proton beam run in 1990. Following proton beam runs, the NA44 have experimented for S-S and S-Pb collisions until 1993. From 1994 to 1996, the Pb-Pb collisions were studied.

The characteristics of the NA44 spectrometer are summarized as;

- high momentum resolution ($\delta P/P \approx 0.2\%$)
- transverse momentum coverage is 0 to 1.6 GeV/c in mid-rapidity
- PID capability for charged hadrons ($\pi^\pm, K^\pm, p, \bar{p}, d$ and so on)

The acceptance of the NA44 spectrometer is shown in Fig. 2.2.

The spectrometer has capability of not only the two particles correlation but also the single particle spectra.

2.1.1 Set-up

Fig. 2.3 shows a schematic view of the NA44 set-up in 1995 for Pb beam runs. The spectrometer consists of three parts; the target area detectors, the magnets and the tracking/PID detectors behind the magnets. The following description of detectors is for the set-up in 1995 Pb beam.

The NA44 spectrometer has been experimented in proton-nucleus and sulphur-nucleus collisions until 1993. For the new lead beam collisions in 1994, the spectrometer has to be upgraded for higher multiplicities. The multiplicity counter at the target area was newly designed and installed. A scintillation hodoscope counter was replaced with a pad chamber to increase higher segmentation. For the particle identification, two new counters;

an aerogel counter and a special threshold imaging cherenkov counter were developed and installed.
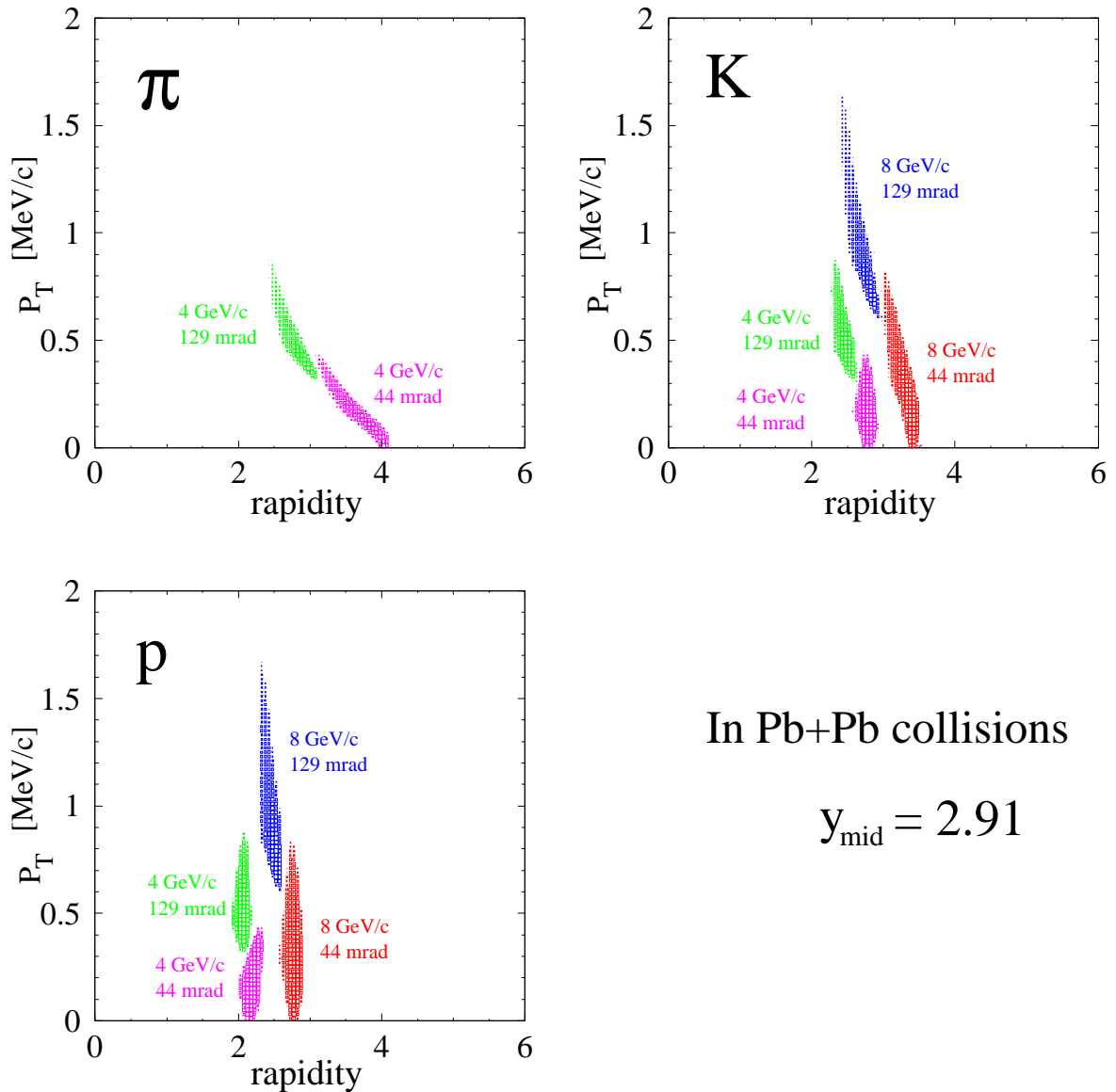
Figure 2.2: The NA44 acceptance of π, K, and p in the rapidity (y) and the transverse momentum (P_T) phase space for horizontal focussing setting.
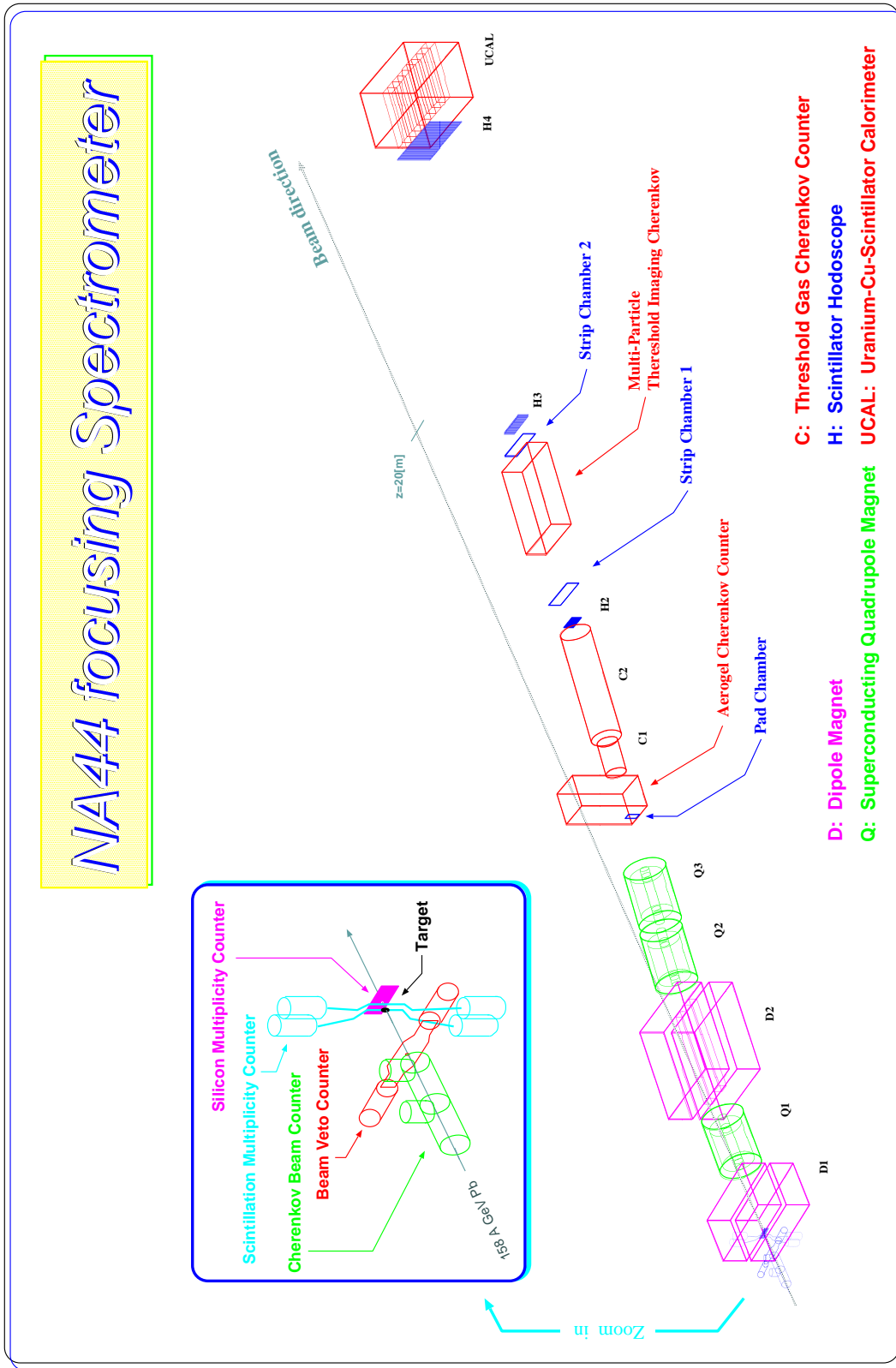
Figure 2.3: Schematic view of NA44 set-up for Pb95 runs. Please look at it with rotating clockwise.

2.1.1.1   Target area counters

A Cherenkov beam counter (CX) defines the start time for Time-Of-Flight (TOF) measurement with a hodoscope and counts the number of beam particles. The CX is a Cherenkov counter viewed with a high-speed photo-multiplier tube (PMT), and contains pure nitrogen gas as the radiator. The nitrogen gas was flowed in order to avoid radiation damage. The intrinsic time resolution are achieved to be 30 ps up to the beam intensity of $\sim 2 \times 10^6$ ions/s, where no sagging was observed in its pulse heights up to this high intensity. We have two sets of identical counters along the beam axis. More details are fond somewhere [33].

A CX-veto counter was placed behind CX to veto beam halo. This is a plastic scintillation counter viewed with two PMT's on both sides, and the scintillator has a hole to make heavy ion beams to pass through. CX and CX-veto define valid beam in trigger.
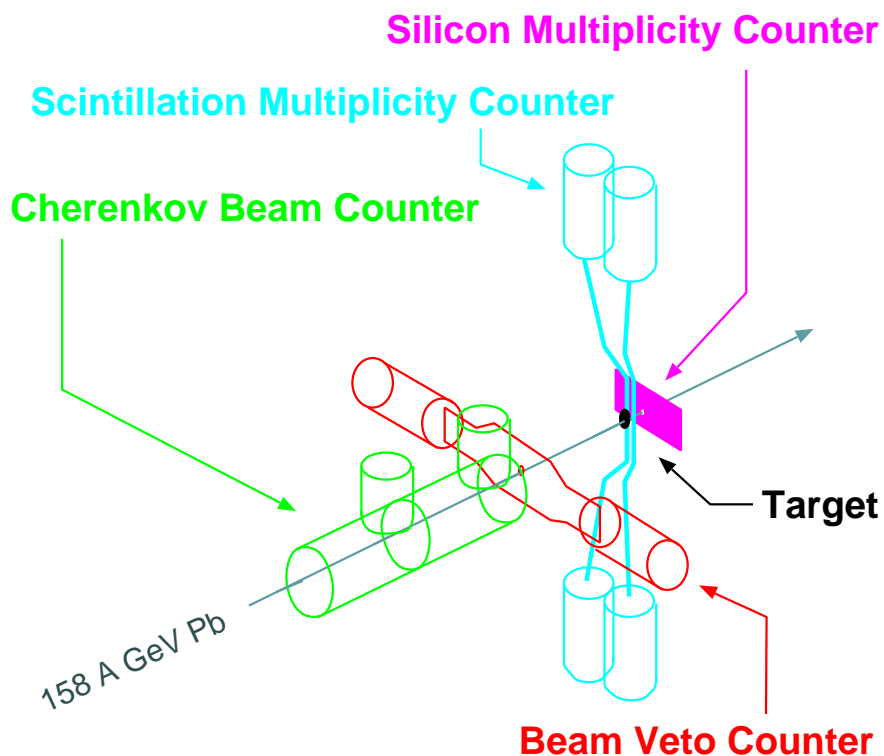
Figure 2.4: Schematic view of the target area counters

A target was put downstream of the CX-veto counter. A 2 mm thick Pb target disk of 10 mm in diameter was used in physics program for single particle studies.

To measure charged multiplicity, we had a scintillation multiplicity counter (T0) and a silicon multiplicity counter. The T0 counter consists of two identical scintillation counters. A counter is composed of a scintillator blade, two light guides and two PMT's. The light guides were glued on top and bottom surfaces of the scintillator block and two PMT's was attached on the both. T0 counter consists of four PMT's and they are called as T0-top-left, -top-right, -bottom-left and -bottom-right. The distance between the target and the scintillator is 10 mm. Beam particles not interacted with a target nucleus pass through the 3 mm gap between left- and right-T0 counters. However, when a beam particle interacts with a target nucleus, some of produced particles will be detected in either left- or right-T0 counters. The T0 counter was used in trigger to select high multiplicity events. The pseudo-rapidity acceptance range is $0.6 \leq \eta \leq 3.3$, which contains the mid-rapidity ($y_{mid} = 2.9$) of a Pb+Pb collision.

The silicon multiplicity counter covers the pseudo-rapidity region $1.5 \leq \eta \leq 3.3$. The counter is divided into 32 small pixels in azimuthal angles and in radial direction, respectively. Since the read-out speed from this semiconductor counter was slow, this counter was out of the trigger. The silicon multiplicity counter consists of two panels (see Fig. A.1 in Appendix A) and the signals from the counter are read out by identical circuits, separately. In 1995 run, we had a trouble of read-out circuits for one side of panel, and any pedestals and peaks corresponding to minimum ionizing particles (MIP) were not observed in a pulse height distribution from each pad (see Appendix A in detail). Therefore, in this thesis, I only used the information from the T0 counter to select the high multiplicity events.

2.1.1.2 Magnets

Two dipole magnets, D1 and D2 were used to select a momentum of particles produced by collisions. The nominal momentum settings were ± 2, ± 4, ± 6 and ± 7.5 GeV/c. The 7.5 GeV/c setting is called as the 8 GeV/c setting in this thesis.

Three super-conducting quadrupole magnets, Q1, Q2, and Q3 were used to focus the charged particles. The focussing capability allows the NA44 spectrometer to have an acceptance of one order higher than those without the quadrupole magnets. The focussing operation had two modes; horizontal and vertical focussing. The two focussing allow us to accumulate two particle spectra in a small momentum difference at very high statistics,

and make possible to study the two particle correlation in three dimensional space. The horizontal focussing were chosen for analyses of the single particle spectra, because it has a wider momentum acceptance than in the other setting.

2.1.1.3   Tracking/PID detectors

A pad chamber (PC), two scintillator hodoscopes (H2 and H3), and two strip chambers (SC1 to SC2) measure hit positions of charged particles. For particle identification of tracks in the trigger level, two threshold gas Cherenkov counters C1 and C2 are used.

2.1.1.3.1   Wire chambers, PC, SC1 and SC2   The technique of PC, SC1 and SC2 is based on multi-wire proportional chamber (MWPC). A basic configuration of MWPC is a plane of sense wires between two cathode planes in a gas filled column. When a charged particle pass through the detector, a shower of ionizing electrons in the chamber gas is detected with the anode wires. An MWPC can provide only one dimensional information of a track, then normally two MWPC's are used to detect the hit position in X-Y plane. In PC, one side of cathode planes is divided into small pads. The pad plane senses the total charge of the electron showers developed near an anode wire. By reading out the signals from all the pads, we are able to detect the hit position in an X-Y plane by single chamber.

Two strip identical chambers SC1 and SC2 were placed behind H2 and in front of H3, respectively. One SC consists of two chambers with two independent wire planes in horizontal (X) and vertical (Y) directions. A cathode plane was segmented into strips. The induced charge on vertical wires was read out by horizontal strips (SCH) and vertical strips (SCV) reads signals on vertical wires.

The parameters of the chambers are shown in Table 2.1. The Gassiplex read-out chips and the CRAMS modules were used to read their signals out [34, 35].

2.1.1.3.2   Hodoscopes, H2, H3 and H4   Two hodoscopes, H2 and H3 consisted of 60 and 50 scintillation counters, respectively. Two PMT's were attached on each the top and bottom ends of rectangular parallelepiped scintillator. The geometry of the scintillator rod was 6.0 mm tick, 6.0 mm wide, and 200.0 mm height for H2 and $13.1 \times 10.0 \times 220.0$ mm^3 for H3. The number of slats was used in the trigger to select a track multiplicity of the event in the spectrometer.

Table 2.1: Summary of pad and strip chamber parameters and resolutions. Reproduced from Ref. [34].

chamber	PC	SCH	SCV
acceptance (x×y) [mm^2]	128×216	768×256	768×256
number of channels	576×2	256	384
columns	32	4	192
rows	18	64	2
x-pitch [mm]	4.064	19.2	4
y-pitch [mm]	11.938	4	12.8
wire direction	horizontal	vertical	horizontal
number of wires	73	192	64
wire pitch [mm]	2.985	4	4
nominal voltage [V]	1850	1750	1750
x resolution [mm]	0.3	1.	0.3
y resolution [mm]	1.	0.3	1.
cathode plane	35μm Cu+Au on 1mm G10 board		
wire diameter	20μm W+Au		
wire tension	40-45g		
chamber gas	Ar/C$_2$H$_6$ 50/50		
transparency	<0.1 X$_0$		
read-out electronics	Gassiplex/CRAMS		

The hit position for horizontal (X) direction was corresponded to the position of counter. The Y position of the hit was reconstructed from time difference from the top and bottom PMT signals. Since the light velocity in each slat was calibrated in special runs, the Y position was given from the timing information. The average of top and bottom timing information of H2 and H3 was used for the stop information for TOF. The overall TOF resolution with CX and H3 was better than 100 ps. It has capability to separate π/K up to 4 GeV/c setting. H4 was set in front of Uranium calorimeter (UCAL), however, the track information on H4 was not added in the trigger.

Table 2.2: Cherenkov threshold in GeV/c for Pb95 run

	gas	Pressure [atm]	electron	pion	kaon	proton
C1	Freon 12	1.4	0.0	2.5	8.9	16.9
		2.7	0.0	1.8	6.4	12.1
C2	N_2/Ne	1.0	0.0	6.5	23.0	43.7
	N_2	1.3	0.0	5.2	18.3	34.8

2.1.1.3.3 Cherenkov counters, C1 and C2 Table 2.2 shows the threshold momenta for each particle in the C1 and C2 counters at different gas pressures. If the particle has a higher momentum than the threshold, it emits the cherenkov light. The role of C1 and C2 was to veto an event, which contains tracks of unfavoured particles in the event. For example, when we required 'C1 veto' in the trigger with the high C1 pressure in 4 GeV/c setting, the trigger is 'on' only for an event with no electrons. It means we have some chance to lose good events when other particles come into the spectrometer with an electron. However, this idea increases the confidence level of PID since these are no chance to miss-identify the particles as electron. I combined the PID information from the cherenkov counters with the PID from mass square measurement.

2.1.1.3.4 Aerogel counter An aerogel counter is set for π/K separation. It consisted of aerogel silica gel, a mirror for reflection of cherenkov light and a PMT. This counter was set and tested in 1995 run, however the detector was not fully understood. So it was not used in analyses of this thesis. The detail description of the counter is described in Refs. [36, 37].

2.1.1.3.5 Threshold imaging cherenkov counter The Threshold Imaging Cherenkov (TIC) counter was developed to identify particle species in multiple tracks. It is a part of up-grade project for Pb+Pb collisions. TIC has a container to fill cherenkov gas, mirrors set at ±45 degrees for X-Z plane and photon detectors. The index of the cherenkov gas was 1.0017, therefore it could separate kaon from pion in the momentum range of 2.2 to 7.9 GeV/c. The cherenkov light was reflected by the mirror and went into the photon detector. In 1994, we tested two types of photon detectors looking at to each mirror. One is a MWPC with CsI coated photo-cathode for photon conversion and the other is a MWPC with TMAE. The TIC measured cherenkov light from each track. In

data analyses, by combining the position of tracks and the TIC information, we could determine whether the track emitted cherenkov light or not. The detail description of the TIC is described in Refs. [38, 39, 40]. Since the photon detectors used in the 1995 runs were under developments, the TIC information was not used in the thesis.

2.1.1.3.6   Uranium scintillator calorimeter   The Uranium scintillator calorimeter (UCAL) was built for the R807(AFS) experiment at the CERN ISR [41]. In addition, it was used in the HELIOS (NA34) experiment. The main aim of the UCAL was to reject electrons from tracks, however, events that contained electrons in the reconstructed tracks were vetoed by C1 and C2 information, and the information was no applied to the analyses for this thesis.

2.1.1.4   A kind of slit, Jaws

A kind of slit to make acceptance small was introduced in 1994 runs and it was called Jaws.

The NA44 spectrometer was originally designed for S+A collisions. In Pb+Pb collisions, the multiplicity in a collision was expected to be one order higher than that in S+A collisions. Since the trigger for kaon and proton is given by veto of an event which has pion and electron in the C1 and C2 cherenkov counters, the probability to reject the events of containing pions decrease as increasing the multiplicity in the spectrometer acceptance. The Jaws was 'in' for kaon and/or proton runs to increase the event rate.

The material was an alloy of Tungsten (90%), Nickel(6%) and Copper(4%). The Jaws consisted of two slats; horizontal Jaws and vertical Jaws. The horizontal (vertical) jaws made the acceptance for y (x) direction narrow about one third (a half) times and was used for the horizontal (vertical) focussing mode.

2.2   Trigger system

The trigger signal was generated a coincidence of the valid beam, the T0 signal, one (two) or more hits in H2 and H3, and a signal from anode wires of pad chamber, vetoed by the Cherenkov counters, C1 and C2. Each trigger signal was prepared with NIM logic modules in the experimental zone, and was sent into the counting house. The coincidence of logic signals was made in the counting room and the trigger signals were recorded by

a DAQ system. The trigger signals are described in the following list.

valid beam (VB): Requirement of higher signals on both CX1 and CX2 than a pulse
height for delta electrons, and no signals seen on the CX-veto.

large signal on T0 counter (T0): The signal of each PMT was discriminated at a
threshold. The threshold was set to get a centrality of about 20 % of interaction.
The discriminated signals from four PMT's were sent to a coincidence module and
a 4-fold coincidence was required to generate the T0 signal.

multiplicity in the spectrometer (Mul1 or Mul2): A hit on a hodoscope was de-
fined as a coincident signal of the top and bottom PMT signals on a same slat. Two
types of trigger signals were prepared. One is Mul1, which requires at least one hit
in H2 and H3 respectively, and the other is Mul2, which requires at least two hits
in H2 and H3 respectively.

signal on the anode wire of pad chamber (PC): This trigger was adopted in 1994
for the Pb beam runs as an optional trigger and called as the PC trigger. The
idea was to guarantee on existence of tracks on the pad chamber and the anode
wire signals entered into a discriminator. This optional trigger was hoped to be
increasing efficiency of the multiplicity trigger.

PID: The trigger was given by signals from Cherenkov counters, C1 and C2. The trigger
mode had three types (require, veto and ignore).

The PC, Aerogel and H4 trigger were prepared as an optional trigger. As described
in the previous section, the Aerogel counter and H4 were tested during the 1995 runs,
therefore they were not in use for the physics runs. The PC trigger was used mainly for
'K/p' run. The data for single particle studies were taken with the trigger

$$VB \otimes T0 \otimes Mul1 \otimes PID (\otimes PC).$$

2.3   Data acquisition system

The trigger logic signals sent to the counting room were read out in a linear sequence via
CAMAC and VME (VERSE-module Europe) C-RAMS (CAEN Readout for Analogue
Multiplexed Signal). Until the 1994 run, we used a DAQ system based on a package
SPA/3W in an environment MAC-UA1 on a Macintosh computer (see Ref. [44] in detail).

In 1995, the DAQ system was moved to an environment with CASCADE (CERN Architecture and System Components for an Adaptable Data acquisition Environment), and the control and monitoring systems were exchanged to HP work station and X-terminal. The hardware of the DAQ was housed in a VME crate. A FIC (Fast Intelligent Controller, CES FIC 8234 a Motorola 68040 single processor VME board) module is operated by OS-9/68K. The HP workstation was used for a file server of the FIC, remote monitoring and run controls. The data trigger signal enter a VME interrupt module (CORBO unit) SPS accelerator start-of-burst (SOB) and end-of-burst (EOB) signals are accepted by CORBO. The signals from CORBO are transferred FIC by the VME bus. The data from TDC and ADC modules, for example, were read out through the VME C-RAMS and CAMAC, and they were stored in a temporary buffer on the FIC. The data on the buffer was written on a magnetic tape between beam bursts. The total read-out time for the entire stage process was approximately 800μsec per event.

This section is based on Ref. [42]. Please see the reference to know detailed description about NA44 DAQ system.
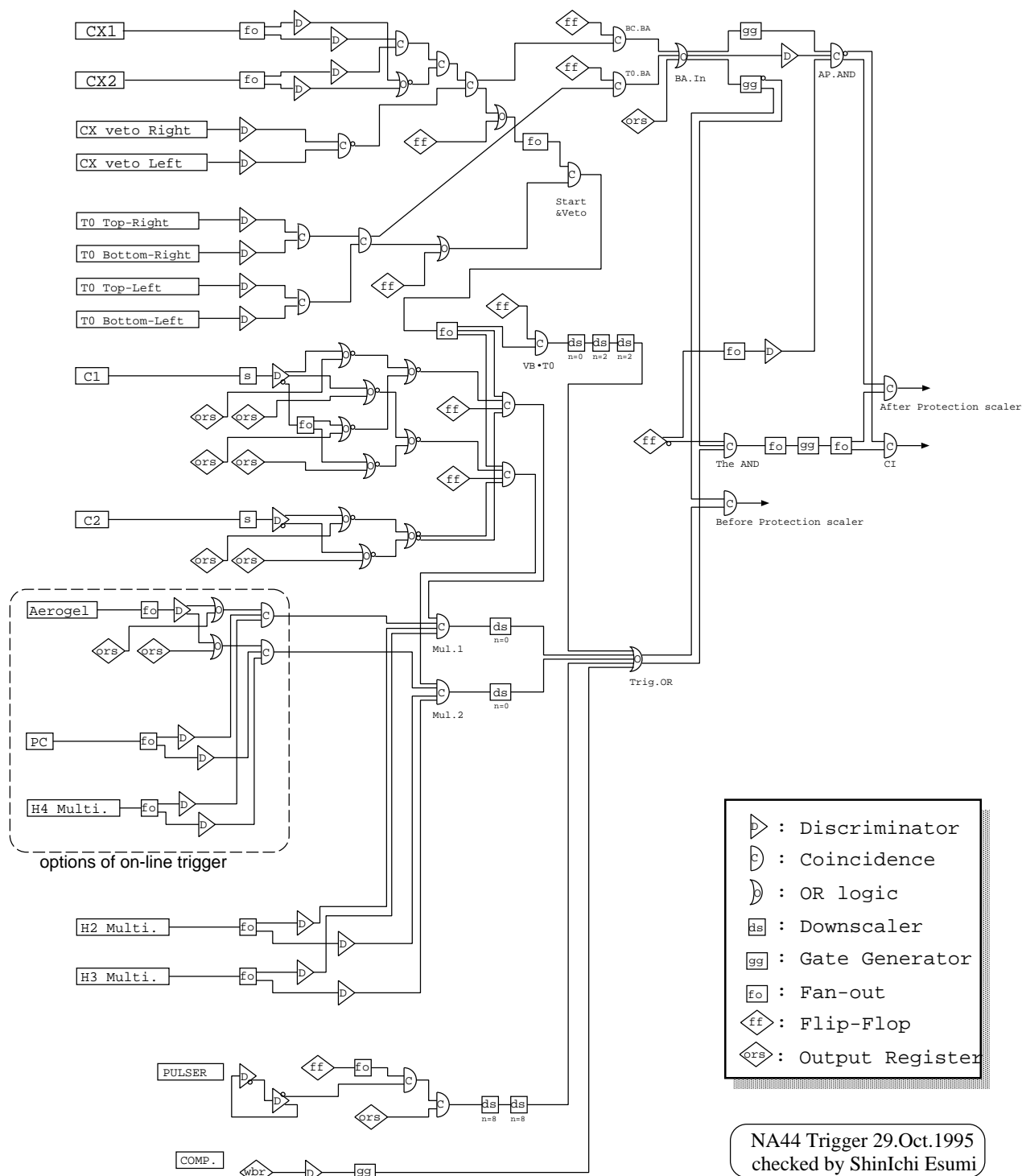
Figure 2.5: Logical diagram of NA44 trigger. The output register and the flip-flop modules are used as switch operated from DAQ system.

Chapter 3

DATA ANALYSIS

This chapter describes analysis procedures. All the detectors need to be calibrated on their time and position. Calibration procedures for CX, H2, H3 and tracking chambers, which were used in data analysis, will be described. After the calibration process, the DST (Data Storage Tape) program will construct particle tracks in the spectrometer by reading their hit positions from the tracking detectors, and calculate the TOF value for each track from time informations recorded in the hodoscopes and CX counter. The program also calculate the three dimensional momenta of each track from the bending angle in the dipole magnets and the off-set angles from the medium plane. The program save these informations, including scalar numbers that were recorded in the raw data tapes, into a data storage tape. It is a reason why one calls the DST for this program.

Since the DST process has been established in the NA44 collaboration, my major contribution is to consider how to select events from the DST data and correct physics data for various effects from spectrometer acceptance and physical backgrounds. The acceptance correction factor was evaluated by a Monte-Carlo (MC) simulation. The absolute cross-section was derived from scaler informations of the number of valid beam, number of interaction, number of trigger presented, and number of trigger accepted.

The NA44 spectrometer has no vertex detectors at the target region. The cross-section has effects of contamination of particles decayed from short-lived particles, such as Λ, Σ, and so on. Considering the particle ratio estimated from an event generator RQMD(v2.3) [43], the contamination from Λ^0 ($\bar{\Lambda}^0$) and Σ^+ ($\bar{\Sigma}^-$) decays for the protons (antiprotons) were from not to be ignored in the proton samples. The effect was estimated from the MC simulation assuming the momentum distribution and yield calculated from the RQMD. Finally, the absolute cross-sections will be shown in the last section of this chapter.

3.1 Detector calibrations

3.1.1 Beam counter and hodoscope calibration

As described in section 2.1.1, the combination of the cherenkov beam counter CX and the hodoscopes provide us Time-Of-Flight information which will be used for PID. The CX counts a beam particle and the hodoscope information give hit positions of the secondary particles. The pulse height of PMT's varies due to different gain of the PMT. The calibration needs for ADC gain, TDC gain and pedestal of ADC signals of the CX and the hodoscopes. The hodoscope needs the other calibration procedure to provide a vertical hit position along a slat and to correct the 'slewing' effect to achieve the best timing resolution from each slat.
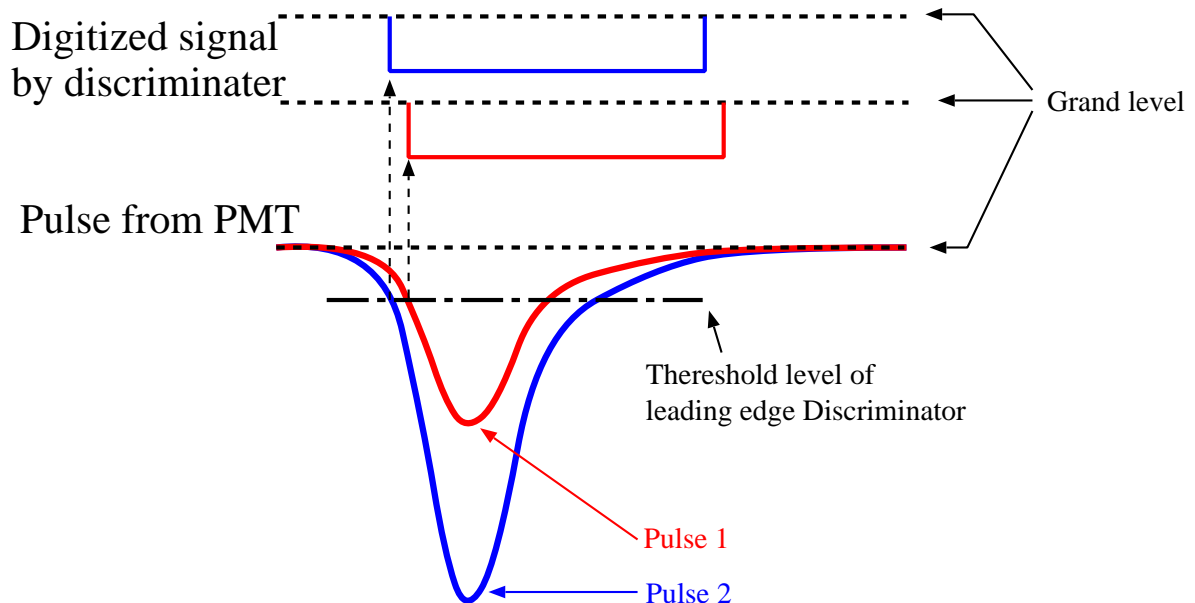
Figure 3.1: Schematic figure of the slewing effect. The output timing from a leading-edge discriminator varies with the different pulse height of PMT signals even these signals are generated at the same time when a particle pass through a scintillator. The horizontal axis is time and the vertical axis is voltage.

Fig. 3.1 shows output signals from a leading-edge discriminator with different pulse heights at the input. The threshold level of the leading-edge discriminator is set to reject thermal noises. The timing of output signal from pulse 1 is different from one from pulse 2 even if the both pulse 1 and 2 are generated at the same time. The smaller pulse height creates a slower output signal from the discriminator.

Correction for the slewing effect followed the standard method [45, 46]. TOF is defined as subtraction of the TDC value of the CX from the arrival time at a slat of hodoscope. Corrected time, TOF_{corr} is defined as

$$\text{TOF}_{corr} = \text{TOF} + \sum_i \frac{A_i}{\sqrt{\text{ADC}_i}} \tag{3.1}$$

$$i = \text{top and bottom PMT's of a slat}$$

for each slat, where A_i is a constant which is to be calibrated for PMT by PMT and ADC_i is ADC value, measured with each PMT.

The calibration process of the hodoscopes and the CX was done simultaneously by the program called PASS. The PASS has four procedures PASS1 to PASS4 to get the final calibration constants.

PASS1: PEDE, TOF1, TDIF, and YVEL
PASS2: SLEW
PASS3: SLEW
PASS4: GAIN, TOFS, and YOFF

Each step of the PASS procedure will be described in the following subsection.

3.1.1.1 PASS1

The PEDE is a pedestal value of ADC channel for each PMT of the CX and the hodoscopes. The pedestal value is an integrated current at the ADC channel with no inputs from the PMT. The pedestal is not the same for all the channels and then it is necessary to calibrate the pedestal for all the channels.

The raw Time-Of-Flight TOF_{raw} is defined as the following.

$$TOF_{raw} = TDC_{hod} - TDC_{CX} \quad \text{for each slat of hodoscope}$$

where

$$TDC_{hod} = \frac{TDC_{top} + TDC_{bottom}}{2} \quad \text{for each slat of hodoscope}$$

$$TDC_{CX} \;\; = \;\; \frac{TDC_{CX1} + TDC_{CX2}}{2}$$

The TDC_{hod} is defined as an average of valid TDC values of the top and bottom PMT's. The TDC_{CX} is defined as an average of valid TDC values of the CX1 and CX2. Valid TDC values are defined by a condition that two TDC values from the top and bottom PMT's in a slat droops in a physical TDC region. The calibration constant TOF1 is defined as a peak position of TOF_{raw} fit by a gaussian distribution.

The three finger counters prepared for the vertical position calibration along y direction on a hodoscope. The y position along a slat is proved from the time difference between the top and bottom PMT's. To reconstruct the y position from the time difference, we need to know the time offset to each TDC value and the light velocity in each slat of the hodoscopes. Fig. 3.2 shows schematic view of the finger counters and a slat of a hodoscope. The TDIF is given as time difference requiring a valid hit on one finger
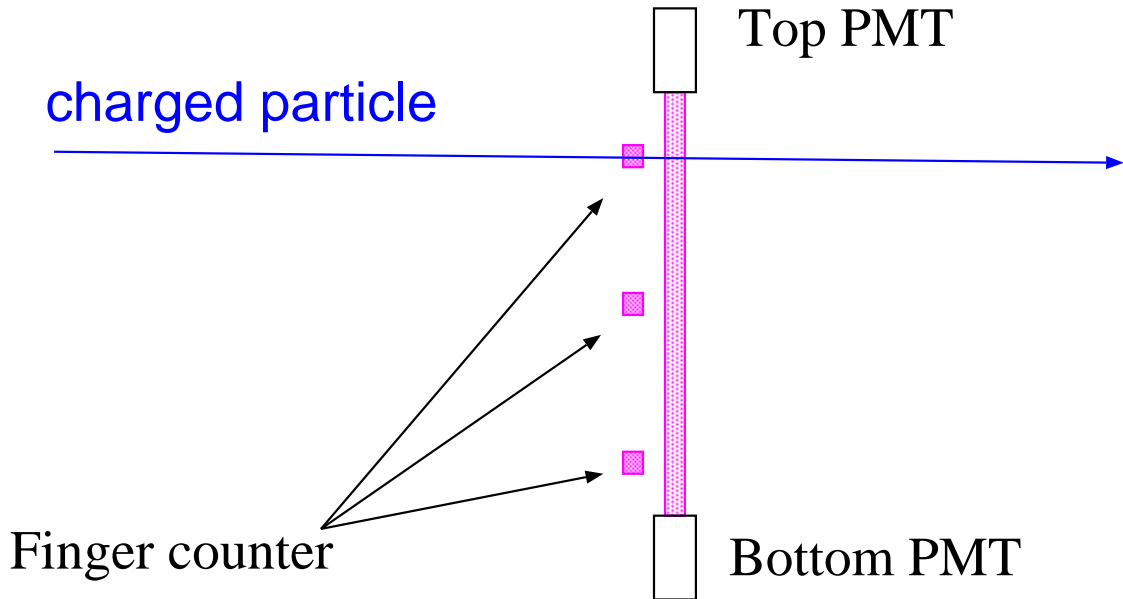
Figure 3.2: Schematic view of hodoscope as side view for calibration of TDIF. The slat of hodoscope puts vertically and two PMT's are connected on top and bottom of the rod. The three finger counters, top, centre and bottom, are in front of the slats horizontally. Two PMT's are connected at both edges of scintillator rod and called left and right PMT of the finger counter.

counter, where there the valid hit on the finger counter is defined requiring valid ADC signals from both the right and left PMT's of the finger counter. From the three TDIF's; $TDIF_{top}$, $TDIF_{centre}$ and $TDIF_{bottom}$, the light velocity YVEL is given by

$$\text{YVEL} = \frac{1}{2} \left(\frac{\text{length of centre to top finger}}{TDIF_{top} - TDIF_{centre}} + \frac{\text{length of centre to bottom finger}}{TDIF_{bottom} - TDIF_{centre}} \right)$$

The y position along a slat is reconstructed from the time difference of the top and bottom PMT's of the slat with using the calibrated value of YVEL for the slat.

3.1.1.2 PASS2 and PASS3

The PASS2 and PASS3 are exactly the same process and these are corrections for the slewing effect in the TOF spectrum. The slew-corrected TOF is given in equation (3.1), and parameters to be calibrated are A_i. They are given by fitting of a scatter plot of TOF_{raw} as a function of ADC value with the equation (3.1). The values of SLEW are recorded in a calibration database and the process PASS3 starts from these constants as the initial values. Since this correction process can not be done in any analytical procedures, the program automatically finds the calibration constants in the iterative method. We fond the method of iteration needs to be two, but do not need more than that.

3.1.1.3 PASS4

The ADC gain calibration constant, GAIN is given from a peak channel for MIP after pedestal subtraction. Since the NA44 experiment measures of particle correlations of two tracks close to each other, it is important to distinguish double hit slats from others.

The TOFS is the peak position of the TOF corrected for the slewing effect. The TOF stored in DST data is not equal to the real Time-Of-Flight from the start counter to the stop counter, but contains some offset time that we do not know. Therefore we stored the TOF information as H3TOF (TOF on H3) for each slat defined with,

$$\text{H3TOF} = TOF_{corr} - TOFS.$$

Also TOF on H2, H2TOF for each slat is defined in the same way. The distribution of TOF_{corr} depends on a trigger setting. In the event with the C1-ignore and C2-ignore setting at the +4 GeV/c setting, for example, we see a large peak by electrons and pions. On the other hand, the C1-veto and C2-veto at +4 GeV/c setting makes two peaks in the

H3TOF distribution contributed by kaons and protons. The PASS4 has an option which select the (first or second) peak to be fit by a gaussian and to be adopted as the value of TOFS. The TOFS is sensitive for the trigger setting of the C1, C2 and momentum setting, therefore the PASS4 process was carried out every two or three runs.

The y position calibration was made for each slat of the hodoscopes. The y position was calibrated with requiring hits on one of three finger counters. The YOFF is defined as a peak position of the raw y position with hit on the centre finger counter.

3.1.2   Chamber calibration

The calibration for the pad and two strip chambers aims to do correction for non-linearity and gain of the read-out electronics and for to reject noisy chambers. The detailed description of the calibration procedure are given in Ref. [34].

3.2   Geometry data of NA44 spectrometer

The geometry of the spectrometer was given by surveyors. The survey was done before the beam time and in a day when the spectrometer angle was changed. The data from surveyors are converted to a geometry data file, called GEOM.DAT, written by GEANT3 [48] format. The geometry information in GEOM.DAT was finally tuned to get the highest efficiency in a routine of track reconstruction.

3.3   DST - Data Storage Tape

The DST program reconstructs particle tracks in the spectrometer, and calculates momenta and TOF and saved the data with some raw data from detectors and scalers. The data was written in the CWN (Column-Wise-Ntuples) [47].

3.3.1   Track and momentum reconstructions

The hit positions on PC, H2, H3, SC1 and SC2 were used to reconstruct tracks. Since the tracking area has no magnetic field, the charged particle should pass straight. The track was reconstructed from hit positions on the tracking detectors by fitting them with

Table 3.1: Particle species for the peak of TOF for various momentum, C1 and C2 setting in trigger. (1): Since Kaon TOF peak of low momentum is close to pion peak, it is seems to be shoulder on the pion tail. (2): The peak of the TOF is hidden in tail of pion TOF due to lower statistics than pion.

trigger setting			particle species	
C1	C2	momentum	the first peak	second peak
ignore	ignore	$+4$ GeV/c	e^+ and π^+	K^+ or p [1]
veto	veto	$+4$ GeV/c	K^+	p
ignore	ignore	-4 GeV/c	e^- and π^-	- [2]
veto	veto	-4 GeV/c	K^-	$\bar{p}$
ignore	ignore	$+8$ GeV/c	e^+ and π^+	p
ignore	veto	$+8$ GeV/c	K^+	p
ignore	ignore	-8 GeV/c	e^- and π^-	- [2]
ignore	veto	-8 GeV/c	K^-	- [2]

a line using the χ^2-minimum method.

After fitting, the track candidate was compared with a lock-up-table to check whether the candidate can come from the target. A Monte-Carlo simulation program simulates various charged particles with different momenta passing through the magnet field and the tracking region. The correction of three dimensional momenta of the particle and hit positions at tracking detectors were stored in a look-up-table.

3.3.2 Calculation of mass square

The mass square was calculated from the momentum and TOF information of the track. As described in sub-sub-section 3.1.1.3, the H2TOF (H3TOF) in DST data is not absolute Time-Of-Flight from the time when the particle created in the target to the time when the particle pass through H2 (H3). The first or second peak of H2TOF (H3TOF) was adjust to 0 ch. We can assign a particle species for the peak in the TOF spectrum by considering the setting of magnet and cherenkov detector C1 and C2 in the trigger as shown in Table 3.1.

The mass square is given as a function of momentum p and velocity β.

$$m^2 = \frac{(1-\beta^2)}{\beta^2} p^2 \tag{3.2}$$

The velocity β is a function of H2TOF (H3TOF), a momentum and a flight pass from the target to the hodoscope 2 (3).

$$\frac{1}{\beta} = \frac{U_{TDC}}{c} \frac{\mathrm{H}n\mathrm{TOF}}{PATH_n} + \frac{\sqrt{m_{calib}^2 + p^2}}{p} \tag{3.3}$$

where U_{TDC} is time in the unit of TDC channel (50 ps/ch), c is the light velocity, the suffix n is 2 for H2 and 3 for H3, HnTOF is TOF on the hodoscope n in the DST data and the unit is TDC channel, $PATH_n$ is the path length from the target to the hodoscope n, and m_{calib} is the mass of particle of which the peak was adjusted to be 0 ch.

3.4   Cuts for event selection and correction factors

The event selection was made requiring high multiplicity event. To select high multiplicity events, the T0 pulse height information was used. The informations from the cherenkov counter C1 and C2 and the TOF value gave us the identification of particles in interest. A severe cut guarantees the higher quality of the particle identification of a spectrum, although it removes some events that have to be counted in the spectrum. Therefore, it is necessary to estimate the correction factor for the lost events by the cut. In addition to this, there are inefficiencies in the detectors and the trigger circuits. The H2 had some noisy photo-multiplier tubes and made some 'fake' hits in the trigger. The H2 efficiency was studied by John P. Sullivan. Another problem was inefficiencies of the PC chambers. The PC trigger efficiency is studied by comparing events within the PC trigger to without the PC trigger.

3.4.1   Double beam cut

The beam particle was counted with the CX counter. Sometime we observed a very bad time structure of the beam in beam spills, therefore there was a certain probability to count two or more beam particles with the CX counters in a gate of the trigger. The CX counter generates the start timing signal for the beam particle arrived first, however, there is a fair chance that the first particle does not collide with a target nucleus, but the second beam particle collide with a target nucleus. The TOF information will be

degenerated due to the time difference of the arrival time. Furthermore, we will not be able to distinguish whether one of the beam particles collides with a target nucleus or both the beam particles accidentally collide with target nuclei independently. Such events deform the single particle spectrum in the spectrometer. Therefore, multiple beam events have to be rejected.

Fig. 3.3 shows a scatter plot of pulse height of CX1 and CX2. The clusters in the plot show single-, double- and triple-beams entering in a gate. A good correlation between the ADC's measured with the CX1 and CX2 is seen. In this analysis, the single beam event was selected as shown by a box in the left-bottom region.
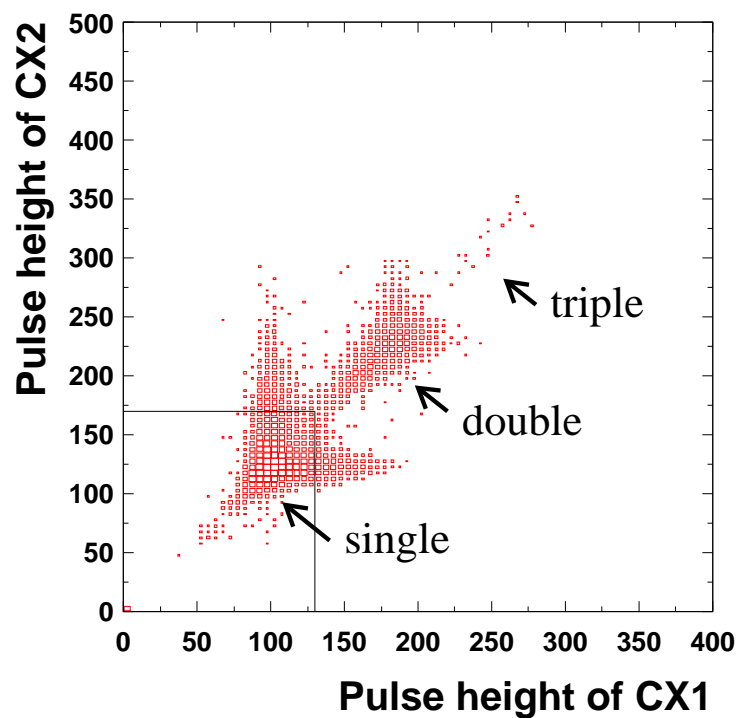
Figure 3.3: Scatter plot of pulse height from CX1 and CX2. The scale of z direction is logarithm.

Table 3.2: The threshold of CX for double beam cut and the correction factor.

trigger setting				threshold [ch]		correction
momentum [GeV/c]	angle [mrad]	C1	C2	C1	C2	factor
+4	44	ignore	ignore	145	180	1.038±0.003
+4	129	ignore	ignore	145	200	1.056±0.003
-4	44	ignore	ignore	145	200	1.045±0.003
-4	129	ignore	ignore	145	210	1.057±0.003
+8	44	ignore	ignore	145	180	1.036±0.003
+8	129	ignore	ignore	145	200	1.047±0.003
-8	44	ignore	ignore	145	200	1.053±0.003
-8	129	ignore	ignore	145	210	1.058±0.003
+4	44	veto	veto	140	180	1.061±0.002
+4	129	veto	veto	140	200	1.063±0.004
-4	44	veto	veto	140	180	1.090±0.003
-4	129	veto	veto	140	200	1.076±0.004
+8	44	ignore	veto	140	180	1.051±0.002
+8	129	ignore	veto	140	190	1.060±0.002
-8	44	ignore	veto	140	210	1.065±0.002
-8	129	ignore	veto	140	210	1.069±0.003

The threshold values were fixed for the same setting of momentum, spectrometer angle, and cherenkov detectors. The correction factor for the CX cut was given by a ratio of the number of events rejected to the number of events selected. They and the correction factors are shown in Table 3.2 The absolute normalization was made with informations from scalers and the number of beam used in the analyses.

3.4.2 Centrality defined by T0 counter

The T0 counter has four PMT's. The pulse height distributions from the PMT's for the VB run and these in the VB⊗T0 trigger are shown in Fig. 3.4 at the +4 GeV/c setting and in Fig. 3.5 at the -4 GeV/c setting. Delta-electrons created in the target due to the electro-magnetic interactions with the large change of the beam nucleus were bent to the left-hand (right-hand) side by the magnetic field of the D1 magnet in the positive (negative) momentum setting.

T0 ADC, +4GeV 44mrad
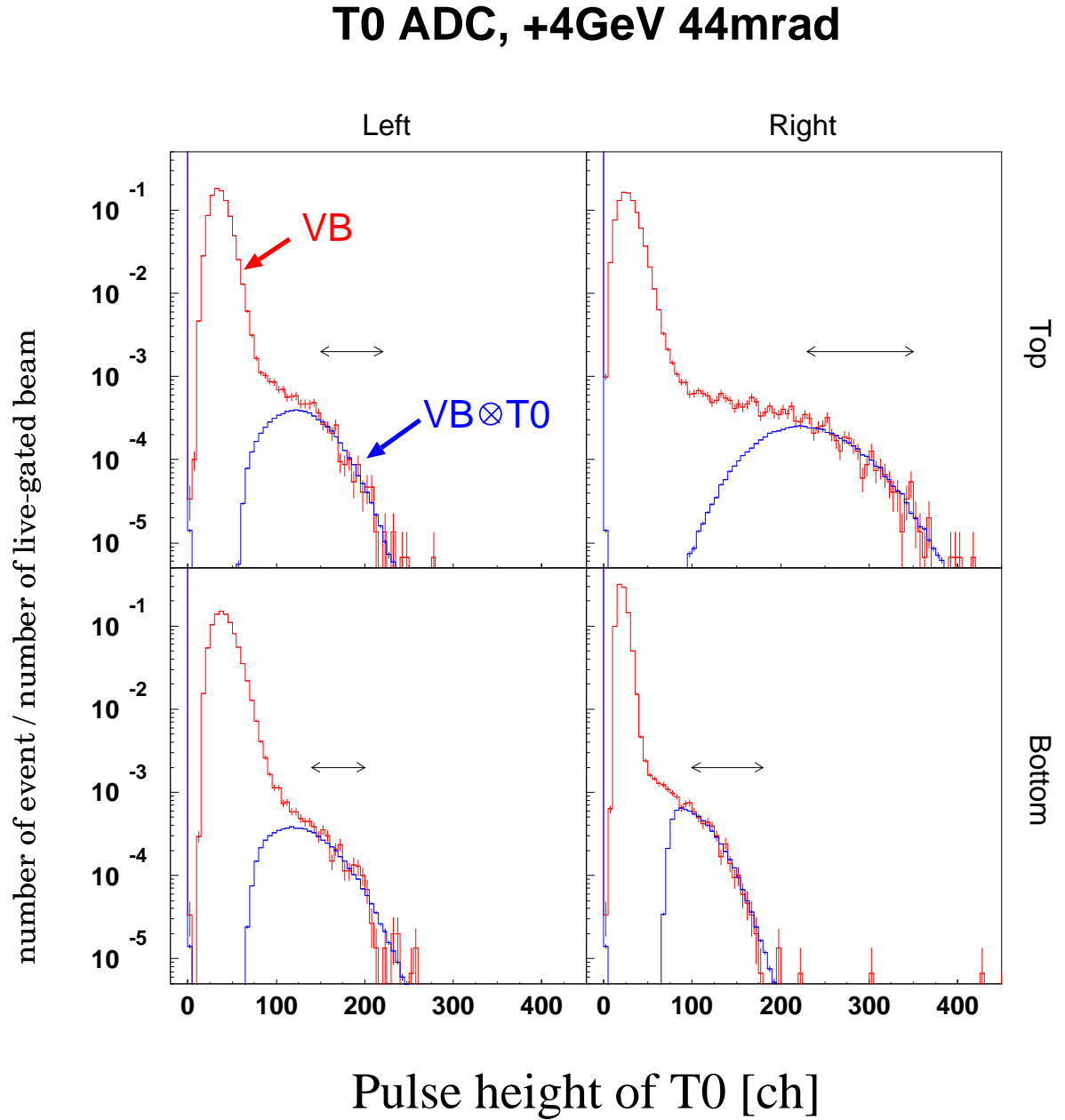
Figure 3.4: T0 pulse height distributions of VB and VB⊗T0 run for +4 GeV/c setting. The VB⊗T0 run is required high multiplicity event with higher pulse from T0 counter than threshold. The horizontal axis is pulse height of each PMT of T0 and the vertical axis is number of event normalized by live-gated beam. The horizontal arrow in the plot shows a fitting range for shoulder T0 distribution of VB⊗T0 to one of VB run.
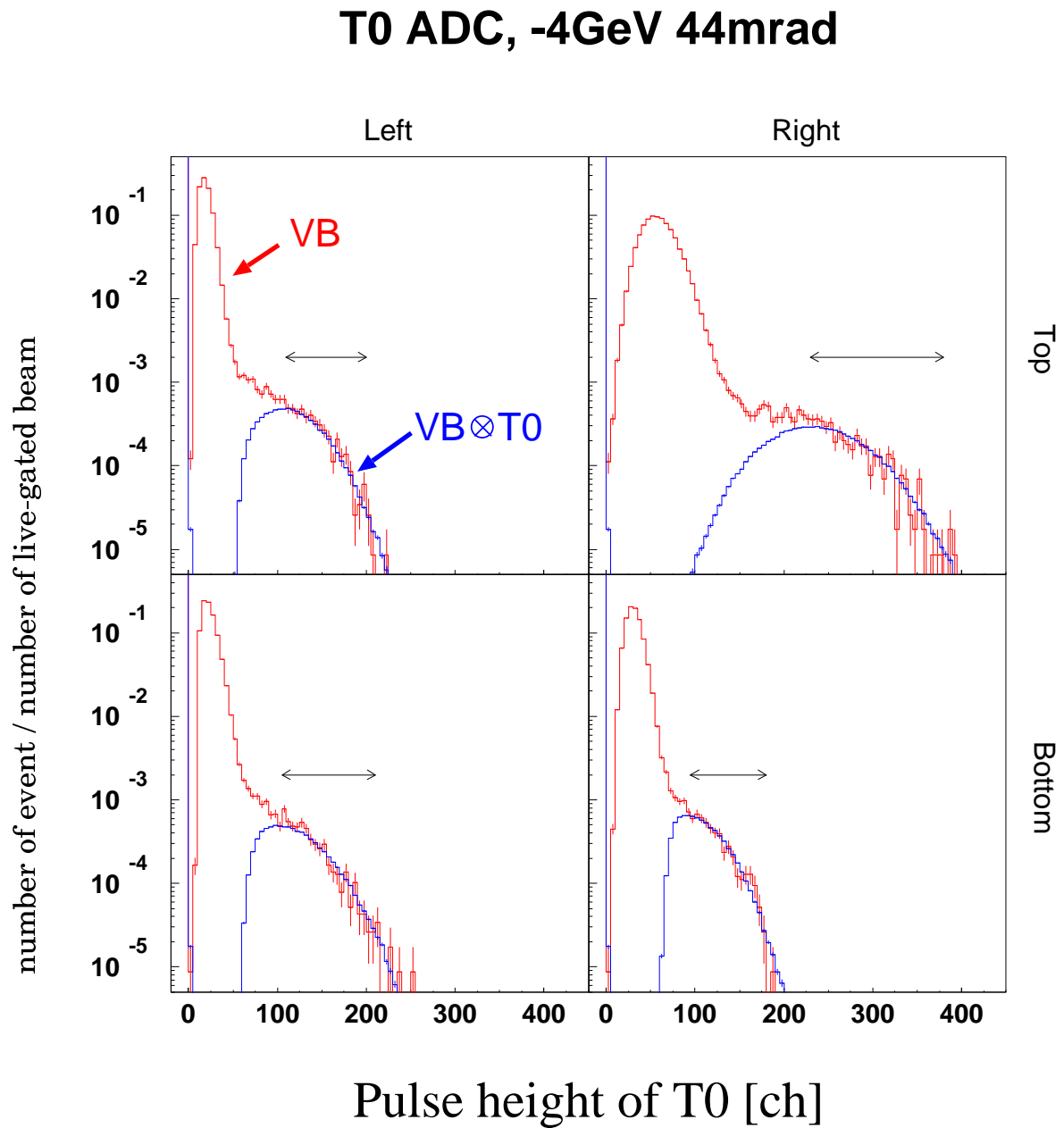
Figure 3.5: Same kind of plot with Fig. 3.4. These are for -4 GeV/*c* setting. We can see that the effect of delta-electron for the width of peak of T0 distribution for VB run are different from +4 GeV/*c* setting.

Since the delta-electrons are emitted independently on nuclear collisions of the beam particles, the effects to the T0 signals are similar to thermal noises. Therefore, the T0 counter in the side of delta-electron has a wider pulse height distribution compared to that of the other side.

The definition of centrality for the physics run was given as the ratio of T0 pulse height distribution from physics runs to one from the VB run. The VB trigger did not require interactions in the target, and the physics run requires interactions with high pulse heights in the T0 counter. The discriminator threshold in the T0 counter was fixed during one physics program. The calculation of centrality in the VB⊗T0 trigger run is the figures.

The centrality σ_{trig} was defined as the following.

$$\sigma_{trig} = \frac{A_{VB \otimes T0}}{A_{VB} \times \lambda} \tag{3.4}$$

where $A_{VB \otimes T0}$ means the number of events of VB⊗T0 runs normalized by the number of live-gated beam, and A_{VB} is the number of events of VB runs normalized by the live-gated beam. λ is the interaction probability of the beam particle in the target. The value of λ is given by scaling of the interaction probability of the p+Pb collisions to one of the Pb+Pb collisions by a geometry factor.

The nuclear interaction length of Pb is 194 g/cm^2 and the density of Pb is 11.35 g/cm^3. The physical thickness of a Pb plate that occurs a nuclear interaction of p+Pb collisions at 100% probability is calculated as,

$$\frac{194}{11.35} = 17.09 \text{ (cm)}$$

The geometry factor to convert the interactions from p+Pb to Pb+Pb is

$$\frac{(\text{Pb+Pb})}{(\text{p+Pb})} = \frac{(208^{\frac{1}{3}} + 208^{\frac{1}{3}})^2}{(1^{\frac{1}{3}} + 208^{\frac{1}{3}})^2} = 2.928$$

Since the thickness of target is 2 mm, the interaction probability of the Pb+Pb collisions in the target is

$$0.2/17.09 \times 2.928 = 0.034$$

The normalization by live-gated beam counts was done by summing a variable SCBCL in the DST data. Since the DAQ system had a dead time by the hardware design and software speed, it was necessary to record number of beam particles passing through the CX1 and CX2 in the DAQ live-gated time. If the scaler of the SCBCL records the number of particles perfectly, the shoulder of the T0 pulse height distribution in the VB⊗T0 run should match to the shoulder of the VB runs.

Table 3.3: A parameter for fitting shoulder of the T0 pulse height distribution of the VB⊗T0 runs to the shoulder from the VB runs and the trigger centrality for each setting. The error of the centrality is from statistical error and fitting of the shoulder of the pulse height distribution.

trigger		fitting constant	trigger centrality [%]
momentum	angle		for VB⊗T0 run
+4 GeV/c	44 mrad	1.037±0.024	17.11±0.40
+4 GeV/c	129 mrad	1.097±0.025	22.59±0.52
-4 GeV/c	44 mrad	1.182±0.024	20.35±0.42
-4 GeV/c	129 mrad	1.009±0.022	18.79±0.42
+8 GeV/c	44 mrad	0.972±0.025	18.93±0.49
+8 GeV/c	129 mrad	1.108±0.021	23.66±0.46
-8 GeV/c	44 mrad	1.147±0.022	20.80±0.41
-8 GeV/c	129 mrad	1.115±0.026	29.49±0.46
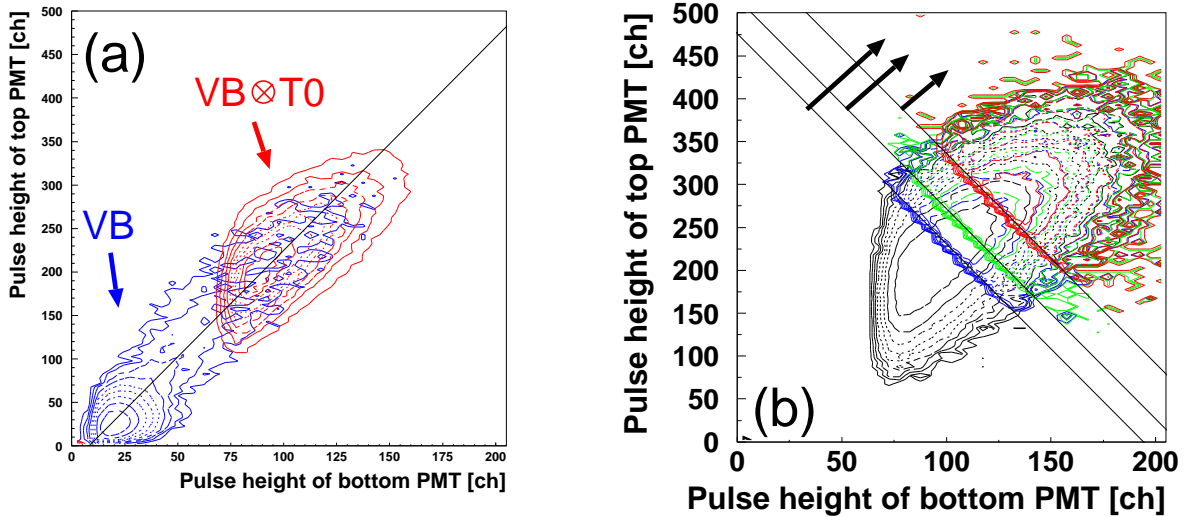
Figure 3.6: Contour plot of pulse height from top and bottom PMT's For the detail description about lines, see text.

Table 3.4: Parameters for centrality selection by T0 counter. The condition is given by $y \geq -a \times x + c$, where a and c are constants, y and x are T0_S_ADC(4) and T0_S_ADC(3) for positive momentum setting, T0_S_ADC(2) and T0_S_ADC(1) for negative momentum setting, respectively. T0_S_ADC is variable in the DST ntuple.

trigger setting		parameters			
momentum	angle	a		c	
			σ_{trig}=3.7%	7.4%	10.5%
+4 GeV/c	44 mrad	2.45	581.0	516.5	475.9
+4 GeV/c	129 mrad	1.20	454.5	405.3	373.5
-4 GeV/c	44 mrad	0.97	293.5	259.0	237.5
-4 GeV/c	129 mrad	0.50	224.0	196.5	179.5
+8 GeV/c	44 mrad	1.20	421.0	370.5	337.8
+8 GeV/c	129 mrad	1.20	445.1	395.0	363.0
-8 GeV/c	44 mrad	0.97	295.3	259.4	237.4
-8 GeV/c	129 mrad	0.50	227.0	200.0	183.6

To check the normalization using SCBCL, the T0 pulse height distributions from the VB⊗T0 runs were compared with those from the VB runs in Fig 3.4 and Fig. 3.5. The T0 has four PMT's and the gain of PMT's were different. However, the inefficiency of scalars should not depend on the gains, so the fitting was made for the 4 PMT's simultaneously with one fitting parameter. The fit range are shown in Fig. 3.4 and Fig. 3.5.

As shown in Table 3.3, the fit parameters are not constant among different trigger conditions. The trigger centrality for each spectrometer setting was obtained using the equation (3.4) with the fitting parameters. They ware about top 20% of minimum bias interactions for every setting, and it was the value that we planed.

For further analyses looking same physics observation as a function of the collision centrality, I need to describe how I divide this top 20% events into several group at different centralities. As described in precious subsections, we saw a large flux of delta-electrons in one slat of T0 counter, which always left side when the magnet polarizing was positive. However, we saw less effect on the other slat of the T0 counter. In order to remove the effect of delta-electrons, I used data from slat in the delta-free side to evaluate centrality event by event.

A T0 slat has two PMT's on the top and bottom ends. A scatter plot of the left-hand side in Fig. 3.6 shows a correlation of the T0 top and bottom ADC's for the VB and VB⊗T0 runs. The centrality selection was made in the following procedure.

A line $y = a{\times}x + b$ which pass at the both ADC peaks of the VB run and peak of VB⊗T0 run was drawn in the Fig. 3.6 (a). Another line $y = -a{\times}x + c$ which crosses the line at right angle was drawn in the Fig. 3.6 (b), where the parameter a corresponds to a factor of gain correction for the PMT's. The events were selected by a condition $y \geq -a{\times}x + c$ to tag them the centrality above a certain value. The parameter c was calibrated to get 3.7, 7.4 and 10.5% centrality, and found in Table 3.4.

The method to calculate the centrality needs stable operation of PMT's during runs, since the centrality is sensitive to the PMT gain. We observed a T0 gain shift during the Pb beam runs due to probably radiation damage of scintillators, however, from a study of T0 gain shift by Texas group, it was indicated that the gain shift was several percent through entire beam time. The effect was expected to be small.

3.4.3   Particle identification by Cherenkov counters

The gas cherenkov counters C1 and C2 were employed to identify particle species for reconstructed tracks. The idea to employ two cherenkov counters is to tag each track with three categories. We expect electrons, pions, kaons and protons as stable or relatively long-lived particles in the spectrometer. In case of 4GeV/c setting, we operated these two cherenkov counters to separate electron and pion from others, since the K/p separation could be made with TOF measurement. In case of two or more particles events in the counters, we basically lose the particle identification capabilities. Because we can not distinguish which particle is find and is to assign the particle species. In this analysis, I used only the event with a single track, so the multi-particle problem would not happen. However, the particles in the multi-particle events need to add in the signal particle cross section. This fraction will be corrected in the next session.

To increase the event rate of kaon and protons for beam time, we had K/p runs by vetoing the electrons and pions by cherenkov counters in the trigger level. The particle yield and the momentum distributions of kaons and protons are made from the K/p runs. However, the kaons and protons in e/π/K/p runs are used for estimations of some correction factors, which will be described later.
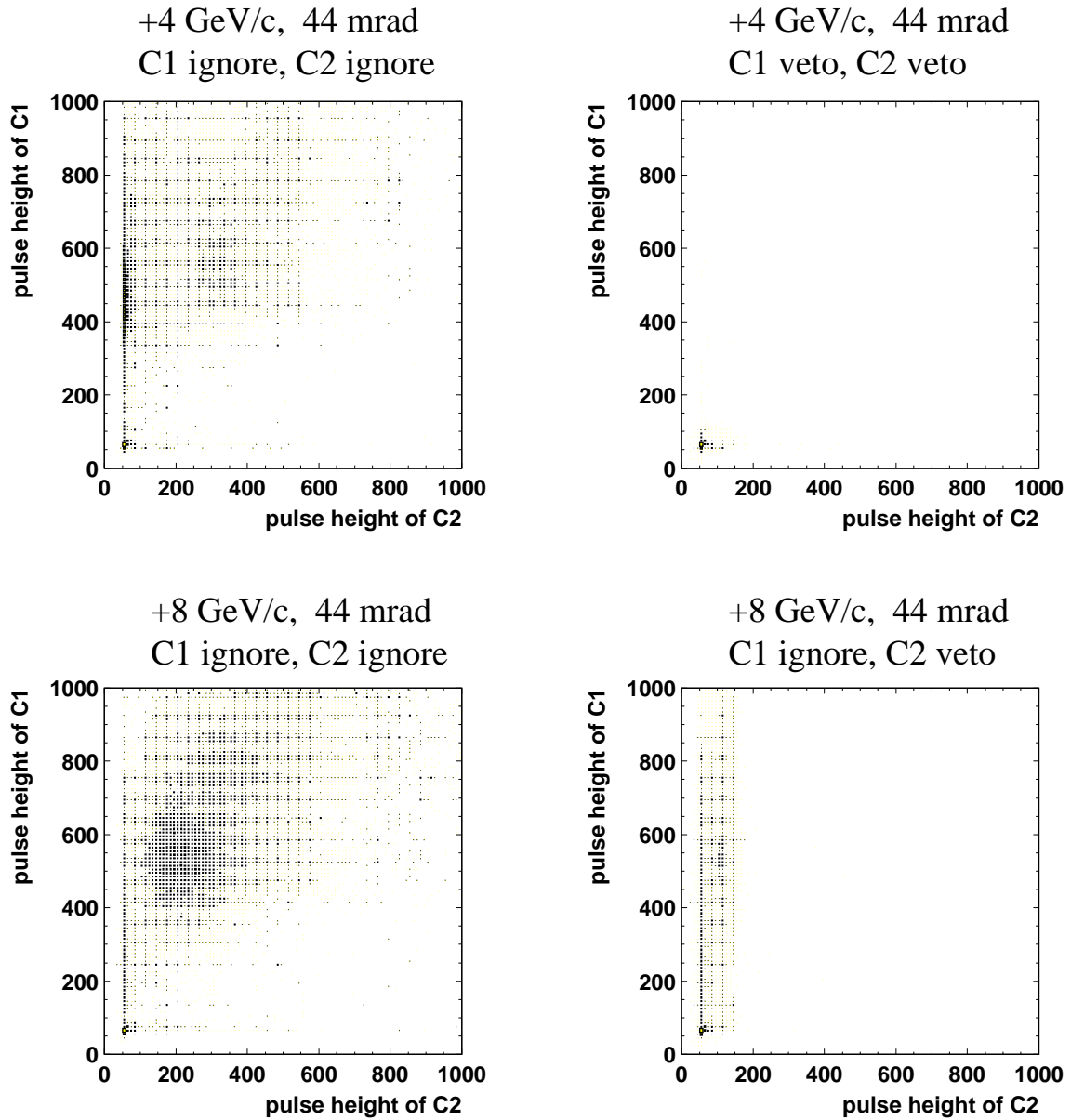
Figure 3.7: Examples of scatter plots of e/π/K/p runs (left) and K/p runs (right). The discriminator threshold of C1 and C2 counters are set higher positions than the pedestal, therefore we need off-line cuts to select the particle by the cherenkov informations.

Table 3.5: Cuts for particle identification for each setting. Conditions, (1), (2) and (3) correspond to the region showed in Fig. 3.8, respectively. The identification of pions, kaons and protons are made with the condition indicated in the table. The cuts values are shown in Table 3.6.

	(1) C1:req and C2:req	(2) C1:req and C2:veto	(3) C1:veto and C2:veto
4 GeV/c		π	K/p
8 GeV/c	e/π	K	p

Table 3.6: The cut values of C1:req, C2:req, C1:veto and C2:veto for each spectrometer setting.

momentum	angle	C1:req	C2:req	C1:veto	C2:veto
+4 GeV/c	44mrad	C1≥75		C1<66	C2<61
+4 GeV/c	129mrad	C1≥79		C1<69	C2<64
−4 GeV/c	44mrad	C1≥75		C1<66	C2<61
−4 GeV/c	129mrad	C1≥79		C1<69	C2<65
+8 GeV/c	44mrad	C1≥74	C2≥69	C1<65	C2<60
+8 GeV/c	129mrad	C1≥79	C2≥75	C1<69	C2<65
−8 GeV/c	44mrad	C1≥74	C2≥69	C1<65	C2<60
−8 GeV/c	129mrad	C1≥80	C2≥77	C1<69	C2<66

Scatter plots in Fig. 3.7 are example plots of pulse height of C1 and C2 counters for e/π/K/p runs and K/p runs. Since the discriminator thresholds of C1 and C2 in the K/p runs were set higher values than the pedestals, respectively, we need off-line cuts. The event selections using the C1 and C2 counters are shown in Table 3.5, and Fig. 3.8 shows an example of the event selections.

For the particle identification, it is necessary for the counter response to be stable, however, we measured pedestal flickers of the C1 and C2 in each run over all the spectrometer setting. Fig. 3.9 shows trends of flicker for both cherenkov counters. The trends was independent in the same momentum and angle setting, therefore I employed the same cut for particle identifications in the e/π/K/p runs and K/p runs. As regions for 'C1:veto', 'C2:veto', 'C1:req' and 'C2:req', I select the regions indicated by the arrows in the Fig. 3.8 and Fig. 3.9.
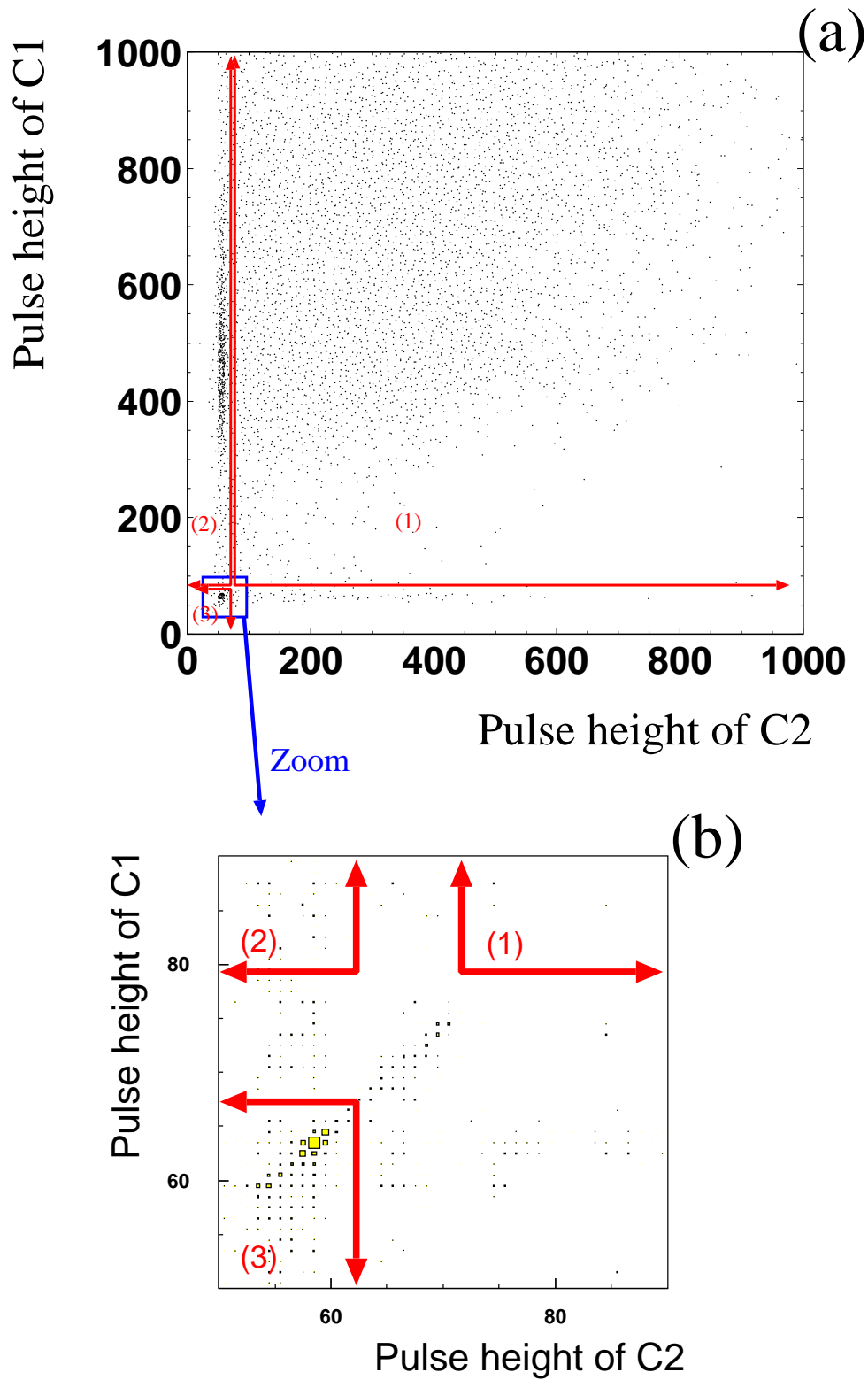
Figure 3.8: The scatter plot of pulse heights of C1 and C2. The three area (1), (2) and (3) indicated by the arrows correspond to the regions shown in Table 3.5. The plot (b) is zoomed a region around pedestal in the plot (a).
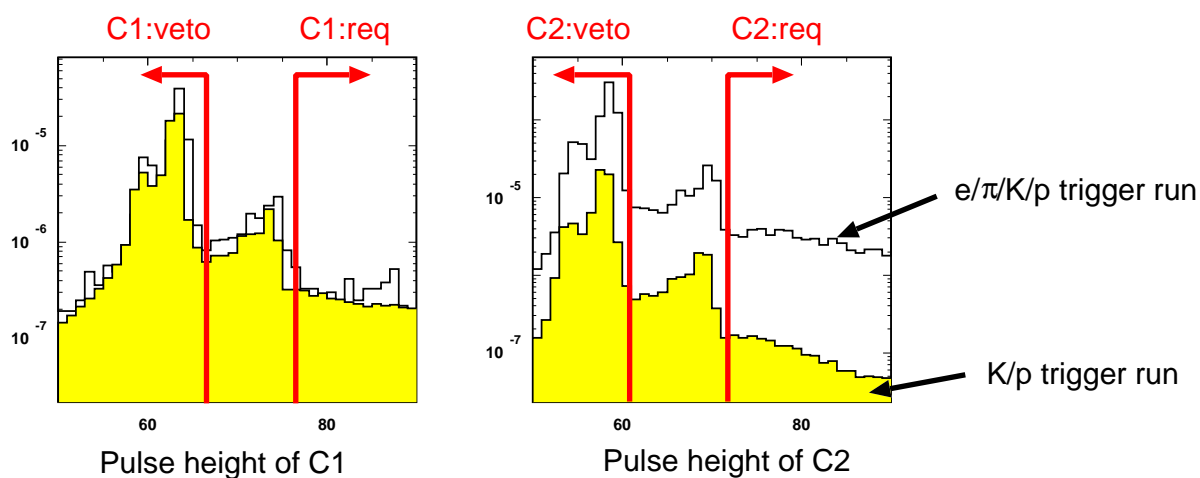
Figure 3.9: Example histograms for the pedestal shift of C1 (left) and C2 (right). The no-hatched histograms are 'C1 ignore and C2 ignore' runs and correspond projecting Fig 3.8 (b) on to both axes. The hatched histograms are 'C1 veto and C2 veto' runs. The discriminator thresholds for 'C1 veto and C2-veto' runs are set at a values out of the histograms. There are two main peaks for the pedestal and small structure of each peak in the both runs. The allows indicate the cuts for 'C1:veto', 'C1:req', 'C2:veto' and 'C2:req'.

3.4.4 Cherenkov veto factor

The cherenkov veto factor was estimated by the ratio of a number of events rejected by C1 and C2 cuts to a number of events selected from the data taken without C1 and C2 trigger. The factor $1 + \alpha_{cv}$ is defined as

$$1 + \alpha_{cv} \equiv 1 + \frac{(\# \text{ of proton in event not selected})}{(\# \text{ of proton in event selected})}$$

where ($\#$ of proton in event selected) means a number of protons selected by the cherenkov veto off-line ('C1:veto' and 'C2:veto'). This definition is base on an assumption as the following items.
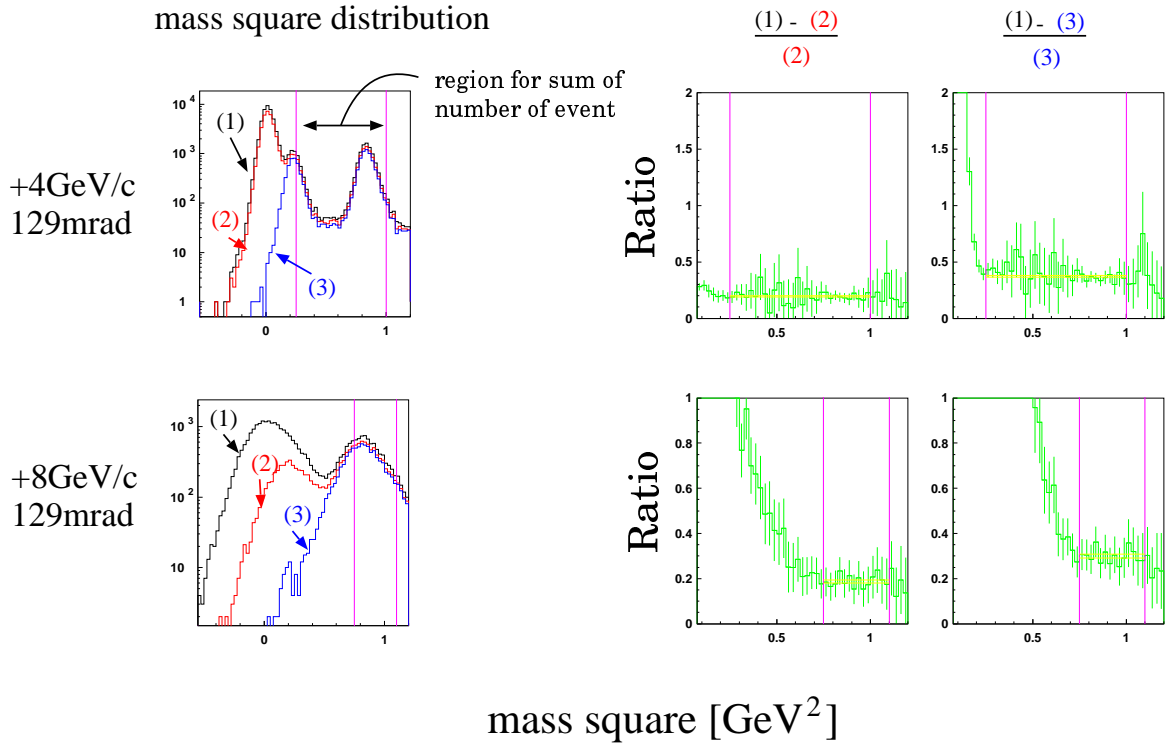
Figure 3.10: Example of figures to estimate cherenkov veto factors. The top figures are from $+4$ GeV/c 129mrad setting and the bottom figures are from $+8$ GeV/c 129mrad setting. The mass square distributions (1), (2) and (3) are corresponding to 'no cut on C1 and C2', 'C1:veto' and 'C1:veto and C2:veto', where the conditions 'C1:veto' and 'C2:veto' are defined in Table 3.6. The ratios in the figures on right hand corresponds to the values of α_{cv} of the cherenkov veto factor '$1 + \alpha_{cv}$'

1. The proton peak in the mass square distribution contains no contaminations from other particles.

2. The shape of mass square distributions is independent on the C1 and C2 cuts.

3. The rejection efficiency of 'veto' is independent of particle species. It means the rejection efficiency of protons from the event sample taken without any C1 or C2 cuts is the same as the pion or kaon rejection efficiency from the same event.

Fig. 3.10 shows the mass square distributions with 'no cut on C1 and C2', 'C1:veto' and 'C1:veto and C2:veto' indicated by (1), (2) and (3), respectively. The top figures are from the +4 GeV/c 129mrad setting and the bottom are from the +8 GeV/c 129mrad setting. The centre and right histograms are the ratio as a function of mass square calculated by an equation as shown by description in the figure. The two histograms of the ratios for the 4GeV setting shows that the ratio around kaon peak and proton peak seems to be a constant as a function of mass square in the error bar. This tendency supports the present method to evaluate correct.

Table 3.7 summarizes the values of α_{cv} of the cherenkov veto factor '$1 + \alpha_{cv}$' for each setting with different centrality.

3.4.5 Correction for requiring single track

To estimate veto factor, the single track in the spectrometer was required to employ C1 and C2 trigger. However, to make a single particle spectrum, I need to add particles in the multiple track event into the particles of the single particle track. The correction factor is basically the yield ratio of the entire events to the single track events, if we neglect particle correlations in the spectrometer acceptance. The factor $1 + \alpha_{track}$ is given by,

$$1 + \alpha_{track} \equiv 1 + \frac{(\# \text{ of } \pi, \text{ K and p with nTrack>2})}{(\# \text{ of } \pi, \text{ K and p with nTrack=1})}$$

where nTrack=1 means the selection of the single track events, and nTrack>1 corresponds the selection of the multiple track events. If there are no particle correlations, the mass square distributions for the single track events and the multiple track events should be the same. It was checked in Fig. 3.11. Here I plot two examples at the 4 GeV/c and 8 GeV/c with a different angle setting. The mass square distributions are quite similar in

any regions for pion, kaon and proton. The differences normalized with the entire yield in the right figures show constant ratio over the particle region. Therefore, I am able to correct the absolute cross section for all particle species with the factor summarized in Table 3.8.
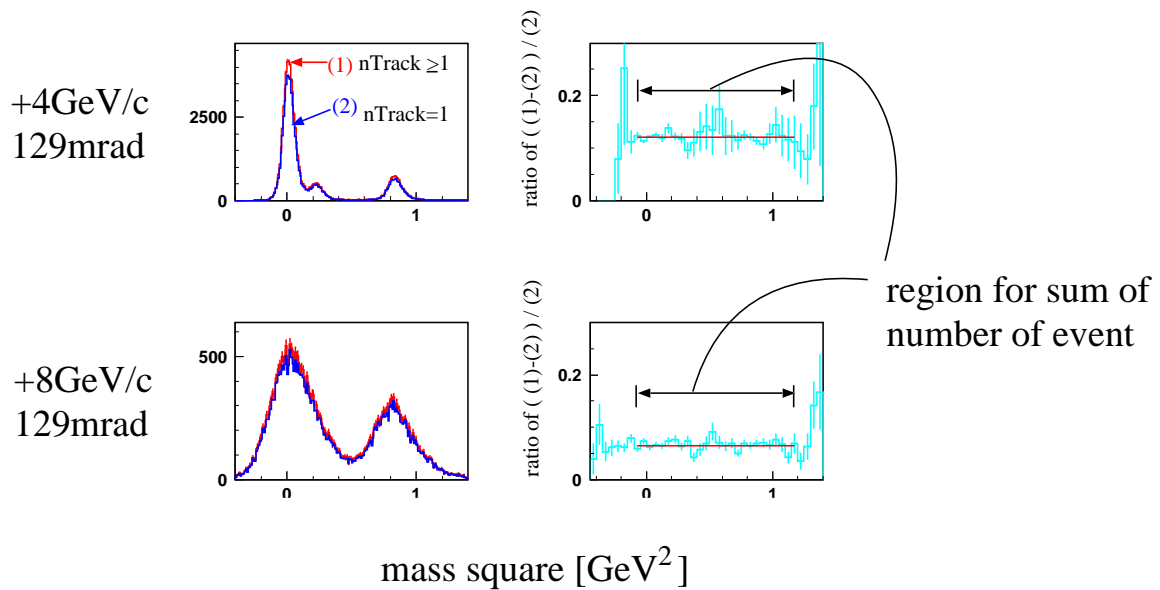
Figure 3.11: Example of histograms to calculate correction factor for requirement of single track event (nTrack=1). The left histograms are mass square distributions from all tracks (1) and from event required nTrack=1 (2). The right-hand side histograms are the ratios of ((1)-(2))/(2) as a function of mass square. The sum of number of tracks are done in a region indicated by the arrows.

Table 3.7: Cherenkov veto factor for each setting and centrality. The factor is given by $1 + \alpha_{cv}$. The error is statistical error only.

momentum	angle	centrality	α_{cv}	
			C1:veto (e veto)	C1:veto and C2:veto (e and π veto)
+4 GeV/c	44mrad	3.7%	0.49±0.05	1.49±0.15
		7.4%	0.48±0.04	1.43±0.10
		10.5%	0.48±0.03	1.42±0.09
+4 GeV/c	129mrad	3.7%	0.19±0.01	0.38±0.01
		7.4%	0.20±0.01	0.38±0.01
		10.5%	0.20±0.01	0.37±0.01
-4 GeV/c	44mrad	3.7%	0.57±0.12	2.45±0.52
		7.4%	0.64±0.09	2.18±0.34
		10.5%	0.60±0.07	1.78±0.22
-4 GeV/c	129mrad	3.7%	0.15±0.02	0.38±0.03
		7.4%	0.18±0.01	0.40±0.03
		10.5%	0.17±0.02	0.38±0.02

momentum	angle	centrality	α_{cv}	
			C1:veto (e and π veto)	C1:veto and C2:veto (e, π and K veto)
+8 GeV/c	44mrad	3.7%	1.06±0.10	2.45±0.26
		7.4%	0.91±0.06	2.00±0.15
		10.5%	0.86±0.05	1.92±0.12
+8 GeV/c	129mrad	3.7%	0.20±0.01	0.31±0.01
		7.4%	0.19±0.01	0.31±0.01
		10.5%	0.19±0.01	0.30±0.01
-8 GeV/c	44mrad	3.7%	2.73±0.96	4.86±2.02
		7.4%	2.00±0.49	4.77±1.45
		10.5%	1.42±0.28	3.04±0.67
-8 GeV/c	129mrad	3.7%	0.25±0.04	0.49±0.07
		7.4%	0.28±0.03	0.47±0.05
		10.5%	0.27±0.03	0.46±0.04

Table 3.8: Correction factor of 'nTrack=1' cut for each setting and centrality. The factor is given by $1 + \alpha_{track}$. The error is statistical only.

momentum	angle	centrality	α_{track}
+4 GeV/c	44mrad	3.7%	0.400±0.008
		7.4%	0.368±0.005
		10.5%	0.353±0.004
+4 GeV/c	129mrad	3.7%	0.132±0.003
		7.4%	0.126±0.002
		10.5%	0.120±0.002
-4 GeV/c	44mrad	3.7%	0.379±0.007
		7.4%	0.347±0.004
		10.5%	0.335±0.004
-4 GeV/c	129mrad	3.7%	0.106±0.003
		7.4%	0.094±0.002
		10.5%	0.092±0.002
+8 GeV/c	44mrad	3.7%	0.496±0.009
		7.4%	0.460±0.006
		10.5%	0.447±0.005
+8 GeV/c	129mrad	3.7%	0.078±0.003
		7.4%	0.070±0.002
		10.5%	0.067±0.002
-8 GeV/c	44mrad	3.7%	0.450±0.009
		7.4%	0.432±0.006
		10.5%	0.413±0.005
-8 GeV/c	129mrad	3.7%	0.045±0.003
		7.4%	0.039±0.002
		10.5%	0.039±0.002

3.4.6   Particle identification from Time-Of-Flight as a function of momentum

After the C1 and C2 cuts, the particle identification has been made with mass square values. The H3TOF variable was employed for the TOF plots, because the path length to the hodoscope 3 was much larger than that of H2, and a large path length makes a
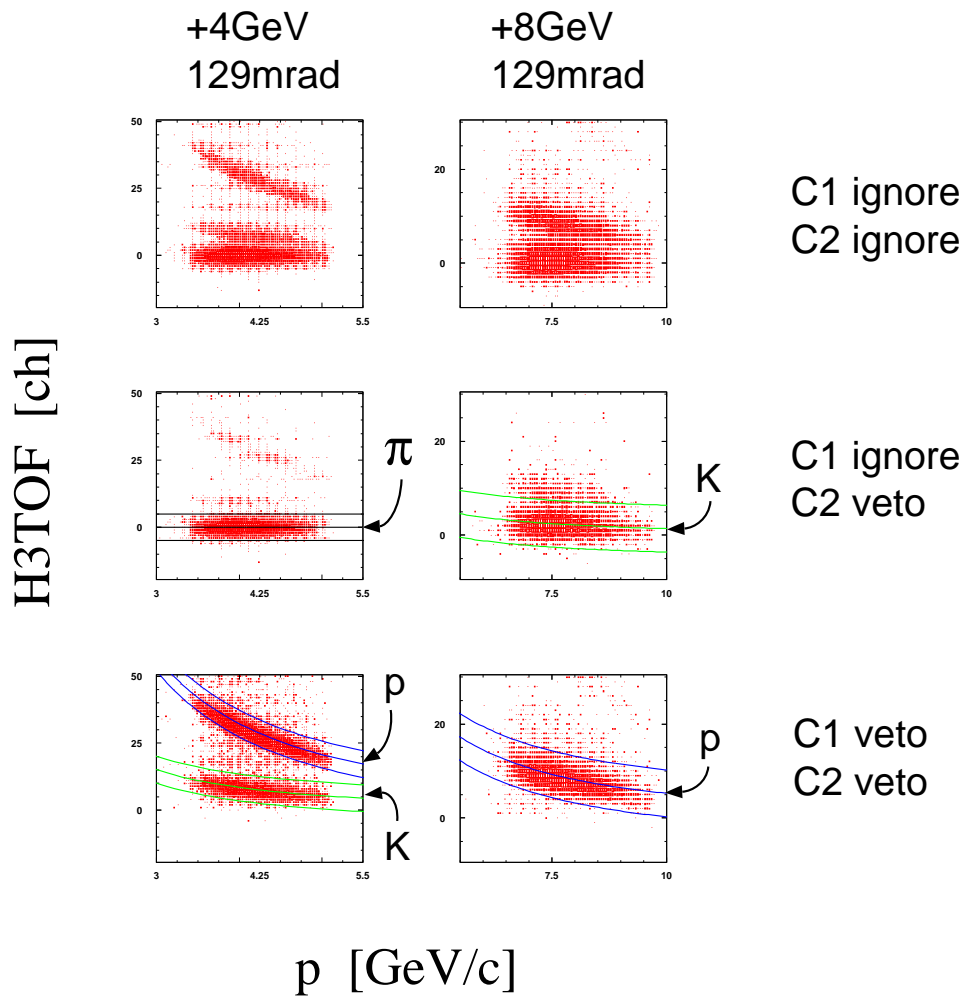
Figure 3.12: Scatter plot of H3TOF and momentum. As example, plots of the +4 GeV/c and +8 GeV/c 129mrad setting are shown. The line on the figure is TOF of particle as a function of momentum. The centre line of three are indicated for the particle and the outer two lines are corresponding to ±4 ch. The particle in the region is selected.

Table 3.9: The p_y cut regions for the low angle setting. The selected regions for the positive and negative settings are independent.

momentum	region selected [GeV/c]
4 GeV/c	$0.00 \leq p_y \leq 0.010$
8 GeV/c	$0.00 \leq p_y \leq 0.022$

clean separation between two particle species travelling at different velocities.

The mass square was calculated with H3TOF values and its momentum in equation (3.3). Since the H3TOF value was absolutely calibrated in the PASS program, and adjusted to be 0 for a particle species with a large yield. To calculate the mass square, the H3TOF value need to add on offset value. The offset value was calibrated with the path length from the target to the hodoscope 3 and its mass as a function of momentum using the below equation.

$$TOF_{particle} = \frac{U_{TDC}}{c} PATH_3 \left(\sqrt{m_{particle}^2 + p^2} - \sqrt{m_{calib}^2 + p^2} \right) /p$$

where $TOF_{particle}$ is in an unit of TDC channel, U_{TDC} is time in the unit of TDC channel (50 ps/ch), c is the light velocity, $m_{particle}$ is the mass (GeV) of particle, m_{calib} is mass (GeV) of particle used for the TOF calibration, $PATH_3$ is path length from the target to the hodoscope 3 and p (GeV/c) is momentum of the particle. To select a particle, a region $TOF_{particle} \pm 4$ ch was required. Since 1 ch is equal to 50 ps and the total resolution of H3TOF is about 80 ps, the cut region corresponds to 2.5 sigma of a gaussian distribution.

Fig. 3.12 shows scatter plots of H3TOF as a function of momentum for the +4 GeV/c and +8 GeV/c 129 mrad settings.

3.4.7   Rejection of tracks scattered by material in Jaws

Fig. 3.13 shows p_y distributions in the +4 and +8 GeV/c 44 mrad settings. To reduce the acceptance, Jaws was 'in' for the low angle setting. The tail in the p_y distributions might be rescattering particles in the material of Jaws. The selected region by the p_y cut was shown in Table 3.9. This cut was done for both experimental data and Monte-Carlo data for an acceptance correction.
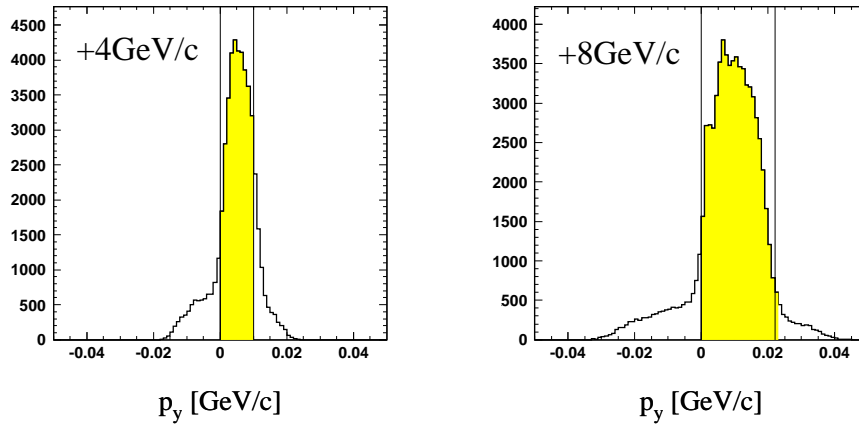
Figure 3.13: p_y distributions from the $+4$ GeV/c and $+8$ GeV/c in 44 mrad setting. The hatched regions indicate events selected.
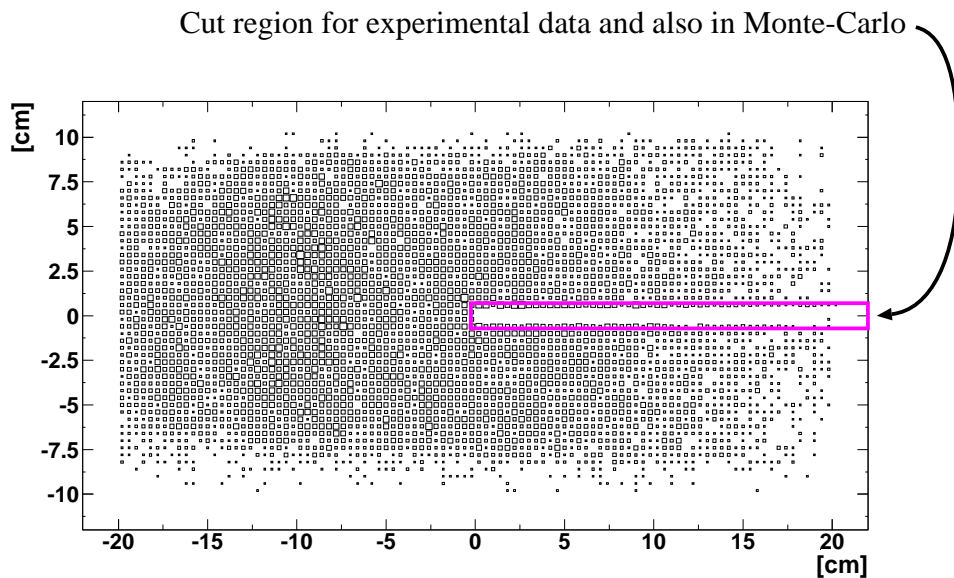
Figure 3.14: The track distribution on SC1. The plot corresponds to a view from downstream position. The region in box is cut for both experimental data and Monte-Carlo data for an acceptance correction.

3.4.8   Correction of dead channels of SC1

A part of the SC1H had dead strips during the Pb 95 run. Fig. 3.14 shows a track distribution on SC1. Since the tracks passing through the dead strip could not be reconstructed with the present tracking algorithm, the region in the SC1

$$-0.8 \text{ cm} < \text{SC1Y} \leq 0.7 \text{ cm}$$

was removed from the spectrometer acceptance, and it was recovered with the acceptance correction using a Monte-Carlo simulation.

3.4.9   H2 efficiency

The H2 had some noisy PMT's and the threshold voltage of these PMT's had to set at higher values than a nominal value to remove 'fake' hit. Some 'real' hits might be lost and it causes inefficiency. The efficiency was studied by John P. Sullivan [49] removing the H2 from the reconstruction algorithm. He concluded the H2 efficiency is 0.898±0.003, and I employed the inverse value 1.11 as the correction factor of the inefficiency.

3.4.10   Hadronic interactions in the target and detectors

The effect of secondary hadronic interactions of produced protons and antiprotons in the spectrometer was studied in Ref. [50]. The correction factors were evaluated with the GEANT [48] simulation. We fond that the hard scatterings or annihilations do not distort the shape of the transverse distribution measured in the spectrometer acceptance, but we lose some amount of flux due to the scatterings. The correction factors to recover the lost fluxes were obtained to be 1.11 for protons and 1.17 for antiprotons, respectively.

3.4.11   PC and K/p trigger efficiency

The PC trigger efficiency was studied by comparing numbers of tracks with the PC trigger and without the trigger. The K/p run which employed the C1 veto and C2 veto in case of the 4 GeV/c setting and C1 ignore and C2 veto in case of the 8 GeV/c setting, was to be studied. However, unfortunately the data-set of the K/p runs with and without PC trigger was not taken in this beam time. Therefore, I have studied product of the PC trigger and the K/p trigger using the cherenkov counters using the pair of data below taken every single run.

Table 3.10: PC trigger and K/p trigger efficiency. The error of the correction factor is statistical only.

momentum	angle	C1 veto and C2 veto by off-line cut		
		no TOF cut	with TOF cut as kaon	with TOF cut as proton
+4 GeV/c	44mrad	1.453±0.039	1.482±0.062	1.428±0.082
+4 GeV/c	129mrad	1.230±0.013	1.240±0.023	1.221±0.018
-4 GeV/c	44mrad	1.582±0.074	1.590±0.091	1.607±0.306
-4 GeV/c	129mrad	1.294±0.027	1.315±0.031	1.243±0.081
momentum	angle	C2 veto by off-line cut		
		no TOF cut	with TOF cut as kaon	with TOF cut as proton
+8 GeV/c	44mrad	1.336±0.021	1.335±0.028	1.368±0.042
+8 GeV/c	129mrad	1.219±0.011	1.237±0.019	1.278±0.014
-8 GeV/c	44mrad	1.256±0.039	1.243±0.042	1.430±0.176
-8 GeV/c	129mrad	1.192±0.020	1.185±0.023	1.259±0.050

$$\text{e}/\pi/\text{K}/\text{p run}: \quad \text{VB} \otimes \text{T0} \otimes \text{Mul1}$$
$$\text{and}$$
$$\text{K}/\text{p run}: \quad \text{VB} \otimes \text{T0} \otimes \text{Mul1} \otimes \text{PID}(\text{K}/\text{p by C1 and C2}) \otimes \text{PC}$$

The mass square distributions from the both data are shown in Fig. 3.15. If both the PC trigger efficiency and the K/p trigger efficiency are unities, the yield in the PID spectrum normalized with the number of beam particle should be the same. However, we saw a lower yield in the data taken with hardware triggers. I concluded this reduction was caused by the inefficiencies the triggers.

The correction factor α_{PCKp} is defined by

$$\alpha_{PCKp} \equiv \frac{(\text{\# of K and p from e}/\pi/\text{K}/\text{p run})}{(\text{\# of K and p from K}/\text{p run})}$$

where (# of K and p from e/π/K/p run) means a number of kaon and proton selected by online C1 and C2 cuts in the e/π/K/p run and (# of K and p from e/π/K/p run) means a number of kaon and proton selected by C1 and C2 cut in the K/p run. The both numbers were normalized by a sum of SCBCL. The correction factors are given in Table 3.10.

without TOF cut   **with TOF cut as kaon**   **with TOF cut as proton**
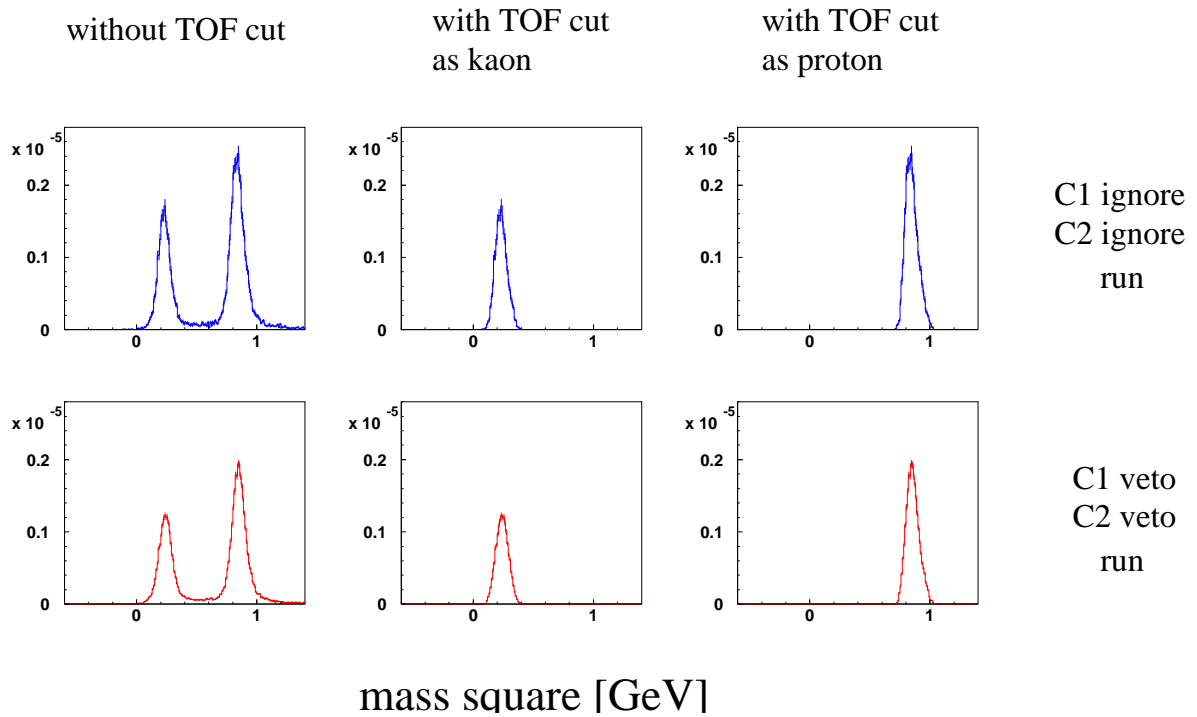
mass square [GeV]

Figure 3.15: Mass square distributions from the e/π/K/p run and the K/p run from the +4 GeV/c 129mrad setting. The events are selected by off-line cuts, C1:veto and C2:veto (see Table 3.5 and 3.6) for all histograms. The centre and right histograms are kaon and proton distributions selected by the TOF cut additionally. The PC trigger and K/p trigger efficiency are estimated by getting the ratio of number of events in the top histograms to one in the bottom histograms.

Table 3.11: The ratio of sum of SCBCL to corrected beam.

	+4 GeV/c		-4 GeV/c	
	44mrad	129mrad	44mrad	129mrad
e/π/K/p run	1.063	1.087	1.074	1.083
K/p run	1.005	0.987	1.073	1.063

|	+8 GeV/c		-8 GeV/c	
	44mrad	129mrad	44mrad	129mrad
e/π/K/p run	1.005	0.987	1.073	1.063
K/p run	0.947	0.982	0.995	1.048

3.5 Beam normalization

The beam normalization is the most important issue to measure the absolute cross section. Various numbers in the trigger system were counted every spill and recorded ion a tape at end of burst. The variables useful to the normalization are the following.

SCBCL	Live-gated Beam counts.
SCCXTRIG	Total number of CX triggers.
SCTRIG	TRIG OR output. Total triggers, not vetoed by Before/After protection.
SCTHAND	THE AND output.

where 'TRIG OR' and 'THE AND' are indicated in Fig. 2.5.

There are two scenarios for the beam normalization. The simplest is to sum over the SCBCL. The other is a sum of SCCXTRIG×SCTHAND/SCTRIG, which is called corrected beam. These two methods use independent variables, so we can check the validity the beam normalization by comparing these two results. 5 % difference was reported for the 1994 runs [51].

I checked whether there is difference between two approaches for the Pb'95 data. Fig. 3.16 shows the ratio of sum of SCBCL to the corrected beam as a function of run numbers in different momentum and angle settings. The numbers in the figures are the average of the ratios over all runs for the setting. The difference between two methods is less than 9% for the Pb'95 run and the average has an error of 5%. I treated the difference of the normalization factor into a systematic error for further analysis.
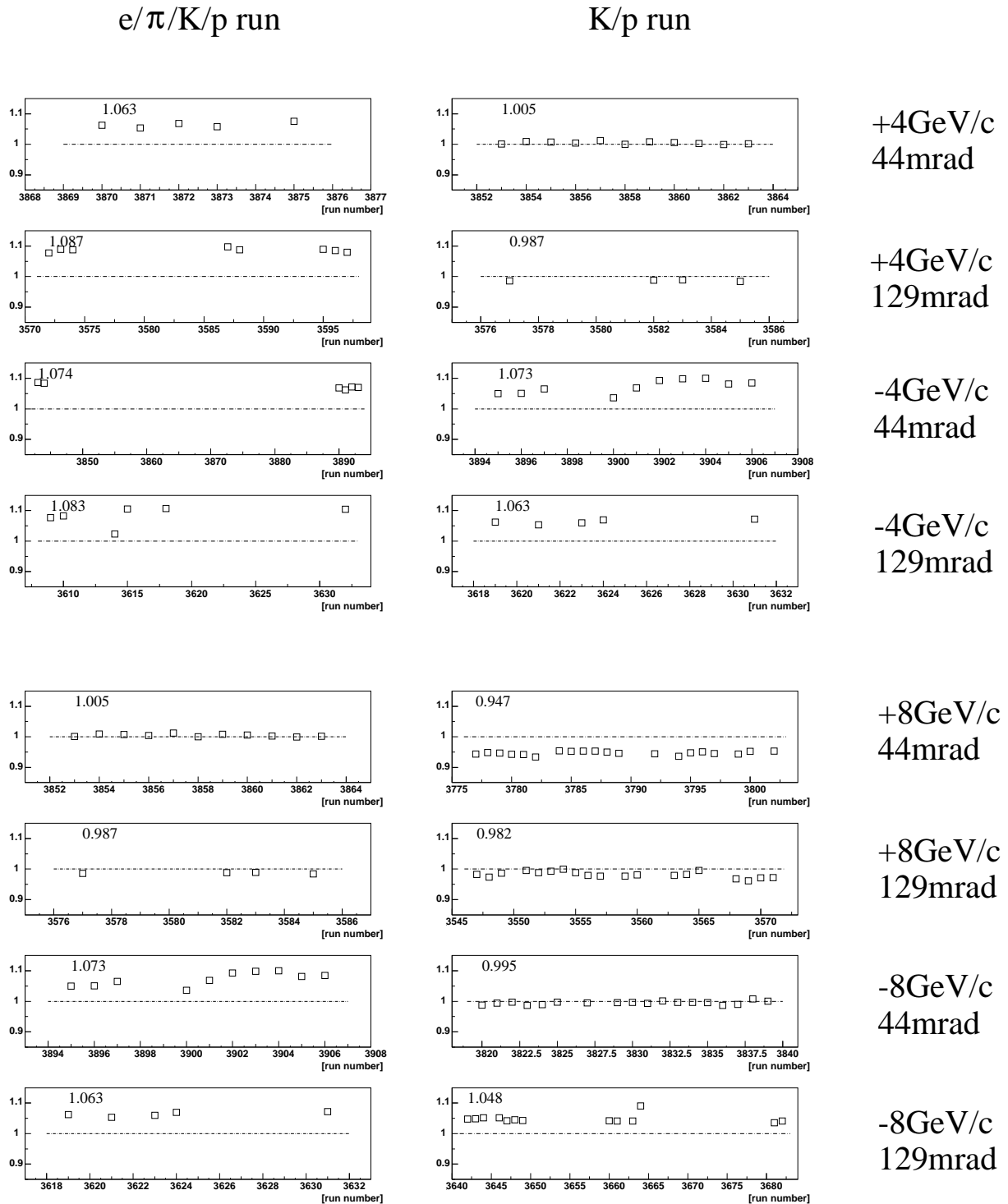
Figure 3.16: Ratio of sum of SCBCL to corrected beam as a function of run numbers. The number on top-left in each plot is the average of the ratio in the setting.

3.6 Acceptance correction

The acceptance correction factor was given by a Monte-Carlo simulation study (mc11) based on TURTLE [52].

The RQMD code was used to find about parameters that represent the momentum spectrum and the rapidity distribution for each particle species. The single particle spectrum at a given rapidity, for example, was expressed by an exponential function, $\exp(-m_T/A)$ for $\frac{1}{m_T}\frac{dN}{dm_T}$, and the parameter A was given by the RQMD model calculation. Monte-Carlo events, which reproduce the single particle spectra, were generated in the mc11 program, traced through the spectrometer and produced hits on the detectors. The Monte-Carlo data was analyzed with the tracking programs in the exactly same method applied to the physics events. I obtained the single particle spectra measured with the spectrum and it original spectra for each particle spices. The acceptance corrections were given by the ratio of the generated yield to the reconstructed yield as a function of m_T.

$$ACF(m_T) = \frac{\left.\frac{1}{m_T}\frac{dN}{m_T}\right|_{\text{generated}}}{\left.\frac{dN}{m_T}\right|_{\text{reconstructed}}}$$

The single particle spectrum was finally obtained by correcting the spectrum measured for the acceptance correction factor $ACF(m_T)$ as a function of m_T.

$$ACF(m_T) \times \left.\frac{dN}{m_T}\right|_{\text{measured}} \equiv \left.\frac{1}{m_T}\frac{dN}{m_T}\right|_{\text{corrected}}$$

3.7 Effect of Λ and Σ decays into protons and antiprotons

The spectrometer detects charged particles behind a series of magnets and has no vertex detectors in the target region. Therefore, some short-lived particles like Λ, Σ, Ξ and their anti-particles will be detected and a part of daughter particles will be identified in the spectrometer. They are contamination to the charged particle spectra. Since yields of pions are so large, effects to the spectra are negligible small. However, the contamination to proton or antiprotons is serious due to their small production rates.

Table 3.12: The dN/dy in mid-rapidity from RQMD(v2.3) in central collisions (b<3 fm)

	dN/dy		dN/dy
π^+	190	π^-	195
p	35	$\bar{p}$	2.5
Λ	14	$\bar{\Lambda}$	1.5
Σ^+	5	$\bar{\Sigma}^-$	0.6
Σ^0	5	$\bar{\Sigma}^0$	0.6
Σ^-	5	$\bar{\Sigma}^+$	0.6
Ξ^0	1.5	$\bar{\Xi}^0$	0.6
Ξ^-	1.5	$\bar{\Xi}^+$	0.6

The decay modes of strangeness baryons are

$$\Lambda \xrightarrow{64\%} p + \pi^- \qquad \Sigma^+ \xrightarrow{52\%} p + \pi^0 \qquad \Xi^0 \longrightarrow \Lambda + \pi^0$$
$$\xrightarrow{36\%} n + \pi^0 \qquad \xrightarrow{48\%} n + \pi^+$$
$$\Xi^- \longrightarrow \Lambda + \pi^-$$
$$\Sigma^0 \longrightarrow \Lambda + \gamma$$
$$\Sigma^- \longrightarrow n + \pi^-$$
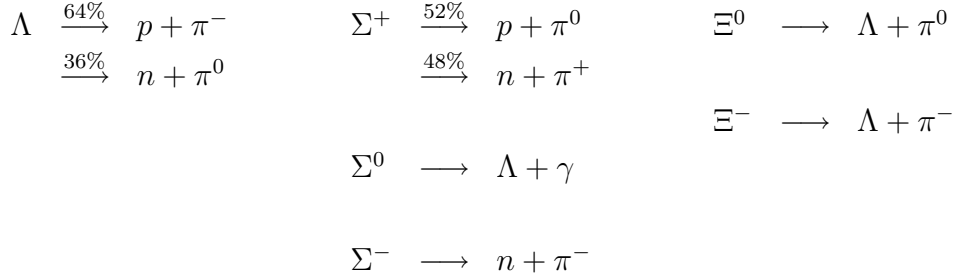
Those particles decay to pions, nucleons and gammas. The dN/dy for various particles near mid-rapidity in the central collisions are evaluated with RQMD(v2.3), and their yield are given in Table 3.12.

The Monte-Carlo simulation program mc11 was used to estimate the yields from these particles. In this analysis, the effect from Λ, Σ^+ and Σ^0 were taken into account, but neglected contribution from Ξ^0 or Ξ^- into the proton spectrum due to technical problems to those successive decaying particles in the present frame work of mc11. Since the life time of Σ is quite short, its yield was included into the Λ yield.

The correction factor is given as a function of m_T,

$$C_p(m_T) = \frac{N_{p_{orig}}(m_T)}{N_{p_{orig}}(m_T) + N_{p_\Lambda}(m_T) + N_{p_\Sigma}(m_T)}$$

where $N_{p_{orig}}$ is the number of original protons, N_{p_Λ} and N_{p_Σ} are the number of protons from Λ decays and Σ^+ decays, respectively.
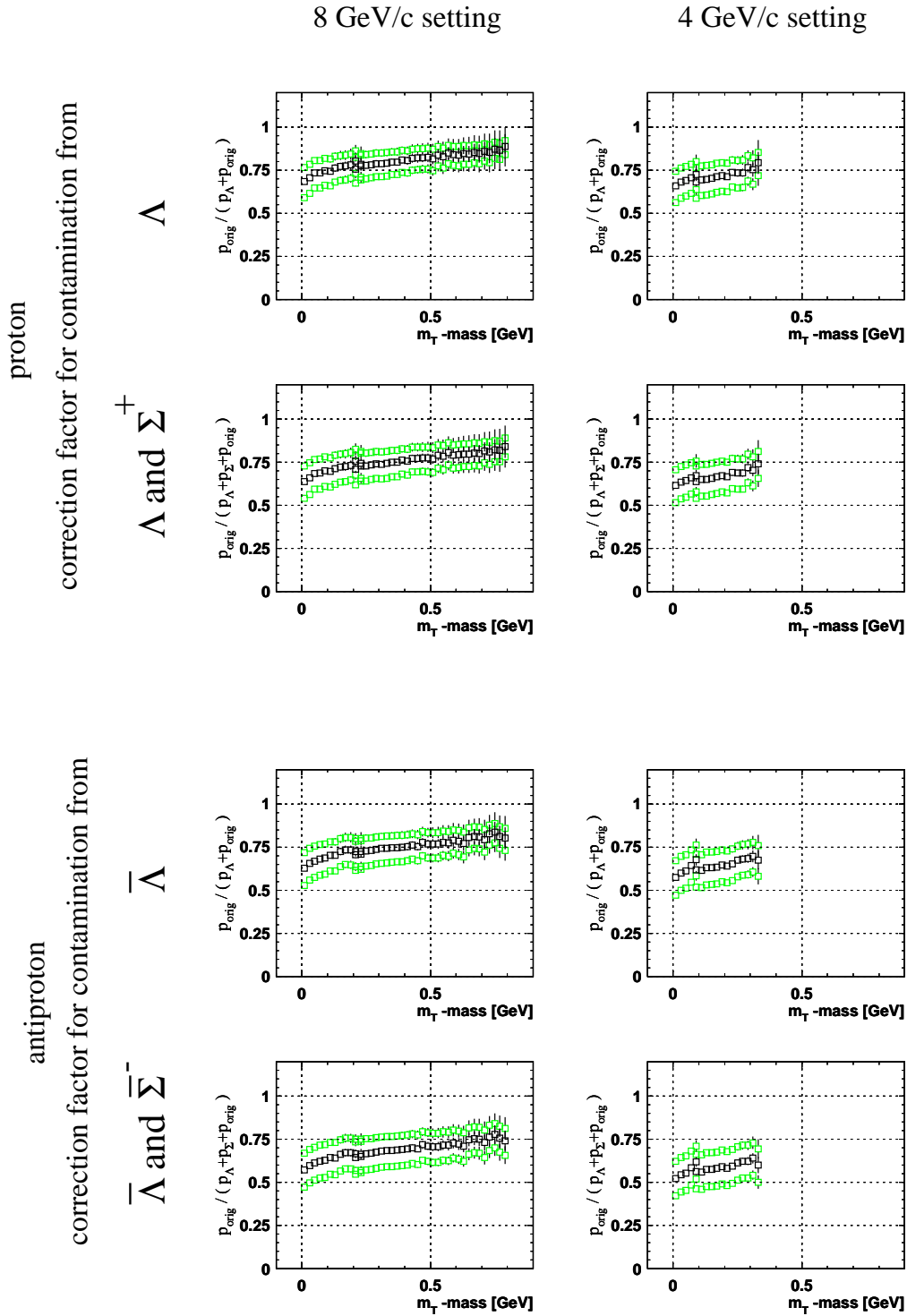
Figure 3.17: The correction factors as a function of m_T. The detail explanation of the figures is written in the text.

Fig. 3.17 shows the correction factors as a function of m_T. Since the correction factors depend on the yield ratio of Λ or Σ^+, the figures shows the factor in three differences. The middle one assumed the Λ/p and Σ/p ratios as given by the RQMD model in Table 3.12, the higher (lower) one assumed the yield ratios are larger (smaller) than the given ones by a factor 1.5. The difference of correction factors by changing the Λ/p and Σ/p ratios are less than 10 %. The proton contamination from Λ and Σ decays weakens with m_T.

3.8 Transverse mass distributions and rapidity densities

The event numbers of pion, kaon and proton data samples after particle identification and quality cuts are shown in Table 3.13.

The particle yields will be given as a function of m_T in the central regions. The dN/dy in the rapidity range will be calculated from the sum of the value of each m_T bin in the measurement region and the fitted coefficient by integration of the single exponential distribution beyond the measurement region.

We took data at the two angles, 44 mrad and 129 mrad. The both data was tried to combine after the absolute normalization, however, the m_T distribution of the low angle data was not matched to the distribution of the high angle data at their overlapped region. The discrepancy between the data at two angles varies factor 0.5 to 1.5, depending at the setting.

The high angle data have smaller systematic errors from correction factors than those of the low angle data. The low angle data have an uncertainties originated from the Jaws. The data shows different p_y distributions for different particle species. This phenomenon could not be understood without scattering effect in the Jaws. However, the effects of Jaws could not be understood very well with our Monte-Carlo studies. For example, the tail of p_y distributions toward the peak can not reproduced in the mc11. Therefore, in this analysis, I decided to take the high angle data for the absolute normalization. The low angle data was adjusted to make a smooth m_T distribution from the low momentum edge of the high angle data to the point at $m_T = 0$.

The matching procedure of the low angle data to the high angle data was carried by fitting of the both distributions with an exponential function with the same inverse slope

Table 3.13: Number of events for each spectrometer setting.

		44 mrad setting			129 mrad setting		
		centrality σ [%]			centrality σ [%]		
		3.7	7.4	10.5	3.7	7.4	10.5
4 GeV/c setting	π^+	2713	5350	7527	11498	22070	30511
	π^-	3839	7511	10470	11163	21129	28911
	K$^+$	5150	10818	15679	4238	8206	11240
	K$^-$	5814	11435	16281	12222	23550	32342
	p	3644	7404	10744	6577	12729	17593
	$\bar{\text{p}}$	428	874	1235	1663	3228	4513
8 GeV/c setting	K$^+$	14689	29462	41767	22614	41397	55561
	K$^-$	12563	25320	35783	26578	50030	67631
	p	6215	12788	18633	41682	76676	102966
	$\bar{\text{p}}$	711	1470	2137	5834	11347	15306

parameter. The constant for the low angle data is a free parameter. The function is

$$f(m_T) = \begin{cases} A_1 \exp(m_T/B) & \text{for data from 44 mrad setting} \\ A_2 \exp(m_T/B) & \text{for data from 129 mrad setting} \end{cases} \tag{3.5}$$

where A_1 and A_2 are constants and B is the inverse slope parameter.

Fig. 3.18 and 3.19 show the invariant cross sections as a function of $m_T - m$ for pions, kaons, proton and antiproton in the three different centralities. The inverse slope parameters and dN/dy for each particle and the spectrometer setting are given in Table 3.14.

The invariant cross sections of protons and antiprotons corrected for the effect of Λ and Σ decays are shown in Fig. 3.20 and 3.21. The error bars in the figures show the systematic errors from the Λ and Σ decay corrections.

3.8.1   Systematic errors

The inverse slope parameters are given by fitting the experimental distribution with a single exponential function. The fitting error of the slope has an error from the matching. The systematic errors for the inverse slope parameters were estimated by changing the fitting region by $\pm$ 80 MeV and are shown in Table 3.15. The systematic errors from the

inverse slope propagate to the error of dN/dy, and the errors are given in the table. The errors from the fitting are less than 9% for the inverse slope and less than 6% for dN/dy.

The errors by the correction factors are shown in Table 3.16. Those errors do not affect the m_T distribution but dN/dy. The contribution to dN/dy from the correction factors is about 8% in total.

The contamination to protons and antiprotons from Λ and Σ decay were corrected and the systematic errors by the corrections are listed in Table 3.17. The errors are about 7% of the inverse slope for the 4 GeV/c setting, about 3% for the 8 GeV/c setting, about 15% for dN/dy of protons and about 19% for dN/dy of antiprotons.

Assuming the errors have no correlation each other, the total systematic error was given by adding the errors in quadrature. The inverse slope parameters and dN/dy for the all of particles and the spectrometer setting are summarized in Table 3.18.

3.9 Summary of data analysis

I obtained the invariant cross sections of the charged pions and kaons, proton and antiproton from the data taken in 1995. The inverse slope parameters are obtained to be the same values within the errors as the results of Ref. [27], which the NA44 collaboration has reported these values and m_T distributions from the data taken in 1994. The most important development in this thesis is that I finally obtained the invariant cross sections from the NA44 data. The absolute values of the rapidity densities allow the study of the dynamics of freeze-out conditions from view points of the thermal and the chemical freeze-out.

I showed various data for different centralities. The slope parameters have no sensitivity to the centrality in the top 10% region. The dN/dy is increasing with the centrality. Especially, dN/dy of the pions and the proton show stronger dependence than the other particles.

In the next chapter, I will discuss the freeze-out scenario from this data and the macroscopic parameters to describe an expanding system.
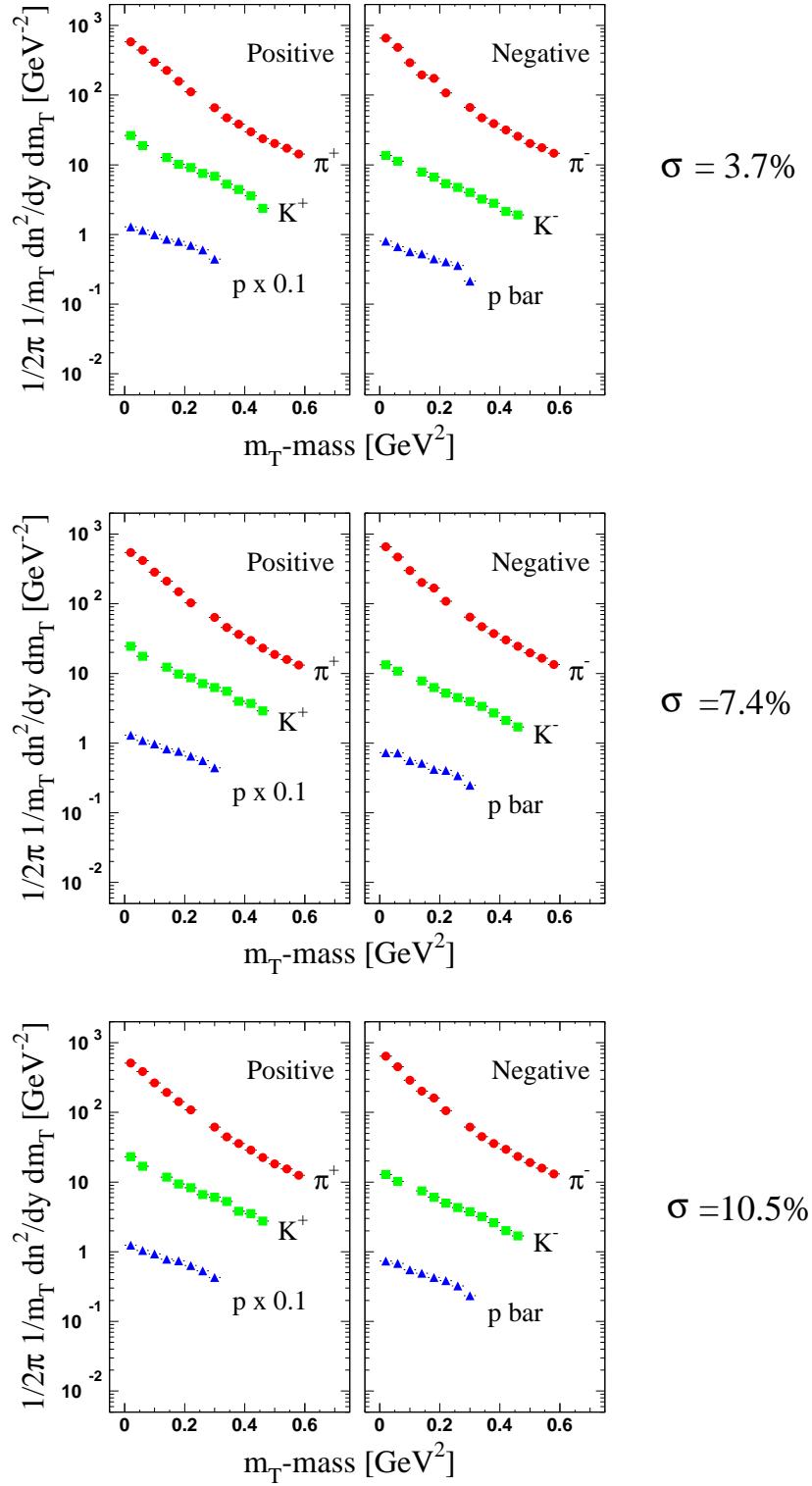
Figure 3.18: The invariant cross sections as a function of $m_T - m$ for pions, kaons, proton and antiproton, and various centralities in the 4 GeV/c setting.
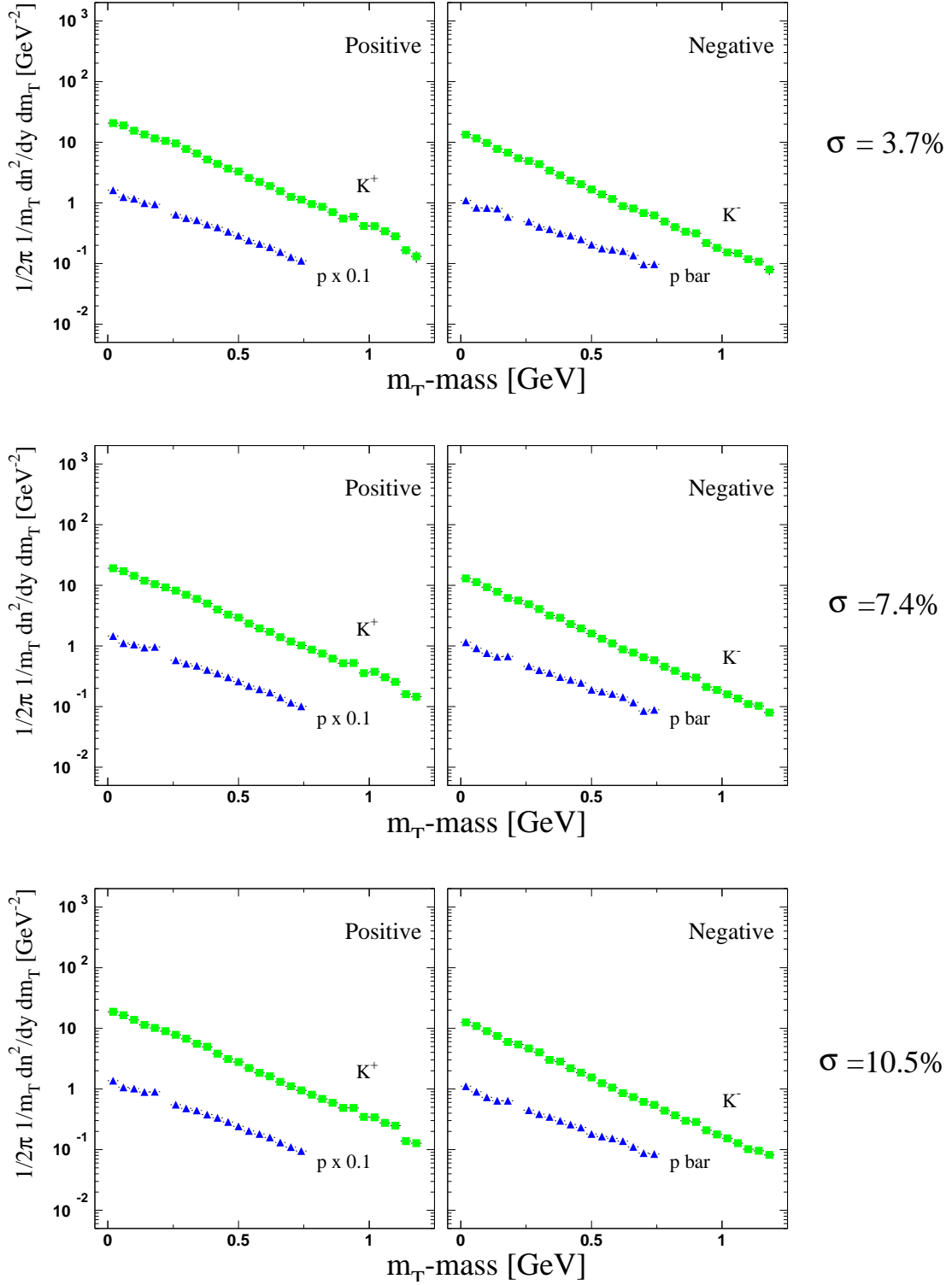
Figure 3.19: The invariant cross sections as a function of $m_T - m$ for kaons, proton and antiproton, and various centralities in the 8 GeV/c setting.

Table 3.14: The fit regions for the inverse slope parameter, the values of inverse slope (MeV) and dN/dy for each particle, centrality and momentum setting. The rapidity region indicates the NA44 acceptance in the low angle setting to the high angle setting except pions. The pion rapidity region on the table shows the region in the low angle setting. The values of dN/dy is given as the average of the rapidity region.

4 GeV/c setting

	fit range in $m_T - m$ [GeV]	$\sigma = 3.7\%$ slope	dN/dy	$\sigma = 7.4\%$ slope	dN/dy	$\sigma = 10.5\%$ slope	dN/dy	y
π^+	0.20-0.60	176±1	155±1	174±1	147±1	173±1	139±1	2.40-3.10
π^-	0.20-0.60	182±1	161±1	178±1	158±1	178±1	152±1	2.40-3.10
K$^+$	0.00-0.48	227±3	24.4±0.2	238±3	23.8±0.2	235±2	22.6±0.2	2.30-2.90
K$^-$	0.00-0.48	224±2	14.8±0.1	225±1	14.4±0.1	225±1	13.8±0.1	2.30-2.90
p	0.00-0.32	304±7	33.3±0.7	283±4	30.4±0.4	285±4	29.5±0.4	1.90-2.35
p̄	0.00-0.32	269±10	1.49±0.05	294±9	1.56±0.04	279±7	1.47±0.03	1.90-2.35

8 GeV/c setting

K$^+$	0.00-1.20	246±2	27.6±0.1	245±1	24.9±0.1	241±1	23.8±0.1	2.40-3.50
K$^-$	0.00-1.20	228±1	15.4±0.0	226±0	14.9±0.0	226±0	14.3±0.0	2.40-3.50
p	0.00-0.76	288±1	35.8±0.1	287±1	32.8±0.1	286±1	30.9±0.0	2.30-2.90
p̄	0.00-0.76	305±3	2.64±0.01	291±2	2.56±0.01	292±2	2.46±0.01	2.30-2.90

Table 3.15: The systematic errors by the changing the fit region for the inverse slope parameter. The errors on the slope and dN/dy are anticorrelated.

		$\sigma = 3.7\%$		$\sigma = 7.4\%$		$\sigma = 10.5\%$	
		slope	dN/dy	slope	dN/dy	slope	dN/dy
4 GeV/c setting	π^+	6.7%	1.2%	5.1%	0.9%	4.8%	1.0%
	π^-	5.2%	1.0%	4.1%	0.8%	4.2%	0.7%
	K^+	6.5%	3.0%	6.3%	2.9%	5.8%	2.6%
	K^-	2.2%	0.9%	3.5%	1.6%	2.8%	1.3%
	p	5.3%	4.5%	2.4%	1.9%	3.4%	2.7%
	$\bar{\text{p}}$	9.2%	7.4%	6.2%	5.1%	7.4%	6.0%
8 GeV/c setting	K^+	1.7%	1.2%	1.2%	0.8%	1.0%	0.7%
	K^-	0.4%	0.0%	0.2%	0.0%	0.3%	0.0%
	p	2.6%	0.7%	2.1%	0.6%	1.8%	0.5%
	$\bar{\text{p}}$	1.9%	0.6%	4.3%	1.1%	4.7%	1.3%

Table 3.16: The systematic errors from the correction factors for each particle and spectrometer setting.

	+4 GeV/c		-4 GeV/c		+8 GeV/c		-8 GeV/c	
	π	K/p	π	K/p	K	p	K	p
Cherenkov veto	0.8%	0.7%	1.7%	2.2%	0.8%	0.8%	3.2%	4.7%
PC and K/p trigger	–	1.1%	–	2.1%	0.9%		1.7%	
Centrality definition	2.3%		2.1%		1.9%		1.6%	
Requirement of single track event	0.3%		0.3%		0.3%		0.3%	
H2 efficiency	0.3%							
Beam normalization	2.2%							
Double beam cut	4.9%							
average in quadrature	5.4%	6.0%	6.0%	6.5%	5.8%	5.8%	6.7%	7.5%
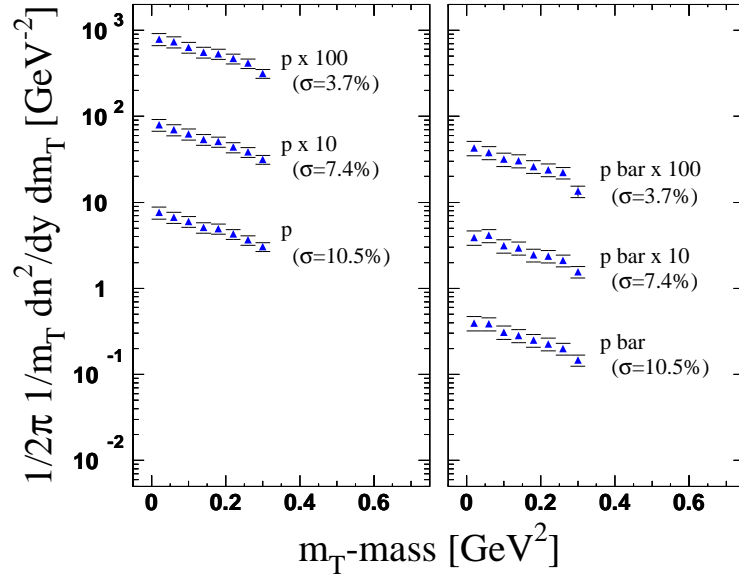
Figure 3.20: m_T distributions of proton and antiprotons in the 4 GeV/c setting with correction of the contamination from the Λ and Σ decays. The error bars correspond to the systematic errors from the Λ and Σ decay corrections.
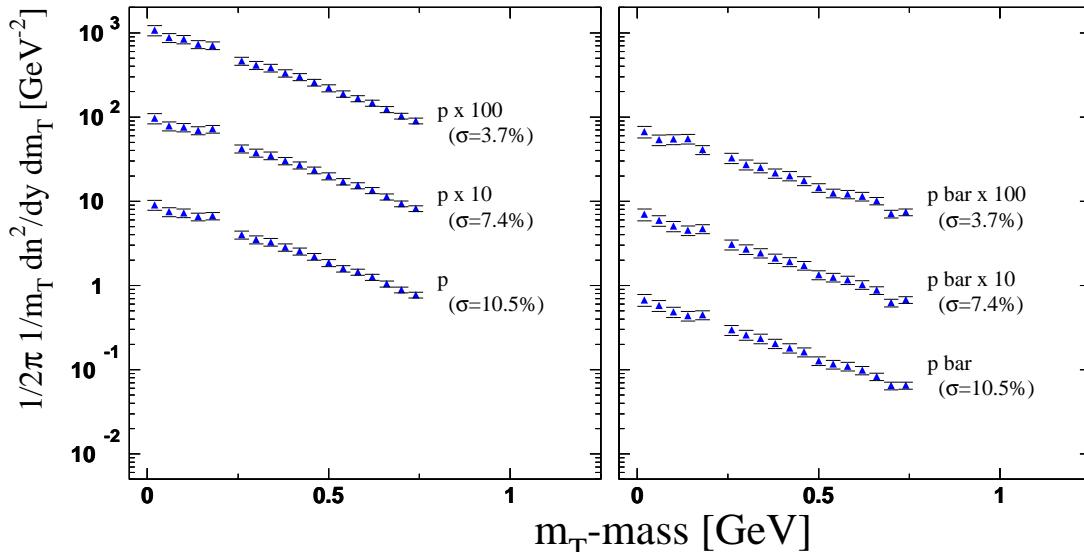
Figure 3.21: In the 8 GeV/c setting, the same figures with Fig.3.20

Table 3.17: The values of inverse slope and dN/dy of the protons and the antiprotons with correction of Λ and Σ decay. The error of inverse slopes is only fitting error. The percentage of the bracket is the error come from increasing and decreasing the ratios of Λ and Σ to p by a factor 1.5 in the estimation.

		Centrality [%]	slope		dN/dy	
4 GeV/c	p	3.7	357±9	(7%)	25.0±0.7	(14%)
		7.4	329±6	(6%)	22.4±0.4	(14%)
		10.5	332±5	(6%)	21.8±0.3	(15%)
	$\bar{\text{p}}$	3.7	358±40	(6%)	1.27±0.16	(18%)
		7.4	374±16	(7%)	1.29±0.06	(19%)
		10.5	352±12	(6%)	1.19±0.04	(19%)
8 GeV/c	p	3.7	315±1	(3%)	27.2±0.1	(14%)
		7.4	313±1	(3%)	24.8±0.1	(14%)
		10.5	310±1	(3%)	23.3±0.0	(14%)
	$\bar{\text{p}}$	3.7	334±3	(3%)	1.85±0.01	(17%)
		7.4	326±2	(3%)	1.78±0.01	(17%)
		10.5	330±1	(3%)	1.71±0.01	(17%)

Table 3.18: The inverse slope parameters and the rapidity densities. The percentage in the brackets is the total systematic error of the value. The values for proton and antiprotons are corrected by the correction factor for the contamination from the Λ and Σ decays.

	y	fit range in $m_T - m$ [GeV]	centrality	slope [MeV]		dN/dy	
π^+	2.40-3.10	0.20-0.60	3.7%	176±1	(7%)	155±1	(6%)
			7.4%	174±1	(5%)	147±1	(5%)
			10.5%	173±1	(5%)	139±1	(5%)
π^-	2.40-3.10	0.20-0.60	3.7%	182±1	(5%)	161±1	(6%)
			7.4%	178±1	(4%)	158±1	(6%)
			10.5%	178±1	(4%)	152±1	(6%)
K^+	2.30-2.90	0.00-0.48	3.7%	227±3	(7%)	24.4±0.2	(7%)
			7.4%	238±3	(6%)	23.8±0.2	(7%)
			10.5%	235±2	(6%)	22.6±0.2	(7%)
	2.40-3.50	0.00-1.20	3.7%	246±2	(2%)	27.6±0.1	(6%)
			7.4%	245±1	(1%)	24.9±0.1	(6%)
			10.5%	241±1	(1%)	23.8±0.1	(6%)
K^-	2.30-2.90	0.00-0.48	3.7%	224±2	(5%)	14.8±0.1	(7%)
			7.4%	225±1	(2%)	14.4±0.1	(7%)
			10.5%	225±1	(3%)	13.8±0.1	(7%)
	2.40-3.50	0.00-1.20	3.7%	228±1	(0%)	15.4±0.0	(7%)
			7.4%	226±0	(0%)	14.9±0.0	(7%)
			10.5%	226±0	(0%)	14.3±0.0	(7%)
p	1.90-2.35	0.00-0.32	3.7%	357±9	(5%)	25.0±0.7	(17%)
			7.4%	329±6	(2%)	22.4±0.4	(15%)
			10.5%	332±5	(3%)	21.8±0.3	(17%)
	2.30-2.90	0.00-0.76	3.7%	315±1	(3%)	27.2±0.1	(19%)
			7.4%	313±1	(2%)	24.8±0.1	(20%)
			10.5%	310±1	(2%)	23.3±0.0	(20%)
$\bar{\text{p}}$	1.90-2.35	0.00-0.32	3.7%	358±40	(9%)	1.27±0.16	(18%)
			7.4%	374±16	(6%)	1.29±0.06	(16%)
			10.5%	352±12	(7%)	1.19±0.04	(17%)
	2.30-2.90	0.00-0.76	3.7%	334±3	(2%)	1.85±0.01	(19%)
			7.4%	326±2	(4%)	1.78±0.01	(19%)
			10.5%	330±1	(5%)	1.71±0.01	(19%)

Chapter 4

THERMAL AND CHEMICAL FREEZE-OUT

The m_T distributions and the values of dN/dy near mid-rapidity is shown in the end of the previous chapter. I will discuss the physics from the m_T distributions and the particle ratios from view points of the thermal and chemical freeze-out.

The general idea of freeze-out is as the following. The produced hadrons interact each other with in-elastic and elastic collisions. After the system expands and an average distance of the hadrons is greater than an interaction length, the hadrons cease to interact. The dynamical informations, for example number of particles, momentum and so on, are frozen at that time. There are two types of freeze-out. One is the thermal freeze-out and the other is the chemical freeze-out.

In the following section, each freeze-out in the central collisions will be discussed by the NA44 data. The compilation of various results from the different collision systems makes the both freeze-out conditions in the heavy ion collisions distinct. It is shown that the hadronization occurs nearby the phase transition of the QGP to hadron gas in the SPS energy region.

4.1 Thermal freeze-out

It is well known that transverse momentum distributions ($\frac{1}{m_T}\frac{dN}{dm_T}$) of hadrons can represented by a single exponential function $A\exp(-m_T/T)$, where A and T are constants, in the heavy ion collisions. Let us consider particle spectra from thermalized hadron gas.

Assuming thermal equilibrium of the hadron gas with a high temperature, the momentum distribution are given by

$$E\frac{d^3N}{dp^3} = \frac{g}{(2\pi)^3}E\exp(-E/T) \qquad (4.1)$$

where g is a number of spi-isospin freedom of the hadron species, E is the energy of the particle and T is the temperature of the system. The left equation is re-writable by transverse mass m_T, rapidity y and azimuthal angle ϕ.

$$E\frac{d^3N}{dp^3} = \frac{1}{m_T}\frac{d^3N}{dm_T\ dy\ d\phi} \qquad (4.2)$$
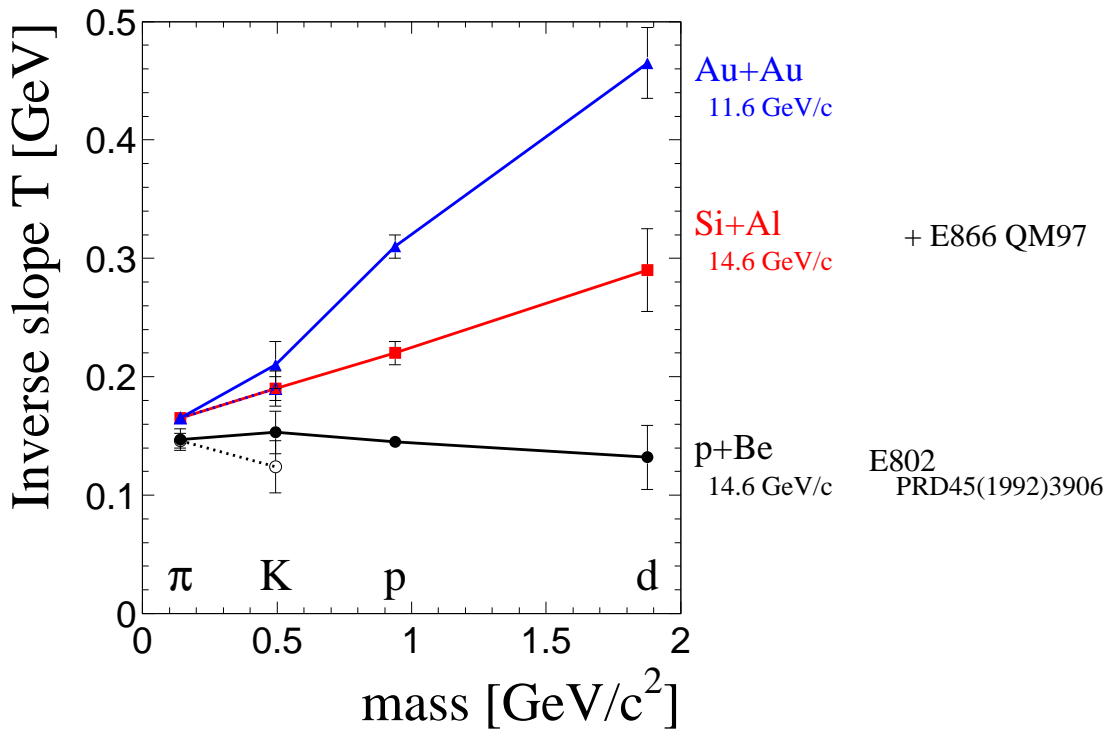
Figure 4.1: The inverse slope parameter around mid-rapidity as a function of mass. The slope parameters are from Ref. [70] for p+Be, Ref. [69] for Si+Al Ref. [53] for Au+Au collisions. For each collisions system, the data points of positive and negative particle are connected by a line, respectively.

For a narrow y region, the transverse mass distribution is described by

$$\frac{1}{m_T}\frac{dN^3}{dm_T \; dy \; d\phi} = A\exp(-m_T/T) \tag{4.3}$$

where A is a constant and T is called as inverse slope parameter and corresponds to the temperature of the Boltzmann gas.

Fig. 4.1 and 4.2 show the various inverse slope parameters as a function of the particle mass in the AGS energy and the SPS energy, respectively. The data near mid-rapidity are used to make the figure. The both figures suggest that heavier particle has larger inverse slope parameter and those parameters show a linear dependence for the mass.

The experimental data of heavy ion collisions at the CERN-SPS and the BNL-AGS show a mass dependence of the inverse slope parameters. The inverse slope parameters
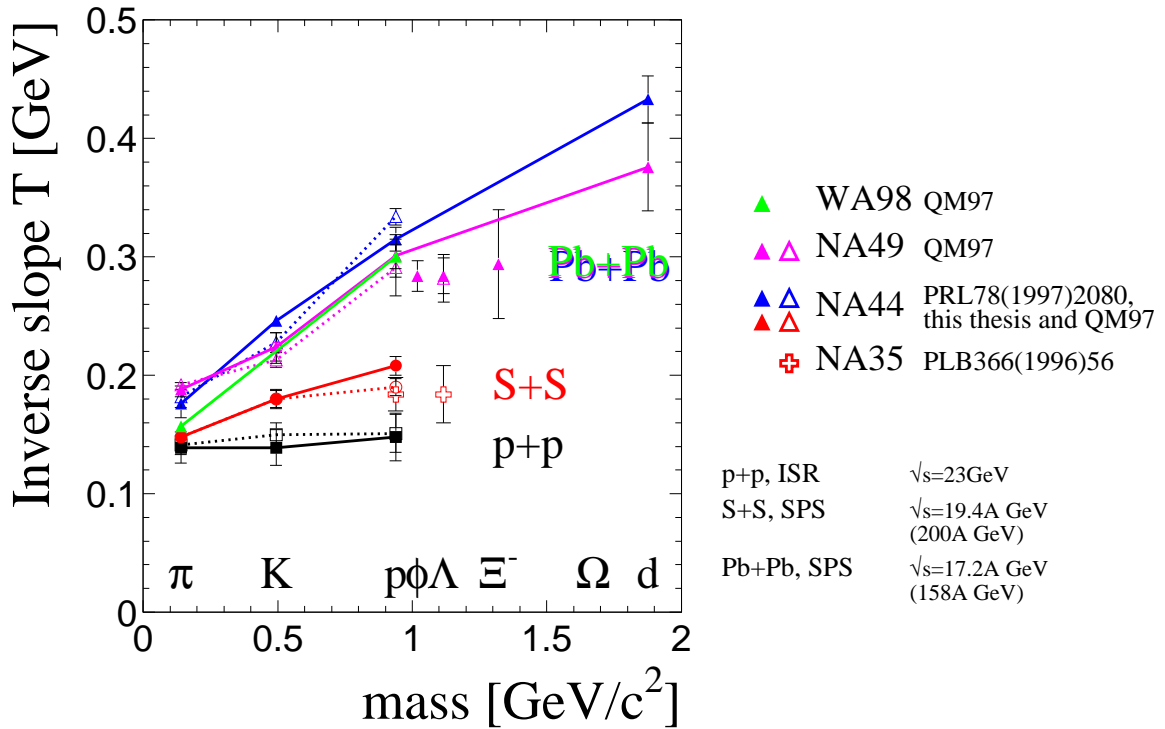
Figure 4.2: The inverse slope parameter around mid-rapidity as a function of mass. The slope parameters are from Refs. [71, 72] for p+p, Refs. [27, 73] for S+S, this thesis and Refs. [56, 57, 59, 63] for Pb+Pb collisions. For each collisions system, the data points of positive and negative particle are connected by a line, respectively.

are increasing with particle mass. It is noted that difference of the slope between the positive and negative charged particle is small for the same mass particles. The recent result of the slope parameters are shown international conference Quark Matter'97 and they are in Refs. [1],[53]-[64].

The mass dependence of inverse slope parameter can be described by an expanding hadron gas by a transverse (or radial) flow in the local thermal equilibrium. T. Cörgo and B. Lørstad discussed correlation of the transverse flow and the inverse slope parameter T in Ref. [65] and show a simple equation

$$\text{T} = T_{th} + m\langle\beta_T\rangle^2 \tag{4.4}$$

where m is the particle mass, $\langle\beta_T\rangle$ is the average of transverse flow velocity, and T_{th} is the temperature for thermal freeze-out. Roughly speaking, the equation (4.4) indicates that the inverse slope parameter has contributions from thermal freeze-out temperature and kinematic energy by transverse flow.

In the both energy regions, the tendency of inverse slope parameters are well described by the equation (4.4). The equation indicate that if the hadrons gas in a thermal equilibrium have a common transverse flow velocity, the inverse slope parameters show a linear dependence of mass and the temperature is given by a limit as mass=0. The data reproduced the above scenario.

I re-calculated T_{th} and $\langle\beta_T\rangle$ for the various collision systems. Table 4.1 shows the values by the fit of inverse slope parameters of pions, kaons, protons and deuteron. The data show the that the thermal freeze-out temperature seems to have small collision system dependence and is about 140 MeV in the SPS and the AGS energy region as shown in Refs. [67, 68]. On the other hand, the transverse flow increases with the collision system.

E. Schnedermann et al. also discussed the transverse flow from slightly different approach in Ref. [66]. Assuming cylindrical fluid with transverse expansion velocity β_r as a function of distance r from longitudinal axis,

$$\frac{dN}{m_T dm_T} \propto \int_0^R r\,dr\,m_T\,K_1\left(\frac{m_T\cosh\rho}{T_{th}}\right)\,I_0\left(\frac{p_T\sinh\rho}{T_{th}}\right) \tag{4.5}$$

$$\rho = \tanh^{-1}\beta_r, \quad \beta_r = \beta_s\frac{r}{R}$$

where T_{th} is thermal freeze-out temperature, β_s is flow velocity at the surface of cylinder, R is maximum radius of the cylinder, K_1 and I_0 is modified Bessel function. The fits of the experimental data by the equation (4.5) are equally good within a temperature range

Table 4.1: Various values of thermal freeze-out temperature (T_{th}) and average of transverse flow velocity ($\langle\beta_T\rangle$) for some collision systems in the AGS and SPS energy regions. Each value is the result of fit for inverse slope parameters of pions, kaons, protons and deuteron by equation (4.4).

	AGS energy region			SPS energy region	
	T_{th} [MeV]	$\langle\beta_T\rangle$ [c]		T_{th} [MeV]	$\langle\beta_T\rangle$ [c]
p+Be	147±6	0.05±0.09	p+p	139±8	0.11±0.13
Si+Al	155±6	0.26±0.11	S+S	140±3	0.26±0.09
Au+Au	139±4	0.42±0.10	Pb+Pb	145±2	0.41±0.07

Table 4.2: Inverse slope parameters (MeV) for pions, kaons, protons and deuteron from various data. These values are used for the calculation for Table 4.1. The mark (*) corresponds to the values from top 3.7% centrality of this thesis.

AGS energy region

	π^+	K^+	p	d	π^-	K^-	$\bar{p}$	Refs.
p+Be	147±9	153±18	145±5	132±27	146±6	124±22		[70]
Si+Al	165±5	190±10	220±10	290±35				[69]
Au+Au	165±5	210±20	310±10	465±30	165±5	190±15		[53]

SPS energy region

	π^+	K^+	p	d	π^-	K^-	$\bar{p}$	Refs.
p+p	139±13	139±15	148±20		141±8	150±10	151±16	[71, 72]
S+S	148±4	180±8	208±8		148±4	180±7	190±7	[27]
Pb+Pb	176±12	246±5	315±10		182±9	228±1	334±7	(*)
				1433±20				[57]
	188±6	224±12	301±18	1376±37	192±3	213±6	291±4	[56]
	157±2		300±10					[59]

$100 \leq T_{th} \leq 150$ MeV in Ref. [27]. Recently the NA49 collaboration obtained the thermal freeze-out temperature $T_{th} \approx 120$ MeV from a simultaneous analysis of transverse mass spectra and two-pion interferometry data [56].

The transverse flow and the thermal freeze-out temperature are obtained by the equation (4.4) and (4.5). The both results give similar values for the temperature and the flow. The thermal freeze-out temperature from the equation (4.5) is rather lower than from the equation (4.4), systematically. Considering the both approach and the data, I concluded that the thermal freeze-out temperature is about 120 to 140 MeV in the SPS energy.

Finally, I comment on very recent data of strange baryons. The WA97 collaboration has reported a very interesting data for the slope parameters. They measured transverse momentum spectra of Λ, Σ and Ω and found that those slope parameters are decreasing with the particle mass. The picture of the thermal freeze-out was that the system had the same thermal freeze-out temperature and the common transverse flow for the hadrons. The WA97 data, however, against the old picture of the thermal freeze-out. Ref. [75] points out that the multi-strange particles have frozen out in the earlier stage than the other particles by analysis of the RQMD model. The systematics of the non multi-strange particle spectra indicates that the main component of the flow develops only rather late.
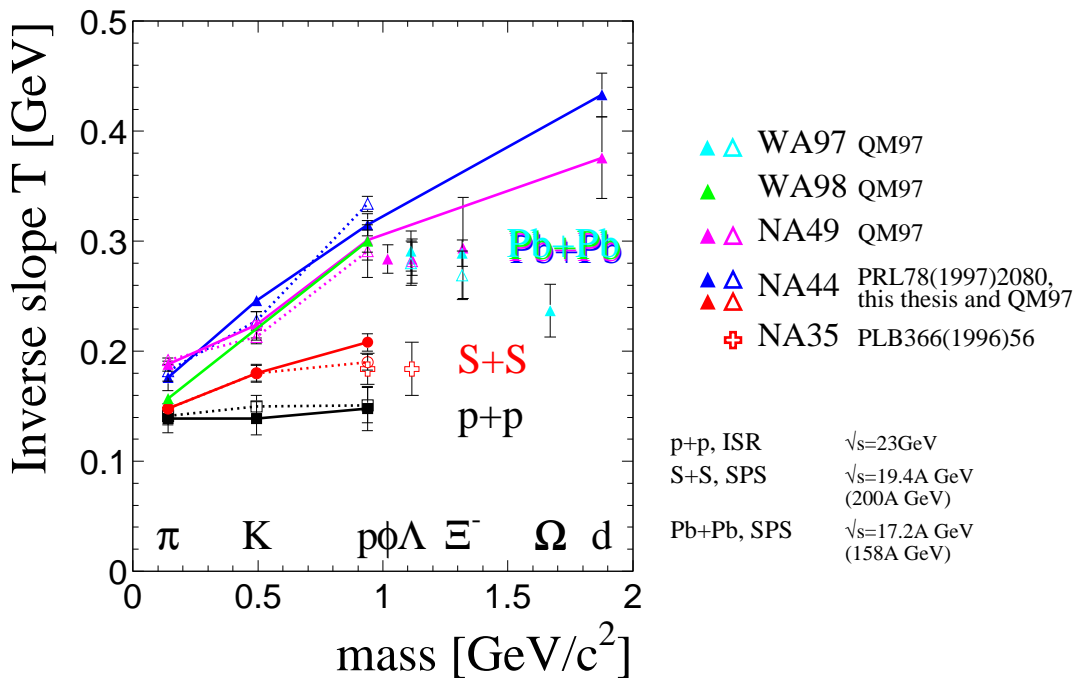

Figure 4.3: Adding the data from Ref. [58], Fig. 4.2 is shown again.

4.2 Chemical freeze-out

The other freeze-out is 'Chemical freeze-out' and relates with equilibrium between different flavours. If the hadron gas reaches chemical equilibrium, particle abundance is described by chemical potentials and temperature. The information of the chemical freeze-out can be extracted from particle ratio in the measurement. I note that it is not need that the both thermal and chemical freeze-out is happen at the same time.

Assuming a system in the chemical equilibrium state, the density of a particle is characterized by macroscopic parameters, chemical equilibrium temperature, and chemical potentials. The object for chemical freeze-out is the gas of hadrons, which consist of light (u and d) quarks and/or strange quarks. The charmed, bottomed and topped hadrons are not included in the model, because those heavy hadrons are not created by thermal creation due to suppression of the Boltzmann factor.

In the grand canonical system, the particle density ρ is described as

$$\rho = \frac{g}{2\pi^2} \int_0^\infty \frac{p^2 dp}{\exp\left[(E - \mu)/T_{ch}\right] \pm 1}$$

where T is the chemical equilibrium temperature, E is the energy, μ is the chemical potential and $\pm$ corresponds to fermions for plus and bosons for minus, respectively. Since we discuss the hadrons of u, d, s quarks and those anti-quarks, the potential μ is

$$\mu = Q\mu_q + s\mu_s$$

where Q is equal to 1 for u and d quark and -1 for the $\bar{\text{u}}$ and $\bar{\text{d}}$ quark, and s is the strange quantum number. The potential μ_q is for u/d/$\bar{\text{u}}$/$\bar{\text{d}}$ quarks, and μ_s is for s and $\bar{\text{s}}$ quark. For example, the potentials corresponding to π^+, π^-, K^+, K^-, p, and $\bar{\text{p}}$ are

$$\begin{aligned}
\mu_{\pi^+} &= & \mu_q &+ (-\mu_q) &= 0, & \mu_{K^+} &= & \mu_q &+ (-\mu_s), & \mu_{\text{p}} &= 3\mu_q, \\
\mu_{\pi^-} &= (-\mu_q) + & \mu_q & &= 0, & \mu_{K^-} &= (-\mu_q) + & \mu_s, & \mu_{\bar{\text{p}}} &= -3\mu_q,
\end{aligned}$$

respectively.

In the high temperature ($T_{ch} \approx$ pion mass), the system is described by the Boltzmann distributions and the density of a particle i is

$$\rho_i = \gamma^{|s_i|} \frac{g_i}{2\pi^2} T_{ch}^3 \left(\frac{m_i}{T_{ch}}\right)^2 K_2(m_i/T_{ch}) \, \lambda_q^{Q_i} \, \lambda_s^{s_i} \tag{4.6}$$

where g_i is a number of spin-isospin freedom, m_i is mass of the particle i, K_2 is the modified Bessel function and

$$\lambda_q = \exp(\mu_q/T_{ch}), \quad \lambda_s = \exp(\mu_s/T_{ch})$$

Table 4.3: The macroscopic parameters for the description of the chemical freeze-out near mid-rapidity for the Pb+Pb, S+S, p+Pb, p+S and p+Be collisions from the NA44 data. For descriptions of model (i) and (ii), see text. The values of dN/dy in the S+S and p+A collisions are from Refs. [50, 76]. The values of dN/dy in Pb+Pb correspond to top 3.7% centrality region.

		Pb+Pb	S+S	p+Pb	p+S	p+Be
T_{ch} [MeV]	(i)	137 - 145	142 - 149	134 - 142	136 - 144	135 - 142
	(ii)	135 - 143	139 - 146	133 - 140	134 - 141	133 - 140
μ_q [MeV]	(i)	60 - 68	50 - 56	24 - 31	27 - 33	22 - 29
	(ii)	59 - 67	49 - 55	24 - 31	26 - 33	22 - 28
μ_s [MeV]	(i)	10 - 25	13 - 34	-8 - 20	-10 - 21	-1 - 27
	(ii)	9 - 23	12 - 32	-7 - 20	-9 - 20	-2 - 27
γ_s	(i)	0.58 - 0.69	0.56 - 0.72	0.27 - 0.38	0.31 - 0.46	0.23 - 0.34
	(ii)	0.56 - 0.67	0.54 - 0.70	0.27 - 0.38	0.31 - 0.45	0.24 - 0.33
dN/dy	π^+	155.0±9.4	29.7±2.8	3.2±0.4	2.4±0.3	2.1±0.3
	π^-	161.0±9.7	—— same value with π^+ in a factor 1.00±0.15 ——			
	K$^+$	27.6±1.7	4.9±0.5	0.27±0.04	0.24±0.04	0.15±0.03
	K$^-$	15.4±1.1	3.4±0.4	0.21±0.03	0.18±0.03	0.13±0.01
	p	27.2±5.2	4.51±0.47	0.251±0.030	0.204±0.022	0.158±0.016
	$\bar{\text{p}}$	1.85±0.35	0.505±0.060	0.076±0.011	0.057±0.008	0.053±0.008

An additional factor γ_s is introduced to take account of possible incomplete strangeness chemical equilibrium [74]. The $\gamma_s = 1$ means the full strangeness chemical equilibrium.

The particle densities are computed by the equation (4.6) for the hadron gas including the resonances. The particle densities are calculated for two types of the hadron gas.

Model (i):   the gas consists of π, η, ω, ρ, $\eta\prime$, ϕ, p, n, N(1440), Δ, K, K*, Λ, Λ(1600), Σ, Σ(1385), Ξ, Ξ(1530), and Ω.

Model (ii):   the gas consists of stable hadrons and the higher mass resonances up to 1 GeV for light unflavoured meson, 1.6 GeV for N and Δ baryon and 2 GeV for the strange meson and baryon.

The resonances decay to the lower mass hadrons after chemical freeze-out. Therefore, the final particle densities for the pions, kaons and protons are given by considering the decays of the resonances to stable hadrons. Here, I apply the formula (4.6) for the particle yields observed in central region of rapidity where thermo-dynamical description is most adequate.

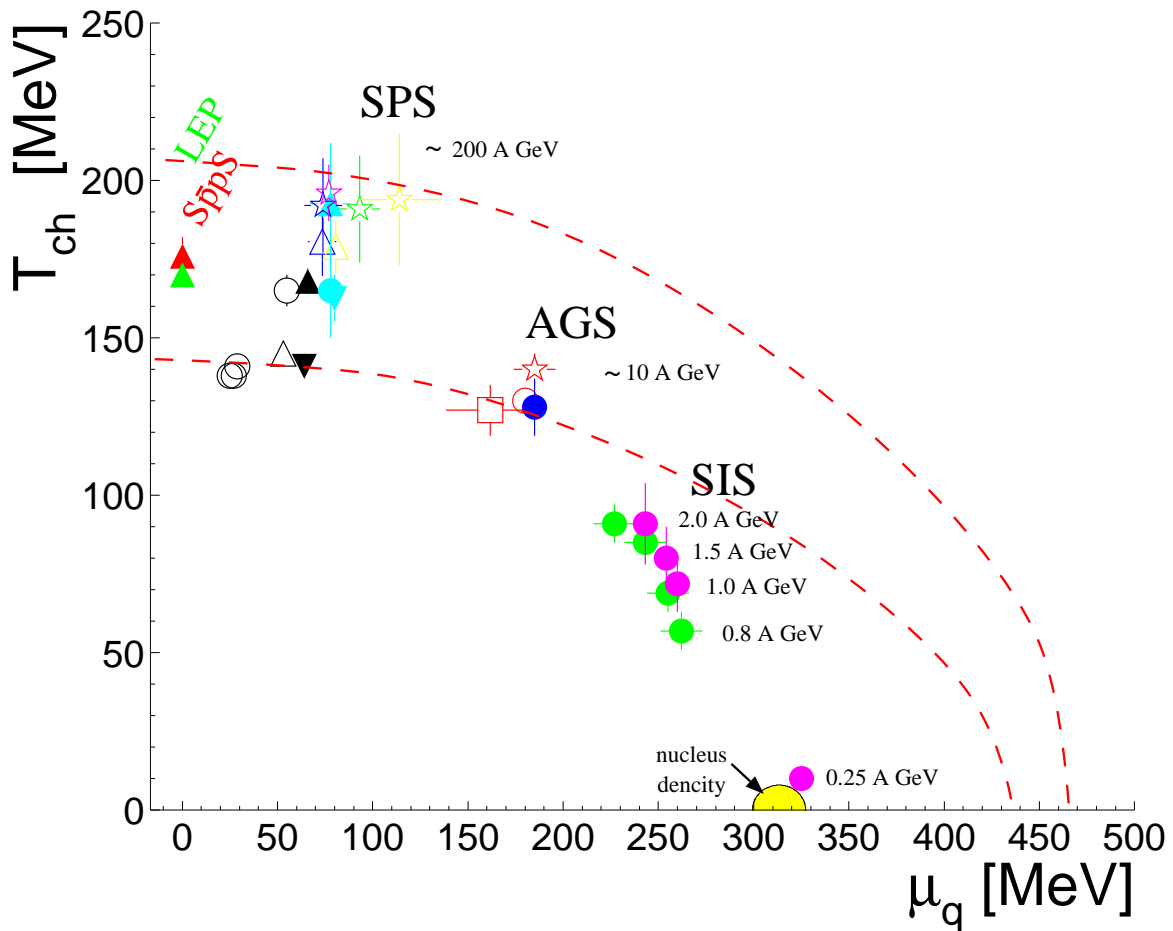Table 4.3 shows the chemical freeze-out temperature T_{ch}, the light quark chemical
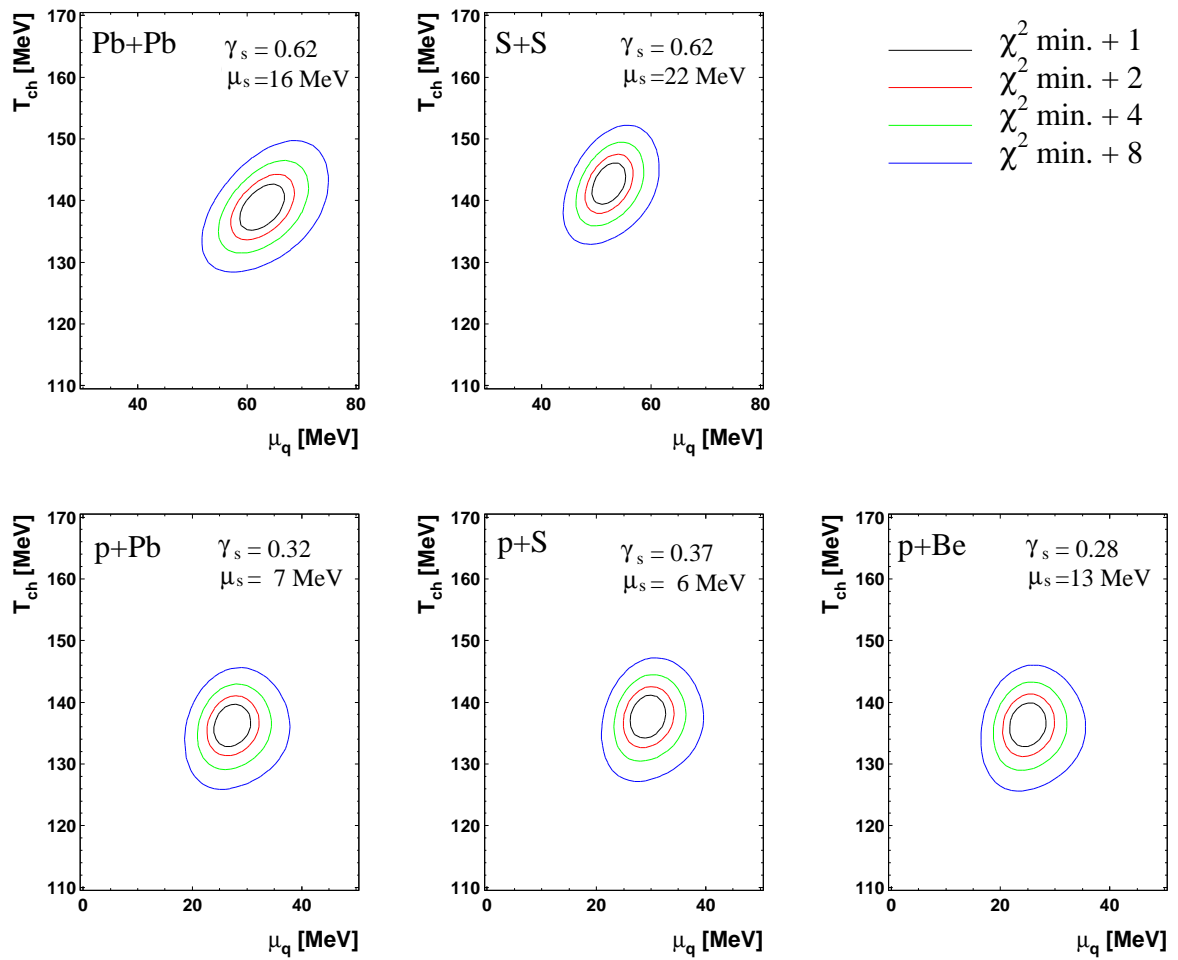
Figure 4.4: By fitting of model (i), chemical freeze-out temperature T_{ch} versus light quark chemical potential μ_q. The curves show constraints from fits to particle ratios and indicate χ^2 minimum $+1$, $+2$, $+4$ and $+8$ from the center of curves. The values of μ_s and γ_s are fixed as indicated in each plot.

potential μ_q, the strange quark chemical potential μ_s and the strangeness saturation factor γ_s. Those values are obtained as a region in χ^2 minimum+1 by fitting of the data. Fig. 4.4 shows examples of fit for model (i).

The difference between the model (i) and (ii) is small and it means that the high mass resonances have small effect for the particle ratio due to their low densities.

The chemical freeze-out temperatures (T_{ch}) are the same in the error bar in p+Be to Pb+Pb collisions at the SPS energy region, and equal or higher than the thermal freeze-out temperature.

Figure 4.5: The various chemical freeze-out temperatures and the light quark chemical potentials from Refs. [1], [77]-[81]. The region in the dashed lines is a lower estimation of the phase transition and mixed phase [82, 83].

The values of strangeness saturation factor γ_s are not equal to 1 for p+A to A+A collisions. That indicates that the hadron gas does not reach the full chemical equilibrium of the strangeness particles in the heavy ion collisions at the SPS energy region. It is shown that the clear difference of γ_s in p+A and A+A collisions, and abundance of strange particles are far from those at chemical equilibrium in p+A collisions than the state in A+A collisions.

The μ_q is increasing with the size of the collisions system. Since the chemical freeze-out temperature is independent of collisions systems (p+A and A+A), the system in p+A collisions has smaller μ_q/T_{ch}, that is, smaller baryon density than A+A collisions.

Fig. 4.5 shows the various chemical freeze-out temperature and the light quark chemical potentials in the mid-rapidity region in the central collisions. The collisions system dependence of T_{ch} and μ_q is much smaller than the beam energy dependence even if there is a fluctuation from models and the data of experimental groups. The dashed line corresponds to the lowest estimation of the QGP phase boundary and mixed phase [82, 83]. The figure indicates that the chemical freeze-out temperature is increasing with the beam energy. On the other hand, the baryon density in the mid-rapidity is decreasing with the beam energy. It is noted that the chemical freeze-out occurs nearby the QGP phase boundary from around AGS energy and higher region, especially the region in the SPS energy.

Chapter 5

SUMMARY AND CONCLUSION

The invariant cross sections of π^+, π^-, K^+, K^-, p and $\bar{p}$ near mid-rapidities in the central 158 A GeV/c Pb+Pb collisions are measured from the NA44 data, finally. I obtained the macroscopic parameters to describe the hadron source by approaches of the thermal and chemical freeze-out. The various transverse mass distributions are characterized by the thermal freeze-out temperature (T_{th}) and transverse flow (β_T) and the particle ratios are characterized by the chemical freeze-out temperature (T_{ch}), the chemical potential for light unflavoured quarks and strange quarks (μ_q, μ_s) and the strangeness saturation factor γ_s.

The thermal freeze-out occurs in the temperature of the value of about 130 MeV. From the particle ratio, it is shown that the chemical freeze-out temperature is about 140 MeV and the values of chemical potentials are approximately 65 MeV and 15 MeV for μ_q and μ_s, respectively and the strangeness saturation factor γ_s is about 0.6 in the Pb+Pb collisions at the CERN SPS. The difference of the both freeze-out temperature support a scenario, that is, in heavy ion collisions at the SPS energies, the hadron gas reaches to chemical equilibrium state with a partial equilibrium for the strangeness at first, and finally goes to the thermal freeze-out during the expansion. It is remarkable that the chemical potentials and the chemical freeze-out temperatures suggest that the state of the fire ball immediately after the collision is rather close to the region where we expects the QGP.

It is fount that chemical freeze-out occurs at higher (lower) temperature (density) with higher beam energy by systematical study of the various collisions systems ($e^+ + e^-$, $p + \bar{p}$, p+p, p+A, A+A, where A means nuclear) and the various beam energy region (LEP, $S\bar{p}S$, SPS, AGS and SIS).

It is also found that the collisions system dependence for the both temperatures are much smaller than the beam energy dependence.

Appendix A

Silicon Multiplicity detector in 1995 Pb run

This appendix is originally written for an internal report for the NA44 collaboration in May 1998.

A.1   Introduction

In the workshop held in March 1998 at SUNY/Stony Brook, the attendants discussed whether silicon detector is more useful than T0 for Pb95 run, which means Lead beam run in 1995. As Hiroaki Ohnishi had been showed in collaboration meeting, the $dN/d\eta$ distribution of negative charged particle on our silicon detector seems to be close to dN/dy distribution of hadron minus from NA49 data. Of cause, it is not sure that there is electron contamination for negative particles on our Si detector and hadron minus of NA49.

To discuss physics in Pb95 runs with silicon detector, it is important to check status of silicon detector in Pb95 run. I modified DST program to include silicon ADC information of channel by channel and re-run DST to get the information.

I will show the following items.

- dead pads list
- and ADC distributions
- typical ADC distributions of one channel on calibration run
- typical ADC distribution of one channel on run for singles

Table A.1: Run list I used for analysis of silicon multiplicity counter. VB means valid beam run which is defined CX and CX-veto counter. VB⊗T0 means VB⊗(high multiplicity requirement by T0 counter). VB⊗Mul1 means VB⊗(at least, one hit required on Hodoscope 2 and Hodoscope 3). Central physics run means VB⊗T0⊗Mul1. e/pi/K/p means no particle identification by Cherenkov counters, C1 and C2 in on-line trigger. K/p means that kaon or proton is selected by C1 and C2 in on-line trigger.

momentum setting spectrometer angle [mrad]	+4 GeV/c		-4 GeV/c		+8 GeV/c		-8 GeV/c	
	44	129	44	129	44	129	44	129
VB	3866	3589	3885	3607	3773	3539	3809	3665
VB⊗T0	3870	3595	3890	3610	3768	3542	3813	3669
VB⊗Mul1	3874	3575	3894	3613	3764		3814	3675
e/pi/K/p central physics run	3875	3599	3886	3614	3761	3544	3815	3656
K/p central physics run	3863	3585	3895	3619	3777	3547	3820	3663

Table A.1 shows run numbers which I used to check the silicon multiplicity detector for each setting.

A.2 Variables in NA44lib for the silicon detector

CWN file from DST modified has Silicon ADC information of each channel. The ADC values of silicon multiplicity counter is filled a common variable `SILOOPUP(i,j)`. The suffix `i` is corresponding to channel number (1-512) and `j` is corresponding to calibration variables. The comment `//FKEEPS/ALL_GENERAL/$SI_CAL` in Deck of CMZ in na44 libraries says,

- `j=1 :  position of pedestal [ch]`
- `j=2 :  pedestal width (sigma) [ch]`
- `j=3 :  threshold [ch]`
- `j=4 :  energy conversion coefficient [KeV/ch]`

where definition of threshold is $2 \times \sigma$ from pedestal position. After pedestal subtraction and energy conversion, all ADC values are summed and filled to variable `SiSumR` and

`SiSumL`, respectively. In addition 'SI HITS SUM' means number of channels of which ADC values are greater than threshold.

A.3 Dead pads

Here, 'dead pads' means pad which has no ADC value. I checked all cwn files to find dead pads in the runs in Table A.1. The dead pads are the same during singles runs. The Fig. A.1 is briefly figure of Silicon pads. The heavy ion beam passes from the surface of this page to back. The dead pads are showed as masked box. The name of 2 panel of the detector is showed in the Fig. A.1 and they were named as seeing from the detector to target direction.
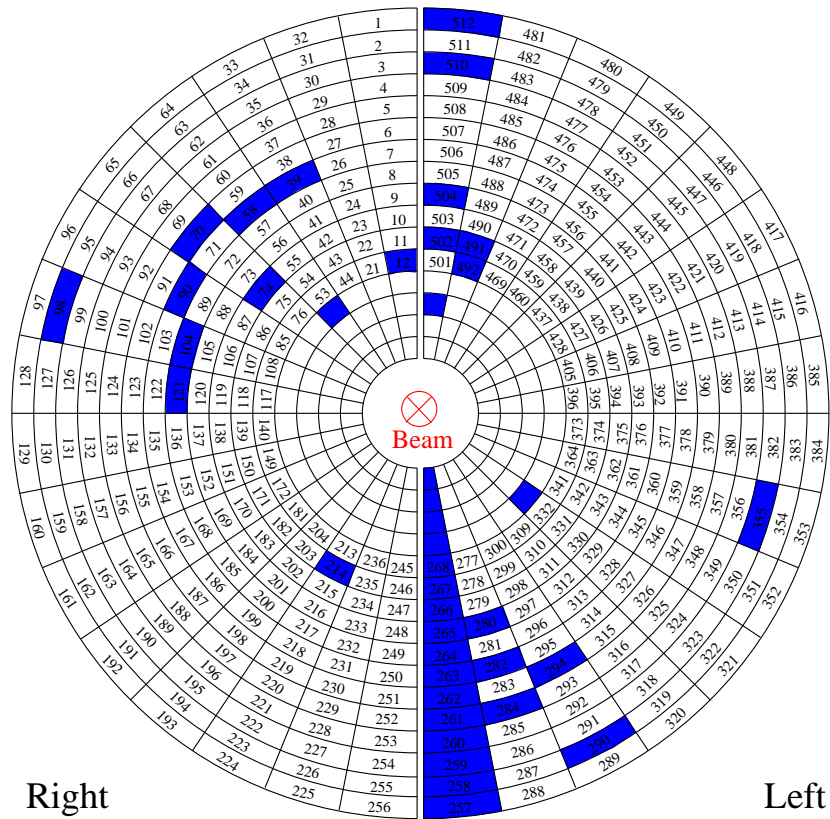
Figure A.1: Brief plot of silicon pads alignment. The number on each channel is corresponding to channel number. The ADC values of pad masked are always 0 (dead pads).

Table A.2: The peak positions and values of sigma by fitting gaussian function for pedestal and 1 MIP.

	pedestal		1 MIP	
	peak [KeV]	sigma [KeV]	peak [KeV]	sigma [KeV]
Si-Right	-2.16 ± 0.03	19.57 ± 0.03	83.60 ± 0.10	31.30 ± 0.16
Si-Left	-2.00 ± 0.03	19.28 ± 0.03	85.06 ± 0.09	28.62 ± 0.13

A.4   Calibration

Up-to-now (Dec/1998), the silicon calibration is done only once for Pb95 run. The run number for the calibration is 3524. Fig. A.2 shows ADC distribution of each side in the calibration run. The peak positions of pedestal and one MIP listed in Table A.2.

The read lines in Fig. A.2 are on 85 [KeV] and 170 [KeV]. We can see clear separation of pedestal and 1 MIP in calibration run. The peak of 2 MIP is not clear in the histograms, however, we can see the shoulder in tail of 1 MIP around 2 MIP. It means that the Silicon ADC values has linearity for MIP in calibration run.
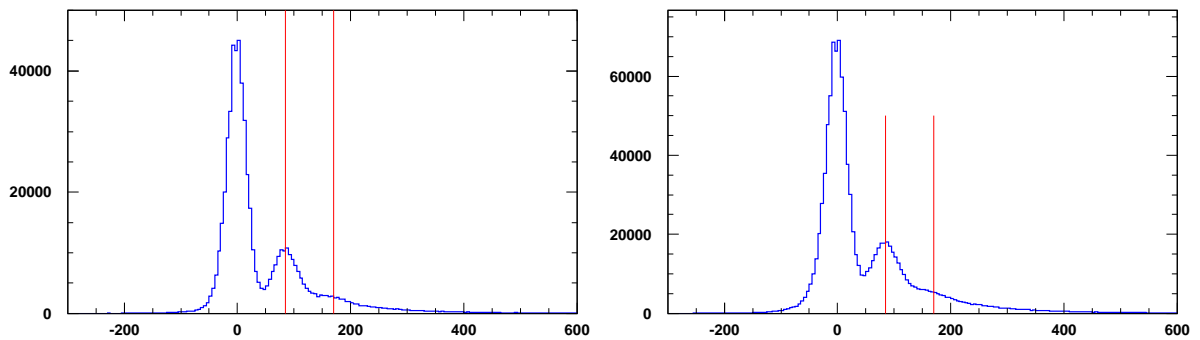
Figure A.2: The figures are ADC distribution of Silicon-Right and Silicon-Left, respectively. The unit of horizontal axis is [KeV] (energy conversion is done channel by channel). These histograms are superimposed all channels for each side without dead channels.

Table A.3: List of run number and momentum, spectrometer angle and trigger setting. In the list 'PC' means 'Pad Chamber trigger'. PC trigger is on, when pulse height of anode wire is greater than a threshold.

run number	momentum setting	angle	trigger setting
3544	+8 GeV/c,	128mrad,	VB⊗T0⊗Mul1, e/pi/K/p run
3547	+8 GeV/c,	128mrad,	VB⊗T0⊗PC⊗Mul1, K/p run
3585	+4 GeV/c,	128mrad,	VB⊗T0⊗PC⊗Mul1, K/p run
3599	+4 GeV/c,	128mrad,	VB⊗T0⊗Mul1, e/pi/K/p run
3614	-4 GeV/c,	128mrad,	VB⊗T0⊗Mul1, e/pi/K/p run
3619	-4 GeV/c,	128mrad,	VB⊗T0⊗PC⊗Mul1, K/p run
3656	-8 GeV/c,	128mrad,	VB⊗T0⊗Mul1, e/pi/K/p run
3663	-8 GeV/c,	128mrad,	VB⊗T0⊗PC⊗Mul1, K/p run
3761	+8 GeV/c,	44mrad,	VB⊗T0⊗Mul1, e/pi/K/p run
3777	+8 GeV/c,	44mrad,	VB⊗T0⊗PC⊗Mul1, K/p run
3815	-8 GeV/c,	44mrad,	VB⊗T0⊗Mul1, e/pi/K/p run
3820	-8 GeV/c,	44mrad,	VB⊗T0⊗PC⊗Mul1, K/p run
3844	-4 GeV/c,	44mrad,	VB⊗T0⊗Mul1, e/pi/K/p run
3863	+4 GeV/c,	44mrad,	VB⊗T0⊗PC⊗Mul1, K/p run
3875	+4 GeV/c,	44mrad,	VB⊗T0⊗Mul1, e/pi/K/p run
3895	-4 GeV/c,	44mrad,	VB⊗T0⊗PC⊗Mul1, K/p run

A.5   Typical ADC distribution for each channel

Fig. A.3 and Fig. A.4 are typical ADC distribution of each channel. Histograms of solid line are from physics runs. Histograms hatched are ADC distribution of calibration run. The vertical line shows the position of threshold for each channel. The threshold is defined as two sigma of pedestal.

From left to right, those histograms are corresponding to channel 161 to 176 for Fig. A.3 and channel 417 to 432 for Fig. A.4. From top to bottom, the order is from small run number to large one. The order is showed in Table A.3 also.
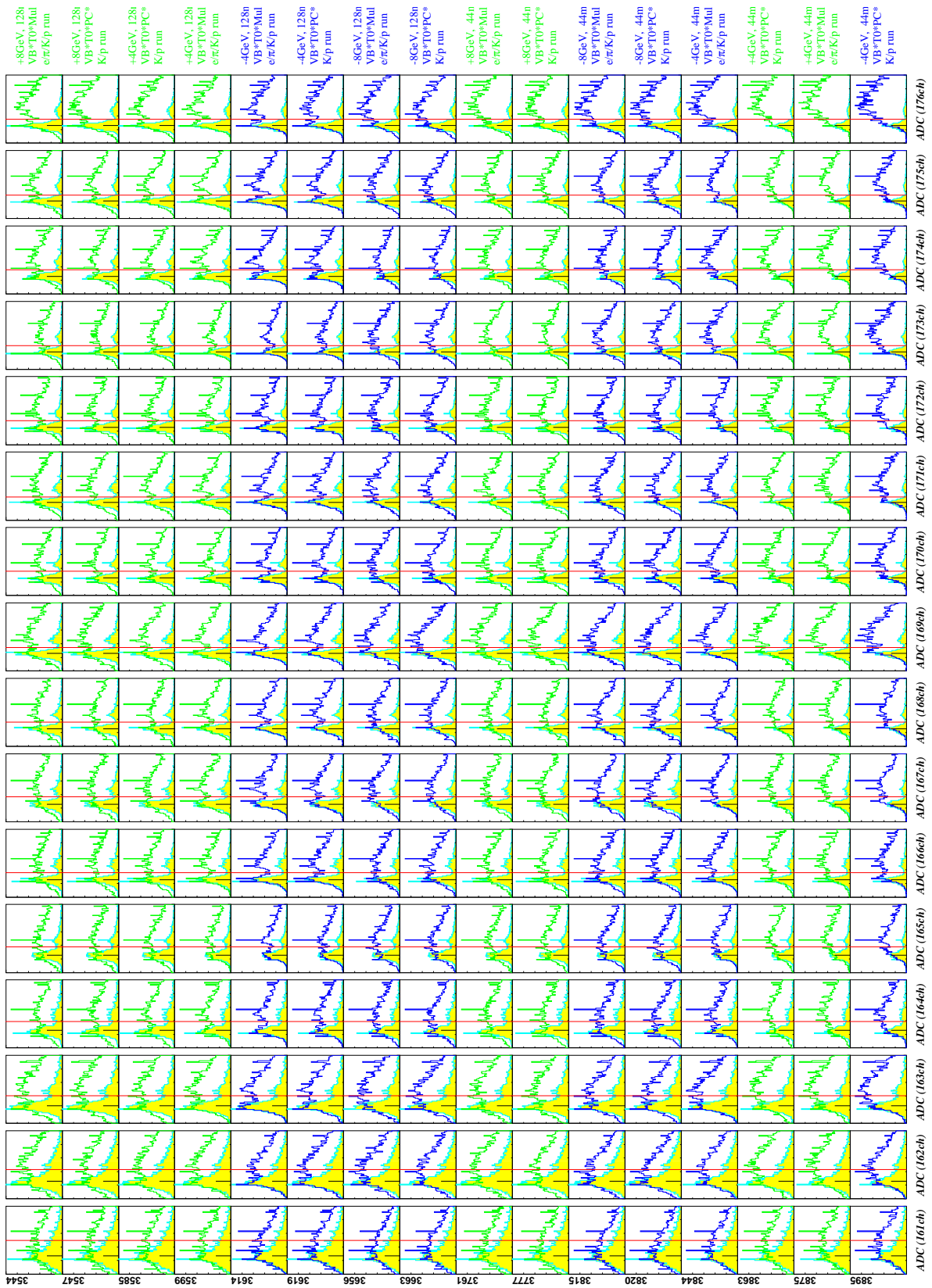
Figure A.3: ADC distribution (Silicon-Right). Please look at it with rotating clockwise.
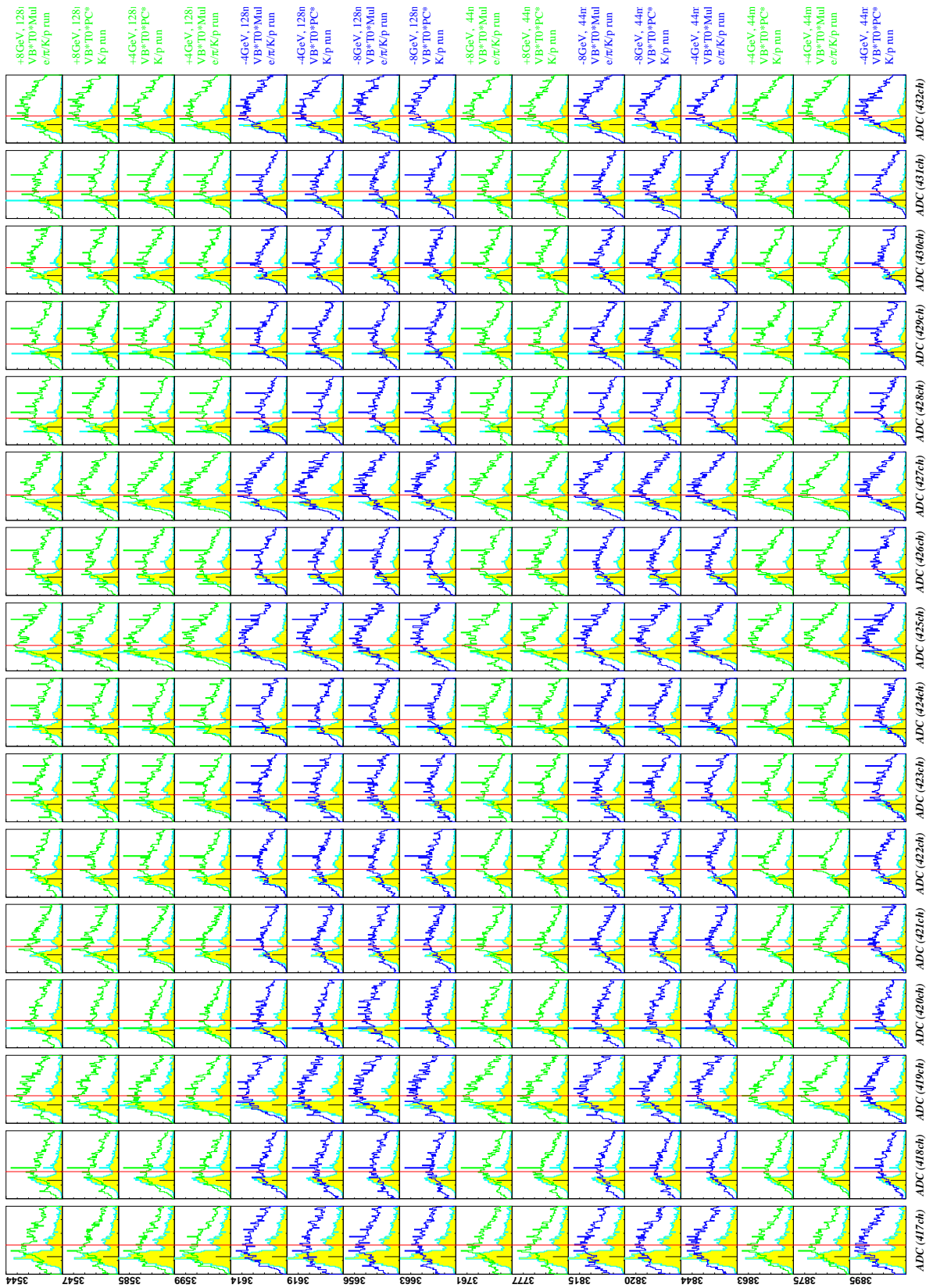
Figure A.4: ADC distribution (Silicon-Right). Please look at it with rotating clockwise.

I checked all of channels for all (central runs, ±4 and ±8 GeV/*c*, high and low angle) setting. The general trends of ADC distribution are

- the resolution of pulse height of Silicon LEFT is worse than Silicon-RIGHT
- the resolution is changing to worse with run number
- almost ADC of pad on Silicon-LEFT have double peak of pedestal and it is strong under positive and negative 8 GeV/*c* setting
- there is pedestal shift and its trend seems no dependence of magnet setting (polarity of magnetic field, 4 or 8 GeV/*c*)

As showed in Fig. A.5, pedestal peak position of VB run are different from the others. To get centrality, we have to compare ADC distribution of physics run to one of VB run. It is need that pedestal position on each channels are independent of trigger setting to calculation of centrality. The data, however, show pedestal shift for all of VB runs. To fix this problem, calibration of run by run is need.

A.6   Scatter plot of Si Hits versus Si ADC sum

Fig. A.6 shows Hits versus ADC sum for VB⊗Mul1 trigger runs. The effect of delta electron is smaller than the difference of pulse height resolution between Si-Right and Si-Left. In addition, we can see double pedestal on ADC sum distribution of Si-Left with 8 GeV

We know that Si hits are not liner for Si ADC sum because 'one hit' includes 1 MIP, 2 MIP, 3 MIP, and more. However, there is a liner component; Si hits are in proportional to ADC sum.

The plots in Fig. A.7 is from run 3894 (-4 GeV/*c*, low angle, VB⊗Mul1 run). The left scatter plot is ADC sum versus Hits on Si-Right and right-hand side plot is ADC distribution (ADC distributions of all channels without dead channels are superimposed on one histogram). The part in a box in plot left-hand side is corresponding to the plot pointed by arrow. Pedestal seems to be shifted as +10 [KeV] and then the threshold would be around 50 [KeV]. The component in the box is just between pedestal and 1 MIP. I conclude that we can see the kind of two components in scatter plot due to wide ADC resolution.
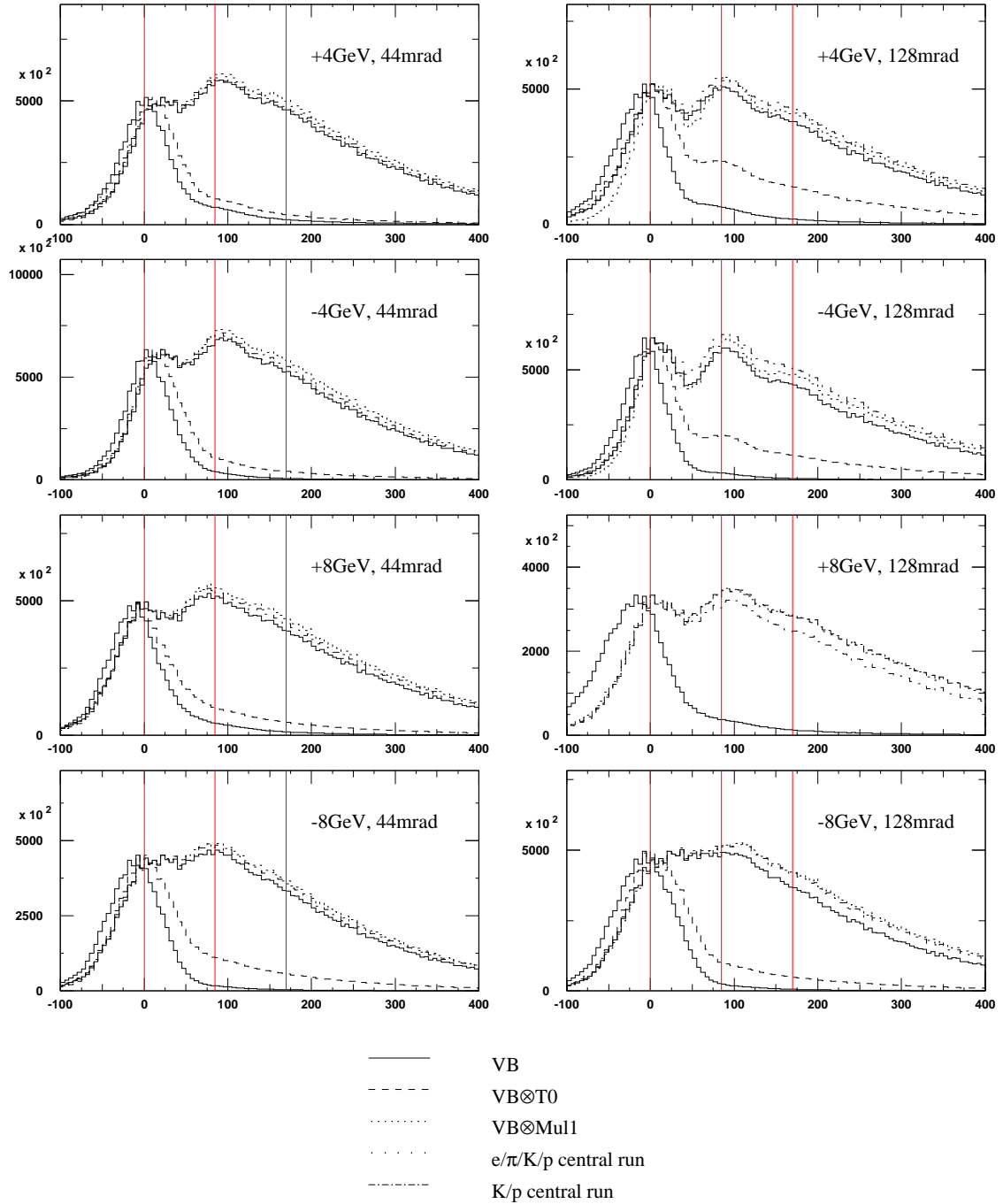
Figure A.5: ADC distribution of Si-Right. The unit of horizontal axis is [KeV] (energy conversion is done channel by channel). Black, magenta, cyan, green and blue plot are VB run, VB⊗T0, VB⊗Mul1, e/pi/K/p central run and K/p central run, respectively. The read lines are on ADC=0, 85 and 170 [KeV] as pedestal peak, 1 MIP and 2 MIP, respectively.
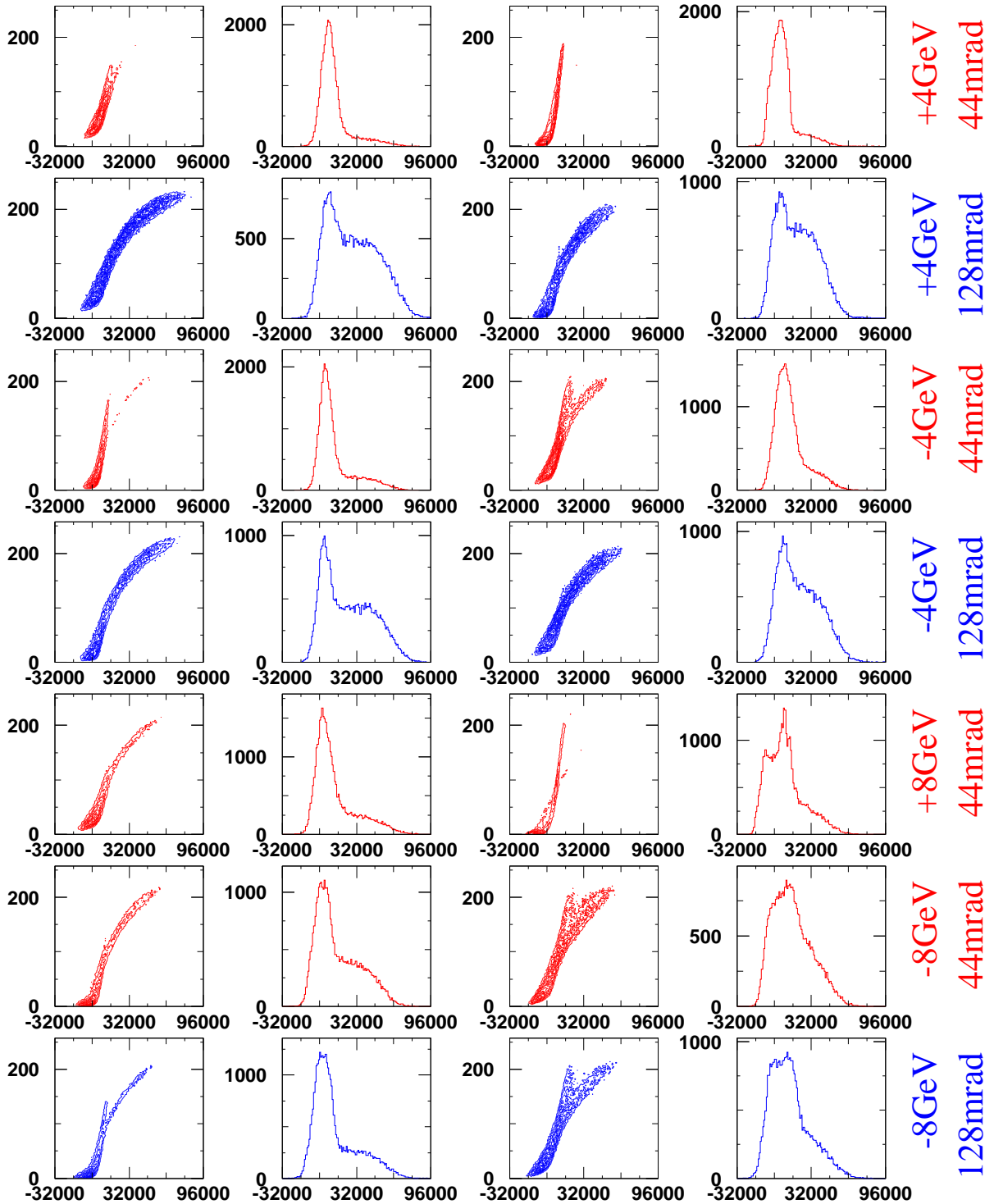
Figure A.6: From left-hand side to right-hand side, Hits versus ADC sum on Si-right, ADC sum on Si-right, Hits versus ADC sum on Si-left and ADC sum on Si-left.
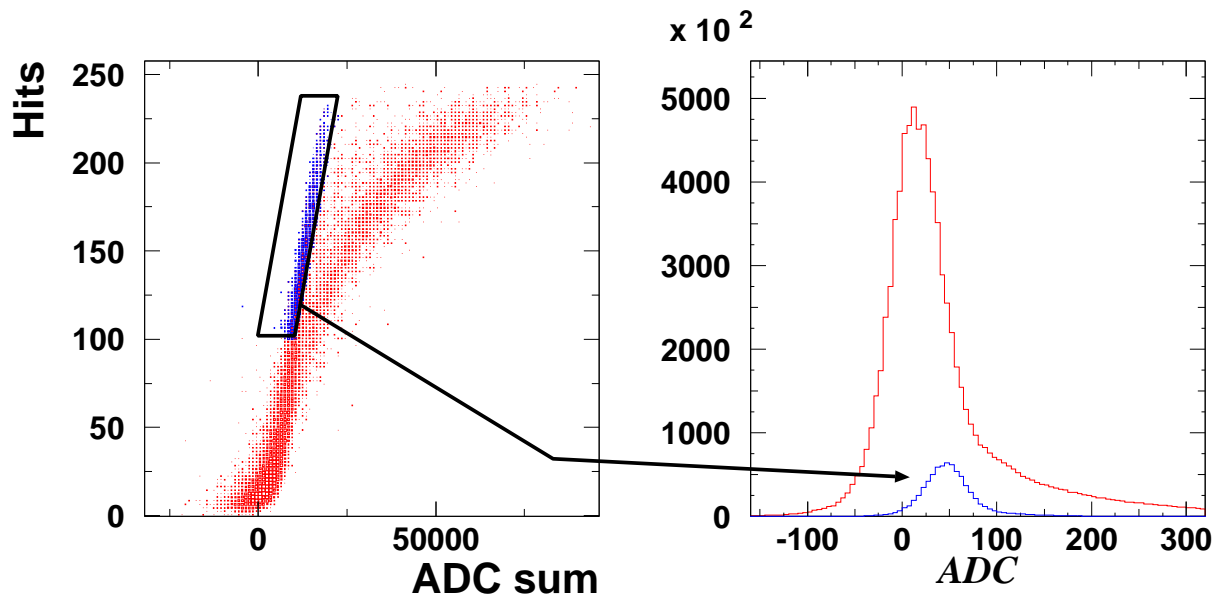
Figure A.7: Scatter plot of ADC sum versus Hits on Si-Right (left-hand side) and ADC distribution on Si-Right.

A.7 Summary

The dead pads are checked in Pb95 run. The numbers of dead pads on Si-Right and Si-Left are 11 and 31. In addition, there are no dead pads during the data taking.

In the calibration run, we can see separation of 1 MIP to pedestal. In addition, Si ADC has linearity for MIP.

In the physics runs, resolution of pulse height is changing to worse with run number. It is difficult to separate pedestal peak and 1 MIP peak on Si-Left pads because resolution of pulse height on Si-Left is bad. On the Si-Left, the pedestal has double peak under 8 GeV setting.

The pedestal peak positions of Si pads are not the same for each trigger, momentum and angle setting. I have no idea the reason why there is pedestal shift in the same momentum setting. At least, it is not effect of delta electron because delta electron effect should be independent from trigger.

By the wide ADC resolution and pedestal shift, the scatter plot of Si Hits and Si ADC sum seems to have two components. Pedestal shift problem would be possible to fixed by

run by run calibration. However, it is impossible to get better ADC resolution.

A.8   Conclusion

I conclude that we can not use Si-Left information to analyze Pb95 data because of bad status. To estimate multiplicity and effect of delta-electron, it requires that one side of performance of Si detector is the same with the other side. Unfortunately, Si-Left has enough performance to reconstruct charged multiplicity from pulse height of pad.

Si-Right is delta-clean-side for π^+, K^+ and p data. It is acceptable if we give-up to analyze negative charged particle. I DO NOT like to do that. Why don't you use the T0 detector? T0 seems to have no serious problem like a silicon multiplicty counter.

Furthermore, even if we give-up negative charged particle data, there is the other task for Si-right, that is, calibration of pedestal and pulse height should be done in run by run. If we would like to analyze our data with only Si-Right information, we need Si calibration run by run. It seems to be heavy work and I can not estimate the time we need to do it.

Since it seems to be endless job that we try to analyze silicon, I conclude that we should use only T0 to calculate centrality. Because we have not enough time to publish our data.

Bibliography

[1] V. Metag, *Nucl. Phys.* **A638**, (1998) 45c.

[2] E. Fermi, *Prog. Theor. Phys.* **5** (1950) 570.

[3] U. Heinz, P.R. Subramanian and W. Greiner, *Z. Phys.* **A318**, (1994) 247.

[4] P. Koch, B. Müller, H. Stöker and W. Greiner, *Mod. Phys. Lett.* A **3** (1988) 737.

[5] J. Ellis, U. Heinz and H. Kowalski, *Phys. Lett.* **B233**, (1989) 233.

[6] K.S. Lee, M.J. Rhoades-Brown and U. Heinz, *Phys. Rev.* **C37**, (1988) 1452.

[7] C. Greiner, P. Koch and H. Stöker, *Phys. Rev. Lett.* **58**, (1987) 1825.

[8] T. Hatsuda and S.H. Lee, *Phys. Rev.* **C46**, (1992) R34.

[9] T. Hatsuda and H. Shiomi, *Nucl. Phys.* **A590**, (1995) 103c.

[10] T. Hashimoto, O. Miyamura, K. Hirose and T. Kanki, *Phys. Rev. Lett.* **57**, (1986) 2123.

[11] T. Matsui and H. Satz, *Phys. Lett.* **B178**, (1986) 416.

[12] The two particle interferometry has been studied by many physicists. *'Introduction to High-Energy Heavy-Ion Collisions'* by Cheuk-Yin Wong (World Scientific) has the detail explanation of the HBT study in the page 431-475.

[13] The physics from the single particle spectra, the transverse momentum distribution and the yield has been developed from many view points. Please refer "*Proceedings of Quark Matter'97*" *Nucl. Phys.* **A638** (1998) 351c-356c and 357c-364c.

[14] M. Tamada, *Evidence for new type of cosmic ray nuclear interactions named 'Centauro'*, Nuovo Cimento **41B** (1977) 245.

[15] P. Wurm for the CERES Collaboration, *Nucl. Phys.* **A590**, (1995) 103c.

[16] G. Agakishiev et al. (CERES Collaboration), *Eur. Phys. J.* **C4**, (1998) 249

[17] G. Agakishiev et al. (CERES Collaboration), *Phys. Rev. Lett.* **75**, (1995) 1272.

[18] G. Agakishiev et al. (CERES Collaboration), *Phys. Lett.* **B422**, (1998) 405.

[19] Particle Data Group, *Eur. Phys. J.* **C3**, (1998) 1.

[20] M. Gonin for the NA50 Collaboration, *Nucl. Phys.* **A610**, (1996) 404c.

[21] G. Cocconi, *Phys. Lett.* **49B**, (1974) 459.

[22] L. Ramello for the NA50 Collaboration, *Nucl. Phys.* **A638**, (1998) 278c.

[23] R. Hanbury-Brown and R.Q. Twiss, *Philios. Mag* **45** (1954) 633.

[24] R. Hanbury-Brown and R.Q. Twiss, *Nature* **178** (1956) 1064.

[25] M. Gyulassy, S.K. Kauffmann and L.W. Wilson, *Phys. Rev.* **C20**, (1979) 2267.

[26] B. Lørstad, *Mod. Phys.* **A4** (1989) 2861.

[27] I.G. Bearden et al., *Phys. Rev. Lett.* **78**, (1997) 2080.

[28] J. Barrette et al., *Phys. Rev. Lett.* **73**, (1994) 2532.

[29] J. Barrette et al., *Nucl. Phys.* **A590**, (1995) 259c.

[30] Y.C. Zhang and J.P. Wessels for the E877 Collaboration, *Nucl. Phys.* **A590**, (1995) 557c.

[31] S. Nishimura for the WA98 Collaboration, *Nucl. Phys.* **A638**, (1998) 459c.

[32] T.J. Humanic et al. (NA35 Collaboration), *Z. Phys.* **C38**, (1988) 79.
     see also K.K. Kolehmainen and M. Gyulassy, *Phys. Lett.* **B180**, (1986) 203.

[33] N. Maeda et al., *Nucl. Instr. and Meth.* **A346**, (1994) 132.

[34] Eva Barbara Holzer, Ph.D. Thesis:
     Proton, deuterons and source dimensions from 33 TeV/c Pb-collisions

[35] H. Becker et al.,
Multipurpose analogue multiplex read out system for pad/strip detectors: description and instruction manual
ALICE Collaboration, 1997.

[36] H. van Hecke et al., *Nucl. Instr. and Meth.* **A346**, (1994) 127.

[37] D.E. Fields et al., *Nucl. Instr. and Meth.* **A349**, (1994) 431.

[38] C.W. Fabjan et al., *Nucl. Instr. and Meth.* **A367**, (1995) 240.

[39] S. Esumi et al. *Fizika* **B4**, (1995) 205.

[40] A. Bream et al., *Nucl. Instr. and Meth.* **A409**, (1998) 426.
and it is available as CERN-PPE-97-120.

[41] T. Akesson et al. CERN-EP/87-111.

[42] A. Franz, A. Ljubicic and D.S. Zachary, *Nucl. Instr. and Meth.* **A384**, (1997) 371.

[43] H. Sorge, *Phys. Rev.* **C52**, (1995) 3291.
see also `http://alba.physics.sunysb.edu/`

[44] Nobuhide Maeda, Ph.D. Thesis:
Transverse momentum dependence of the space-time evolution of the particle source produced in S+Pb collisions at 200 GeV per nucleon

[45] T. Tanimori et al., *Nucl. Instr. and Meth.* **216**, (1983) 57.

[46] T. Sugitate et al., *Nucl. Instr. and Meth.* **A249**, (1986) 354.

[47] HBOOK Reference Manual, CERN Program Library Long Writeup Y250.

[48] CN/ASD/SImulation section, GEANT - Detector Description and Simulation Tool, CERN Program Library W5013. 1993

[49] J.P. Sullivan, NA44 note, *H2 efficiency Study.*

[50] I.G. Bearden et al., *Phys. Rev.* **C57**, (1998) 837.

[51] Jehanne Simon-Gillo, Jerry Dodd, Barbara Jacak, Michael Murray and Nu Xu
Singles Analysis - putting the questions to rest and getting a life
on the NA44 Web page under miscellaneous writeups of NA44 restricted.

[52] CN/ASD, Beam Transport Simulation, Including Decay W151. CERN, 1974
     `http://wwwinfo.cern.ch/asdoc/shortwrupsdir/w151/top.html`

[53] C.A. Ogilve for the E866 and E917 Collaboration, *Nucl. Phys.* **A638**, (1998) 57c.

[54] J.P. Wessels for the E877 Collaboration, *Nucl. Phys.* **A638**, (1998) 69c.

[55] C.A. Pruneau for the AGS E864 Collaboration, *Nucl. Phys.* **A638**, (1998) 81c.

[56] G. Roland for the NA49 Collaboration, *Nucl. Phys.* **A638**, (1998) 91c.

[57] A. Sakaguchi for the NA44 Collaboration, *Nucl. Phys.* **A638**, (1998) 103c.

[58] I. Králik for the WA97 Collaboration, *Nucl. Phys.* **A638**, (1998) 115c.

[59] B. Wyslouch for the WA98 Collaboration, *Nucl. Phys.* **A638**, (1998) 147c.

[60] T. Petzmann for the WA98 Collaboration, *Nucl. Phys.* **A638**, (1998) 415c.

[61] M. Kaneta for the NA44 Collaboration, *Nucl. Phys.* **A638**, (1998) 419c.

[62] H. Sako for the E802 Collaboration, *Nucl. Phys.* **A638**, (1998) 427c.

[63] F. Pühlhhofer for the NA49 Collaboration, *Nucl. Phys.* **A638**, (1998) 431c.

[64] F. Ceretto for the CERES Collaboration, *Nucl. Phys.* **A638**, (1998) 467c.

[65] T. Cörgo and B. Lørstad, *Phys. Rev.* **C54**, (1996) 1390.

[66] E. Schnedermann et al., *Phys. Rev.* **C48**, (1993) 2462.

[67] N. Xu for the NA44 Collaboration, *Nucl. Phys.* **A610**, (1996) 175c.

[68] M. Kaneta for the NA44 Collaboration., *Prog. Theor. Phys. Suppl.* **129** (1997) 167.

[69] T. Abbot et al., *Phys. Rev. Lett.* **D45**, (1992) 3906.

[70] T. Abbot et al., *Phys. Rev. Lett.* **D45**, (1992) 3906.

[71] B. Alper et al., *Nucl. Phys.* **B100**, (1975) 237.

[72] K. Guettler et al., *Nucl. Phys.* **B116**, (1976) 77.

[73] T. Alber et al., *Phys. Lett.* **B366**, (1996) 56.

[74] J. Rafelski, *Phys. Lett.* **B262**, (1991) 333.

[75] H. van Hecke, H. Sorge and N. Xu, nucl-th/9804035.

[76] H. Bøggild et al., *Phys. Rev.* **C59**, (1999) 328.

[77] F. Becattini, hep-ph/9701275.

[78] F. Becattini and U. Heinz, *Z. Phys.* **C76**, (1997) 269.

[79] F. Becattini, M. Gázdzicki and J. Sollfrank, *Nucl. Phys.* **A638**, (1998) 403c.

[80] A.D Panagiotou, G. Mayromanolakis and J. Tzoulis, *Phys. Rev.* **C53**, (1996) 1353.

[81] J. Letessier, J. Rafelski and A. Tounsi, *Phys. Lett.* **B328**, (1994) 499.

[82] M.I. Gorenstein, H. Stöchker, G.D. Yan, S.N. Yang and W. Greiner, nucl-th/9711055 and *J. Phys.* **G24** 1998 1777.

[83] U. Heinz and C. Loureço, CERN Courier, p13-16, March 1998.

Acknowledgements